Doctoral Dissertation

Exploration of Fundamental Physics with Neutron Optics Using Advanced Machining Technology

先端的加工技術を用いた中性子光学による基礎物理の探究

by

Takuhiro Fujiie

Laboratory for Particle Properties
Department of Particle Physics and Astrophysics
Graduate School of Science
Nagoya University

Supervisor: Masaaki Kitaguchi

March, 2024

Abstract

The current Standard Model of particle physics accurately explains many phenomena, yet its inability to unify strong and gravitational forces suggests the need for new physics. Neutrons, being mass-bearing and electrically neutral, serve as useful test particles in the search for new physics. Especially, precision measurements using low-energy neutrons have yielded significant results since they can be handled optically. Recently, the use of neutron optics has been proposed to explore the fifth force and fundamental symmetry breaking, reaffirming its significance in the field. To realize such research, neutron optics demands enhanced measurement precision and flexible experimental frameworks.

In current neutron optics, sufficient statistical quantities are secured using large-area beams and large components. Despite the increased neutron intensity from pulsed neutron sources, the usable statistical quantity for experiments has been limited due to the manufacturing and installation precision limits of neutron optics components. Additionally, neutron optics components for precision measurements require micro to nanometer-level accuracy, making their development challenging. I have focused on using advanced machining technologies in developing neutron optics components, maintaining accuracy in large components, and improving both the shape accuracy and installation precision of these components. These efforts, demonstrating the advancement of neutron optics, were validated through three experimental approaches.

In the first experiment, I demonstrated the development of large components maintaining shape accuracy by measuring the reflection of epithermal neutrons. I developed a large flat neutron mirror with a 0.3 mrad slope error and 100×300 mm^2 surface area, demonstrating the potential applicability of neutron optics to the epithermal region. The second experiment used dynamical diffraction in the fifth force search experiment, proving shape accuracy improvement. This experiment significantly reduced the dominant systematic uncertainty, the single-crystal sample thickness error, to less than 1 µm, allowing a more accurate approach to the fifth force. Finally, the development of a multilayer neutron interferometer demonstrated an improvement in component installation accuracy. By adapting optical substrates and adjustment devices used in laser optics for neutron optical components, I achieved component installation with about 30 nm precision, enabling observation of neutron interference dependent on neutron wavelength. The development of this interferometer showed the potential to construct an experimental setup previously deemed impossible.

These demonstration experiments indicate that the application of advanced machining technologies advances neutron optics. The development of neutron optics reduces uncertainty in physical measurements and enables the construction of new experimental systems. This research demonstrates the contribution of neutron optics advancement to the exploration of fundamental physics.

Contents

List of Figures

List of Tables

Part I

Introduction

Chapter 1

Exploration of Fundamental Physics using Neutron Optics

In fundamental physics, efforts are being made to broadly and generally understand physical phenomena through a deeper comprehension of the behavior of elementary particles and their interactions. Currently, the Standard Model of particle physics, which unifies electromagnetic and weak forces among the four basic interactions, accounts for the largest number of physical phenomena with the greatest precision. However, the theory that includes the remaining strong force and gravity is still developing, and understanding these interactions remains a challenge in fundamental physics.

The advancement of theoretical physics has always been supported by experimental verification. Among the numerous experiments conducted, many significant results have been obtained from experiments using neutrons. A neutron is a composite particle made up of one up and two down quarks, first observed by Chadwick[1]. Neutrons are characterized by having mass, no charge, a magnetic moment, and a long lifetime of about 15 minutes. Since non-relativistic neutrons are known to behave as de Broglie waves, the wavelength, energy, and momentum of neutrons are closely related. Among a wide energy range, the wavelength of neutrons near 300 K in the Boltzmann distribution is similar to that of X-rays. Neutrons in this wavelength region can utilize optical phenomena such as interference, reflection, refraction, and diffraction like X-rays. The field encompassing the optical treatment of neutrons is generally referred to as "Neutron Optics". Research using neutron optics, active since the 1970s, has played a crucial role in both fundamental and applied physics. It has notably advanced the field of fundamental physics by harnessing the inherent properties of neutrons and their capabilities in optical handling. The substantial value of neutron optics is highlighted by historical studies that have investigated phenomena inaccessible by other experimental techniques. To this day, neutron optics remains an essential tool in the proposal and execution of fundamental physics experiments, continually uncovering new facets of previously unknown phenomena.

Fundamental physics experiments using neutron optics have continually progressed alongside increasing demands for experimental precision. The advent of pulsed neutron sources, in particular, revolutionized neutron experiments. The ability to use neutrons of various wavelengths simultaneously led to improvements in wavelength-dependent measurements and statistical quantities. However, the development of neutron optical components is still a work in progress. Unlike X-ray sources, where focusing systems using electromagnetic forces are applicable, neutron sources can't create such focusing systems. Therefore, neutrons from a source are shaped using shields before being directed to experimental apparatuses. To create a focusing system, large mirrors capable of accepting a wide-area neutron beam are needed. Similarly, large samples that can accept a wide-area beam are required for components irradiated with neutrons not to compromise statistical quantities. While components

used in X-ray optics can rely on the local precision of components due to the availability of focusing systems, neutron optical components require global precision in the area of use because of the unavailability of a focusing system. Developing large neutron optical components with high shape accuracy is challenging. Thus far, neutron optics has often sacrificed shape accuracy for improved statistics and experimental precision. However, with the advent of pulsed neutron sources solving the statistical quantity issues, the next challenge is enhancing the precision of neutron optical components.

The following sections describe the motivation for expanding neutron optics to explore fundamental physics. Section 1.1 describes the fundamental physics that can be investigated using neutron optics, providing insights into how this technology enhances our understanding of fundamental physics. Section 1.2 focuses on the basic properties of neutron optics, detailing the principles and mechanisms that govern its functionality. Finally, Section 1.3 describes directions for the development of neutron optics for the exploration of fundamental physics.

1.1 Fundamental Physics using Neutron Optics

In this section, we will clarify the motivation for this study by briefly summarizing the current status and challenges in fundamental physics. In the subsections that follow, we describe experiments using neutron optics that have been designed to approach these issues and organized by each physical topic.

In inflation theory, it is believed that the fundamental particles and interactions we know today were unified at the beginning of the universe. Hence, it is conceivable that the four fundamental interactions -electromagnetic, weak, strong, and gravitational interaction- could be described in a unified theory at a certain energy scale, an idea encapsulated in the Grand Unified Theory. Currently, the particle standard theory, which unifies the electromagnetic and weak forces, explains a majority of physical phenomena with remarkable accuracy. However, the theoretical framework that includes the remaining strong force and gravity is still in development. Fully understanding these interactions and integrating them into a comprehensive theory remains one of the significant challenges in modern physics.

To unify gravitational interaction with other interactions, it's necessary to understand gravity at the scale of the early universe. According to inflationary theory, the size of the universe was around the Planck scale, approximately 1.6×10^{-35} m at its inception. To deal with gravity at this scale, quantum mechanics must be applied, suggesting that gravitational values become discrete and thus requiring the breakdown of Lorentz symmetry. Lorentz symmetry breaking, while a fundamental principle in physical laws, could offer a viable solution for treating quantum effects of gravity without contradiction when considering high energies. This approach is regarded as a strong candidate for new quantum gravity theories[2]. If the quantization of gravity is carried out under the assumption that Lorentz symmetry is maintained, quantum corrections become necessary to ensure that physical quantities are calculable as finite values. However, this approach leads to non-renormalizability, posing a significant challenge in the theoretical framework. Superstring theory, proposed to overcome this issue of non-renormalizability, suggests the existence of extra dimensions. This theory implies that gravity might deviate from the inverse square law in microscopic spaces, a concept that has significant implications for our understanding of fundamental physics, particularly at the smallest scales[3].

The quantization of gravity essentially seeks to unify the theory of general relativity, which is based on the principles of equivalence and locality, with the theory of quantum mechanics, founded on the conservation of probability and unitarity. If there are issues in quantizing gravity, it implies that modifications might be necessary in either or both theories. One such modification in general relativity is the Chern-Simons theory. This theory emerges from adding a topological term, known as the Chern-Simons term, to the standard Lagrangian density. It offers an explanation for the flat rotation curves of galaxies without the need to invoke dark matter[4, 5]. Conversely, there are also

research efforts focused on modifying the framework of quantum mechanics itself. These studies aim to address the complexities and challenges encountered in the intersection of quantum mechanics and gravitational theory[6].

In the context of space and black holes, the quantization of gravity is closely related to the singularity problem in Einstein's equations. Einstein's equations describes that the presence of matter causes a distortion in spacetime. However, these equations also lead to singularities, where spacetime curvature becomes infinite, such as within a black hole. To resolve the singularity where spacetime curvature becomes infinite, matter itself would have to vanish, a scenario that is considered unnatural. To tackle this issue, the weak-field approximation was introduced. It assumes that the gravitational field weakens near the center of a black hole, leading to the emergence of a flat spacetime in that region. This approach of using a weak-field approximation has notably influenced the development of Quantum Chromodynamics (QCD). This weak-field approximation has influenced the success of QCD, which was introduced as a theory of strong interactions describing the physics of hadrons such as nuclei.

Observations of stars in the universe, particularly through the analysis of gamma rays emitted by them, indicate that the universe is expanding at an accelerated rate[7]. This accelerated expansion cannot be fully explained by the interstellar gravity known to us, leading to theories about a type of repulsive gravity[8]. This repulsive force is incorporated into Einstein's equations as the cosmological term. In the early universe, this term was insignificant. However, as the universe expanded and the density of matter decreased, the influence of the cosmological term became more pronounced, and it is now believed to be the driving force behind the universe's accelerated expansion. The cosmic microwave background radiation (CMB) studies suggest that this repulsive gravity-like force contributes to about 70% of the total energy in the current universe. Despite its significant impact, the true nature and origin of this force remain one of the biggest mysteries in modern astrophysics and cosmology.

Matter constitutes everything in our observable universe, but during the early stages of the universe's formation, it is believed that antimatter existed in equal quantities to matter. However, the current universe is predominantly composed of matter, a phenomenon thought to result from slight differences in the properties of matter and antimatter. This disparity suggests the presence of CP (Charge Parity) symmetry breaking and non-conservation of baryon number. Research efforts are ongoing to detect and understand these phenomena. The currently known degree of symmetry breaking in CP is quantified at , but this magnitude is not sufficient to fully explain the predominance of matter in the universe. The discrepancies in the currently understood symmetry breaking suggest that additional, yet undiscovered forms of symmetry breaking may have occurred in the early universe.

Quantum Chromodynamics (QCD) has been successful in explaining some aspects of quarks and gluons, the fundamental constituents of hadrons, particularly in the energy region of about GeV. However, QCD has yet to effectively address phenomena in higher energy regions, such as those involving nuclei and neutron stars. Nuclear forces at these higher energy levels play a crucial role in the balance of forces in extreme environments of the universe and in super-dense states created by explosive phenomena. The accurate determination of these forces through lattice QCD is expected to significantly contribute to understanding the mysteries surrounding various cosmic events. These include supernova explosions at the end of stellar evolution, the formation of neutron stars and black holes, mergers of binary neutron stars, and elemental synthesis in the universe, all of which are intricately linked to these explosive phenomena.

In the realm of fundamental physics, experiments utilizing neutron optics have accomplished many significant achievements. This success is largely due to the unique properties of neutrons. As neutrons carry no electric charge and have mass, they enable the verification of interactions coupled with mass, such as gravity, as well as interactions with atomic nuclei, without being influenced by electric fields. Moreover, free neutrons possess an exceptionally long lifetime of about 15 minutes, allowing them to be used as stable particles in various experiments. In the subsequent subsections, we discuss experiments

where neutron optics can be applied to address the aforementioned fundamental physics issues.

1.1.1 Fifth Force

The quantization of gravity and the origin of the accelerated expansion of the universe are hypothesized to involve an unknown interaction coupled with mass. This interaction, not accounted for in the four known fundamental interactions, is often referred to as the "Fifth Force". A common approach to exploring this interaction involves adding a short-range term to Newtonian gravity, which does not diminish the generality of the theory. This interaction is characterized by

$$V(r) = -G\frac{m_1 m_2}{r}\left(1 + \alpha_\mathrm{G} e^{-r/\lambda_5}\right), \tag{1.1}$$

where α_G represents the coupling constant, λ_5 represents the reach distance, G is the gravitational constant, m_1 and m_2 is the mass of the two substances, and r is their distance apart. The existence of a Fifth Force has been a focus of exploratory experiments around the world, and the current findings are well-documented in the reference[9]. These studies have investigated various fifth forces, the details of which are depicted in Figure 1.1. Among the findings, the shortest range of gravity observed to date operates at a distance of 56 μm, with no gravitational effects detected at shorter distances[10]. Search experiments using large accelerators have not even confirmed the existence of an interaction that is 10^{30} orders of magnitude larger than Newtonian gravity[11]. In contrast to charged particles, neutrons are uncharged yet possess mass, enabling them to penetrate into the interior of an atom, a region inaccessible to charged particles. Within this atomic domain, neutrons interact at scales roughly equivalent to the size of an atomic nucleus. This characteristic of neutrons makes them ideal test particles in experimental searches, allowing for the strong limitation of interactions at distances on the order of nanometers. In previous studies, experiments using neutron scattering have provided the strongest limits on fifth forces in the reach range of 10^{-11}–10^{-8} m[12, 13].
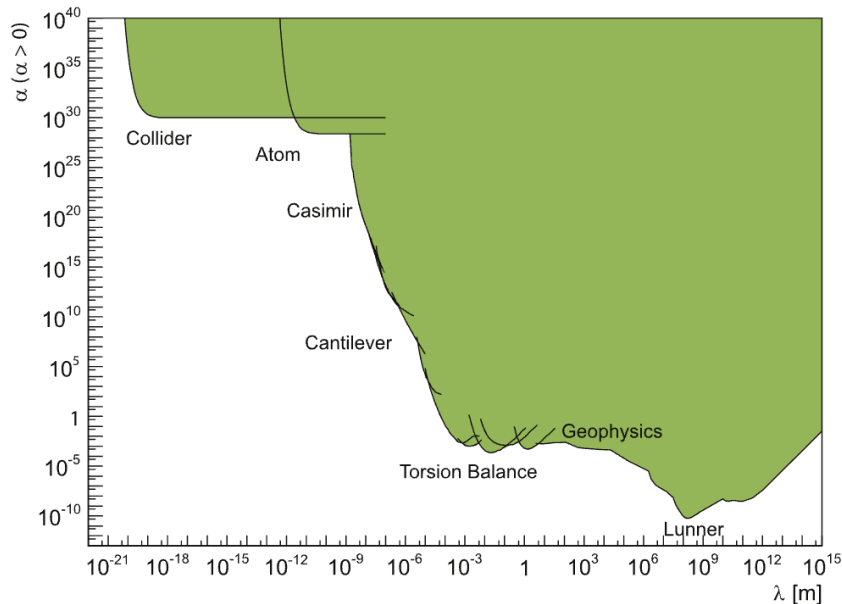
Figure 1.1: Exclusion map of the fifth force.

The chameleon mechanism, one of the fifth forces, has an effective mass that varies depending on the matter density. This mechanism has the potential to explain the origin of the accelerated expansion of the universe, since the mass changes in the distant universe where the matter density is low. Investigations into the chameleon mechanism have predominantly used neutron interferometry, focusing on the phase change of neutron waves as they traverse through matter of different densities[14, 15]. In more recent times, research into this mechanism has expanded, incorporating techniques such as atomic interferometry and experiments with force sensors to explore this concept further[16, 17].

1.1.2   General Relativity

Investigating the gravitational effects on fundamental particles can be effectively done using Earth's gravity. Most common fundamental particles either have negligible mass or are completely massless, and in the case of heavy-mass particles like protons and nuclei, their behavior is predominantly influenced by electrical interactions. In contrast to these particles, neutrons are unaffected by electric fields and thus can be used to measure gravitational forces directly. Neutrons, when their momentum is reduced to an extremely low level, can be trapped by Earth's gravity. This trapping results in a discrete probability distribution of their existence along the vertical or height axis. This discretization is particularly observable with ultra-cold neutrons. In the relevant literature, it has been shown that the search sensitivity for these gravitational effects can be enhanced by ensuring the flatness of the guide mirrors of neutrons and by developing techniques to isolate minor variations in the measurement position[18]. Neutron interferometer experiments are capable of measuring differences in Earth's gravitational potential by directing neutrons along two separate paths at varying heights. Past studies in this field have sparked debate, particularly when observed deviations of up to 12% from theoretical values were reported[19]. These results were subsequently re-examined in a follow-up experiment, achieving an accuracy of 0.8%[20]. However, there remains a desire for further improvement in measurement sensitivity to deepen our understanding of gravitational effects on neutrons.

The current theory of general relativity posits that gravitational waves are produced through the interactions between massive objects[21]. Primordial gravitational waves, thought to have originated in the early stages of the universe's formation, provide a means to observe phenomena from a time before the universe became transparent, which is not possible with optical methods. Gravitational waves are primarily detected using laser interferometry. In contrast, the use of neutron interferometry has gained interest due to its advantages, such as allowing for longer interaction times and eliminating mirror noise[22].

Chern-Simons modified gravity, a theory that alters the conventional understanding of gravity, suggests that the path integral of waves traveling along two different elevations changes over time[23]. This change can be observed in the influence of relativistic Sagnac effect measurement with the Lense-Thirring effect. It has been proposed to investigate this phenomenon by making precise time-variant measurements of the Sagnac effect using neutron interferometry, building on previous observations[24].

1.1.3   Quantum Mechanics

Quantum mechanics, constructed based on empirical principles, has seen proposed modifications aimed at achieving a unified description with general relativity. A fundamental aspect of quantum mechanics, the 4π symmetry of fermions, was experimentally verified using neutron interferometry[25]. This involved measuring the phase shift of polarized neutrons in a magnetic field. In addition, the experiment observed the Sagnac effect extended for the quantum mechanism by applying a rotating magnetic field to polarized neutrons[26]. This effect is a result of the interaction between the neutron spin and the angular velocity of the rotating field. Observations in quantum mechanics are generally confined to determining a particle's final state. However, by conducting measurements that limit the information to the bare minimum, it's possible to observe particles in a superposition of wave functions.

This method is known as weak measurement and is crucial for exploring quantum paradoxes and deepening the understanding of quantum mechanics, such as the implications of the Dirac equation and the concept of weak values. These weak measurements have been experimentally validated using neutron interferometry with polarized neutrons, providing significant insights into the nuances of quantum mechanics[27].

1.1.4 Symmetry Breaking

CP symmetry breaking implies that either parity or charge conservation is not upheld in matter and antimatter. This phenomenon has been validated through the measurement of 2π decay of K meson, and so on[28, 29, 30]. However, a more substantial degree of symmetry breaking is necessary to explain the current matter-dominated universe. CP symmetry breaking can be verified as time-reversal symmetry breaking by using the CPT theorem. This effect is explored by measuring the absorption cross-section of polarized epithermal neutrons at the polarized target[31, 32, 33].

The breaking of CP symmetry can also be investigated by searching for the electric dipole moment (EDM) of neutrons[34]. Neutrons, though electrically neutral, are known to possess an internal charge structure. The asymmetry in the charge distribution within nucleons is a phenomenon that instantaneously breaks CP symmetry and has been extensively studied. Currently, experiments using stored ultra-cold neutrons provide the most stringent constraints on this search[35]. However, improving the sensitivity of these searches beyond current levels is fundamentally challenging. Therefore, proposals have been made to enhance search sensitivity by utilizing multiple methods, such as beam techniques and diffraction methods[36, 37].

Baryon number violation predicts the existence of neutron-antineutron oscillations[38]. Similar to flavor oscillations in neutrinos, this phenomenon involves neutrons transforming into antineutrons. Left-right symmetric Grand Unified Theories, which predict massive right-handed neutrinos, anticipate this neutron-antineutron oscillation to occur within a range of 10^9–10^{10} seconds[39]. The phenomenon can be explored by allowing free neutrons to travel a long distance of 76 m. The lower limit of this oscillation period has been investigated in experiments conducted at the ILL reactor, establishing a lower bound of $\tau_{n\bar{n}} > 8.6 \times 10^7$ seconds for the neutron-antineutron oscillation period[40]. Several new experiments have been proposed to improve the scope of the search to the area predicted by the new theories[41].

The theoretical framework aimed at resolving the issue of quantizing gravity necessitates the existence of Lorentz symmetry breaking[42]. Lorentz symmetry breaking introduces an anisotropic effect that varies based on the direction of a particle's momentum[43]. Neutrons, with their substantial mass, are particularly useful probes in such search experiments, as they possess large momentum even at relatively low energies. When neutrons travel along two non-parallel paths, Lorentz symmetry breaking leads to differing momentum changes, resulting in a phase shift. This phase shift can be investigated using a non-parallel neutron interferometer. Notably, this setup suggests the possibility of observing daily periodicity variations in the phase shift due to the Lorentz symmetry breaking[44].

1.1.5 Nuclear Structure

In the construction of lattice Quantum Chromodynamics (QCD) theory, continuous spacetime is approximated using a "lattice", onto which QCD is defined for numerical calculations. However, due to the immense computational requirements, calculations are currently limited to two-body problems. Understanding the behavior of nuclei composed of multiple nucleons is still in the development stage. Various methods are used for three-body calculations, however, each of these theories is incomplete[45]. To evaluate these theories, precise measurements of nucleon-nucleon interactions are required. Neutron interferometry can contribute to this field by measuring the nuclear scattering lengths of neutrons with

light elements such as protons, deuterons, and helium. These measurements provide experimental values that are crucial for assessing and refining theoretical models in nuclear physics[46, 47, 48, 49].

1.2 Neutron Optics

In the previous section, we delved into the remarkable history of neutron optics, highlighting how these physics experiments have been conducted within the unique environment provided by neutron optics. In this section, we will focus on describing the basic properties of neutron optics.

Non-relativistic neutrons are known to behave as de Broglie waves according to the following equation:

$$E = \frac{\hbar^2 k^2}{2m_{\mathrm{n}}} = \frac{h^2}{2m_{\mathrm{n}}\lambda^2} = \frac{1}{2}m_{\mathrm{n}}v^2 \hat{=} k_{\mathrm{B}}T, \tag{1.2}$$

where the E is kinetic energy, h is Plank constant, $\hbar$ is Dirac constant, and m_{n} is neutron mass. The wave vector k is proportional to the square root of E. This value has the following relationship to the momentum p:

$$p = \hbar k = m_{\mathrm{n}}v = h/\lambda. \tag{1.3}$$

The neutron wavelength λ is inversely proportional to the square root of E. The neutron velocity v is proportional to the k. The averaged temperature of neutrons T in the thermodynamic equilibrium state follows a Maxwell–Boltzmann distribution, where the k_{B} is the Boltzmann constant. Neutrons are assigned different designations depending on their kinetic energy (Figure 1.2). A typical neutron cooled to near room temperature ($T = 300$ K) has the characteristics of

$$E \simeq 25 \text{ meV}, \ \lambda \simeq 0.18 \text{ nm}, \ v \simeq 2200 \text{ m/s}. \tag{1.4}$$

Noteworthy is the wavelength of neutrons is almost the same as that of X-rays. This similarity means that optical phenomena such as interference, reflection, refraction, and diffraction, which are commonly utilized in X-ray studies, can also be applied to neutron studies. In this dissertation, the field that leverages these characteristics of neutrons is referred to as neutron optics, and neutrons within the energy range addressed by neutron optics are referred to as low-energy neutrons.

			Neutron Optics			
Energy	10^5 eV	10 eV	25 meV	10^{-3} eV	10^{-6} eV	
Temperature	10^9 K	10^5 K	300 K	10 K	10^{-2} K	
Wavelength	10^{-13} m	10^{-11} m	0.18 nm	10^{-9} m	10^{-7} m	
	fast neutron	epithermal neutron	thermal neutron	cold neutron	very-cold neutron	ultra-cold neutron

Figure 1.2: Correlation between neutron energy and generic designations.

Neutrons have the ability to penetrate into the interior of an atom due to their electrical neutrality, which causes neutron scattering to be primarily influenced by the potential of the nucleus. Since

the effective radius of the potential is about a few femtometers, and considering that the wavelength of low-energy neutrons is approximately 10^5 times larger than the nuclear potential, neutrons are unable to discern individual nuclei and can only detect the averaged potential. This property of neutrons eliminates the necessity to consider individual scattering events in neutron optical phenomena. Consequently, this allows for discussions and analyses to be conducted in a semiclassical framework.

The upcoming subsections provide a description of the major behavior of neutron optics: interference, reflection, refraction, and diffraction, with an explanation of the basic laws of quantum mechanics. In addition, facilities and detectors essential for neutron experiments will be introduced. These subsections can be skipped if they are not relevant to your needs.

1.2.1 Basic Characteristics

The phenomena in neutron optics are described using the general theory of quantum physics. The matter-wave fields are described by the Schrödinger equation using Hamiltonian $\mathcal{H}$:

$$\mathcal{H}\Psi(\mathbf{r},t) = \left(-\frac{\hbar^2}{2m}\nabla^2 + V(\mathbf{r},t)\right)\Psi(\mathbf{r},t) = i\hbar\frac{\partial\Psi(\mathbf{r},t)}{\partial t}, \tag{1.5}$$

where the V is static potential. These equations are linear and solvable in free space using a plane wave approach:

$$\Psi(\mathbf{r},t) = Ae^{i(\mathbf{k}\cdot\mathbf{r}-\omega t)}, \tag{1.6}$$

where the ω is the angular frequency, and the A is normalized parameter. This value is given such that the probability of existence of the particle, determined by the square of the wave function, is 1. A wave packet in free space composed of multiple wave functions can be written as a superposition of plane waves.

$$\Psi(x,t) = \frac{1}{\sqrt{2\pi}}\int_{-\infty}^{+\infty} g(k)e^{i(kx-\omega t)}\,dk \tag{1.7}$$

where $g(k)$ is an eigenvalue. When considering a Gaussian distributed wave packet, its wave function can be written as a wave packet localized at $x = x_0$. In this case, the eigenvalues are written as

$$g(k) = \frac{1}{(2\pi\sigma_k^2)^{1/4}}\exp\left[-\frac{(k-k_0)^2}{2\left(\sqrt{2}\sigma_k\right)^2}\right] \tag{1.8}$$

The spatial extent of the wave function Δx and the momentum extent Δp are written by the square root of the mean of the squares of the deviations from the expected values $\langle x\rangle$ and $\langle p\rangle$, respectively.

$$\Delta x \quad = \sqrt{\langle(x-(x))^2\rangle} \tag{1.9}$$
$$\Delta p \quad = \sqrt{\langle(p-(p))^2\rangle} \tag{1.10}$$

Calculating the spread using the expectation value obtained from the integral of Eq. (1.8), we can write

$$\Delta x\Delta p = \frac{\hbar}{2} \tag{1.11}$$

This is the minimum value that can be expected from the uncertainty principle, indicating that the position and momentum of the wave cannot be determined simultaneously.

The velocity of an isotropic wavefront can be expressed as ω/k, using the fact that the phase of the wavefunction is constant, i.e. $kr-\omega t$ in Eq. (1.6) is constant. This velocity is called the phase velocity and is written as

$$v_{\mathrm{p}} = \frac{\omega}{k}, \tag{1.12}$$

This phase velocity relates the de Broglie wavelength to the frequency of the matter wave. In contrast, the speed of travel of the wave packet is determined by the speed of travel of the probability density of the equation. This value is given by the following equation:

$$v \equiv \frac{d\omega}{dk} = \frac{\hbar k}{m} = 2v_{\mathrm{p}} \tag{1.13}$$

This v is called the group velocity and is related to the velocity of matter in de Broglie's relation.

1.2.2 Interference

Consider the situation where two wave functions with the same phase origin overlap. The wave functions $\Psi(x,t)$ separated into two paths can be written with a phase difference ϕ as follows:

$$\Psi_{\mathrm{I}}(x,t) = \frac{a_{\mathrm{I}}}{\sqrt{2\pi}} \int g(k) e^{i(kx-\omega t)} \, dk, \tag{1.14}$$

$$\Psi_{\mathrm{II}}(x,t) = \frac{a_{\mathrm{II}}}{\sqrt{2\pi}} \int g(k) e^{i(kx-\omega t)} e^{\phi} \, dk. \tag{1.15}$$

Here, a_{I} and a_{II} are normalization constants that satisfy $a_{\mathrm{I}}^2 + a_{\mathrm{II}}^2 = 1$ when absorption is ignored. The $g(k)$ is the eigenvalue parameter shown in Eq. (1.8). The phase shift ϕ can be expressed using the phase ϕ_0 of the wave function before separation and the optical path length difference L_0 between the two paths as:

$$\phi = \phi_0 + L_0 \left(k - k_0 \right). \tag{1.16}$$

The observed wave function is obtained by the superposition of these two wave functions:

$$\int |\Psi_{\mathrm{sup}}|^2 \, dx = \int |\Psi_{\mathrm{I}} + \Psi_{\mathrm{II}}|^2 \, dx \tag{1.17}$$

$$= a_{\mathrm{I}}'^2 + a_{\mathrm{II}}'^2 + 2a_{\mathrm{I}}' a_{\mathrm{II}}' \exp\left[-\frac{1}{2} \left(\sigma_k L_0 \right)^2 \right] \cos\phi_0 \tag{1.18}$$

When the two wave functions overlap, in addition to the sum of the probabilities of each wave function $a_{\mathrm{I}}'^2 + a_{\mathrm{II}}'^2$, a periodically varying term is added, observable as interference. To quantify the degree of interference, a value defined by the standard deviation of the wave packet and the optical path length difference is given as:

$$\Gamma(L) = \exp\left[\left(-\sigma_k L \right)^2 / 2 \right] \tag{1.19}$$

With a fixed wave number dispersion, the optical path length difference that makes $\Gamma = 1/e$ is called the coherence length L^c, and can be written as:

$$\sigma_k L^c = \sqrt{2} \tag{1.20}$$

This value is a parameter that determines the coherency of matter waves, and the experimental setup needs to be constructed to fit within the range of the coherence length.

Neutron interference was demonstrated by the realization of neutron interferometer[50]. Subsequently, neutron double-slit experiments and other experiments have clearly demonstrated the wave nature of neutrons[51].

1.2.3   Scattering

Next, we consider the scattering of neutrons by the time-independent potential $V(\mathbf{r})$. In this case, the time-dependent terms of the wave function in Eq. (1.6) can be regarded as constants:

$$\Psi(\mathbf{r}, t) = \psi(\mathbf{r})e^{-i\omega t}, \tag{1.21}$$

and the Eq. (1.5) can be expanded as follows:

$$\left[-\frac{\hbar^2}{2m}\nabla^2 + V(\mathbf{r}) \right] \psi(\mathbf{r}) = E\psi(\mathbf{r}), \tag{1.22}$$

which is the time-independent Schrödinger equation. We can describe the incident particle as a plane wave approaching the target in the region where the potential has no effect. The incident plane wave can be expressed according to the Eq. (1.22) as follows:

$$\psi(\mathbf{r}) = e^{i\mathbf{k}\cdot\mathbf{r}}. \tag{1.23}$$

The majority of these particles propagate directly as transmission waves, while a portion of them, scattered by particles within the target, can be represented as outward spherical waves. The neutron wave field outside the nucleus ($R \ll r$) can be expressed by adding a spherical wave term as follows:

$$\psi(\mathbf{r}) = e^{ikz} + f(\theta, \phi)\frac{e^{ikr}}{r}, \tag{1.24}$$

where $f(\theta, \phi)$ is the scattering amplitude. The potential $V(\mathbf{r})$ responsible for the scattering can be defined in accordance with condition $kR \ll 1$ as follows:

$$V(\mathbf{r}) = \begin{cases} -U & (r < R) \\ 0 & (r > R) \end{cases} \tag{1.25}$$

The wave equation for the scattered wave by the potential can be written using the Lippmann-Schwinger equation, which is widely known as the equation to solve scattering states.

$$\psi(k; \mathbf{r}) = e^{i\mathbf{k}\cdot\mathbf{r}} - \frac{2m}{\hbar^2} \int d^3r' \frac{e^{+ik|\mathbf{r}-\mathbf{r}'|}}{4\pi|\mathbf{r}-\mathbf{r}'|} V(\mathbf{r}')\, \psi(k; \mathbf{r}') \tag{1.26}$$

It can be readily verified that applying the operator $(\nabla^2 + k^2)$ to this equation indeed returns us to the original Schrödinger equation Eq. (1.22). The Lippmann-Schwinger equation represents an integral equation, serving as a reinterpretation of the more conventional Schrödinger differential equation. It does not provide a solution to the Schrödinger equation itself, as there is still a need to determine what that solution entails. Considering the limit of $r \to \infty$ for comparison with Eq. (1.24), Eq. (1.26) can be written using the first Born approximation and the condition of $r \gg r'$:

$$\psi(\mathbf{r}) = e^{i\mathbf{k}\cdot\mathbf{r}} - \frac{2m}{\hbar^2}\frac{1}{4\pi} \left[\int d^3r' e^{i\mathbf{q}\cdot\mathbf{r}'} V(\mathbf{r}') \right] \frac{e^{ikr}}{r}, \tag{1.27}$$

where

$$\mathbf{q} = \mathbf{k} - k\hat{\mathbf{r}} \tag{1.28}$$

can be thought of as the momentum transfer from the incoming wave to the outgoing wave. Due to the scattering amplitude can be written by the comparison between Eq. (1.24) and Eq. (1.27), the following equation is obtained

$$f(\theta, \phi) \approx -\frac{m}{2\pi\hbar^2} \left[\int d^3r' e^{i\mathbf{q}\cdot\mathbf{r}'} V(\mathbf{r}') \right] \tag{1.29}$$

Since neutrons are primarily scattered by nuclei, the interaction length R of the potential is significantly shorter than the wavelength of the neutron. As this condition renders $kR \ll 1$ valid, it allows us to make the approximation of $e^{i\mathbf{q}\cdot\mathbf{r}'} \simeq 1$, and we need to consider only the s-wave for the scattered waves. Utilizing these connections, Eq. (1.29) can be expressed as:

$$f(\theta, \phi) = -\frac{m}{2\pi\hbar^2}\tilde{V}(\mathbf{r}). \tag{1.30}$$

Since the condition of $kR \ll 1$, the potentials can be treated as point sources, and neutrons can be seen as undergoing scattering by point potentials with a number density N. Furthermore, since the mass of the scatterer is considerably larger than the mass of the neutron, the parameter in Eq. (1.30) can be regarded as $m = m_{\mathrm{n}}$. Under these conditions, Eq. (1.30) yields the following relationship:

$$U_{\mathrm{F}} = \frac{2\pi\hbar^2}{m_{\mathrm{n}}}bN \tag{1.31}$$

where b is called the "scattering length" and represents the scattering amplitude by the nucleon. The U_{F} represents is called the "Fermi pseudopotential". These values serve as fundamental parameters extensively employed in neutron experiments, offering a concise and lucid depiction of neutron-nucleon interactions.

Next, we consider the wave function around the scattering potential. Inside the nucleus, the exact s-wave regular solution of the Schrödinger equation is

$$\psi(r) = A\frac{\sin Kr}{Kr}, \tag{1.32}$$

where

$$K^2 = 2m\frac{E - U_{\mathrm{F}}}{\hbar^2}. \tag{1.33}$$

The constants A and b need to be tuned to ensure the continuity of both ψ and $d\psi/dr$ at the surface of the nucleus ($r = R$). In the vicinity of the nuclear surface, where kr is very small, we can write Eq. (1.24) as follows:

$$\psi \approx 1 - \frac{b}{r} \tag{1.34}$$

in the region of $r > R$. The boundary conditions necessitate us to seamlessly connect this function to the rapidly oscillating wavefunction Eq. (1.32) within the nucleus, as illustrated in Figure 1.3. In the limit of $kR \to 0$, the boundary conditions entail the following:

$$A\frac{\sin KR}{K} = R - b \tag{1.35}$$

and

$$A\cos KR = 1 \tag{1.36}$$

As indicated by the equation and the diagram, the wavefunction undergoes distortion due to the intense potential of the nucleus, resulting in multiple oscillations within the potential well. The nuclear scattering length exhibits significant variations with even slight adjustments in the potential depth R.

It is evident that neutrons undergo scattering by a potential characterized by a nuclear scattering length. The interaction of neutrons with potentials results not only in scattering but also in absorption. This effect can be expressed by extending the scattering length to complex numbers:

$$b = b_{\mathrm{scat}} + ib_{\mathrm{abs}}. \tag{1.37}$$
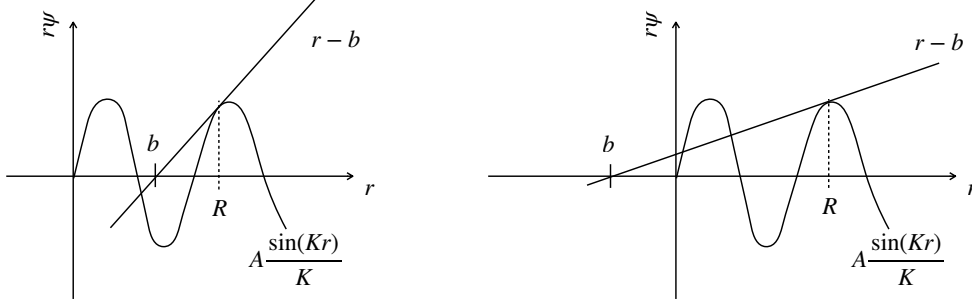
Figure 1.3: Diagram showing the matching of the neutron wave function.

The parameter b_{scat} can be categorized into two groups: coherent scattering lengths b_{c}, which do not involve the change of momentum in the scattering process, and incoherent scattering lengths b_{inc}, which encompass the change of momentum. Absorption reactions b_{abs} encompass both fission reactions, in which nuclei split, and capture reactions, where neutrons are absorbed by nuclei. For nuclei with magnetic structures, the magnetic scattering length can be used to describe them:

$$b = b_{\text{coh}} \pm b_{\text{mag}}, \tag{1.38}$$

where the sign associated with the magnetic scattering length is determined by the direction of polarization of the neutron with respect to the polarized material. Theoretical calculations of the interaction between neutrons and potentials can be challenging due to the sensitivity of the phase to even minor changes in the potential. Consequently, we often use experimental values[52]. Here, the scattering lengths of representative nuclei are shown in Table 1.1.

Table 1.1: Scattering lengths of representative nuclei.

Material	Si	Ge	Ni	Ti	Al	V
Coherent scattering length [fm]	4.1491	8.185	10.3	−3.438	3.449	−0.3824

The total neutron scattering cross section σ is expressed by the following equation:

$$\sigma = 4\pi b^2. \tag{1.39}$$

This cross-section can be classified into scattering cross-section (σ_{s}) and absorption cross-section (σ_{a}) as well as scattering length. Each cross-section can be written using the scattering length b as follows:

$$\sigma_{\text{s}} = 4\pi \left(\text{Re } b\right)^2 \tag{1.40}$$

$$\sigma_{\text{a}} = -\frac{4\pi}{k}\text{Im } b \tag{1.41}$$

The absorption cross-section is generally inversely proportional to the velocity of the neutron. Also, the beam attenuation satisfies the Lambert's law:

$$\frac{I}{I_0} = \exp\left[-\left(\sigma_{\text{a}} + \sigma_{\text{s}}\right) ND\right], \tag{1.42}$$

where the I_0 is the initial intensity, the I is the attenuated intensity, and the D is the interaction length. These cross-section values have been measured experimentally and summarized in the database, e.g. JENDL[53]. Absorption cross sections for materials commonly used in laboratory equipment, such as metals, are 0.231 barn for aluminum and 2.56 barn for iron. Furthermore, the absorption cross sections of silicon, which is often used as an irradiation sample, is 0.171 barn. To achieve a transmittance of $1/e$, it is necessary to prepare a sample of several milli-centi meters. For some nuclei, such as ^{139}La, ^{113}Cd, and ^{131}Xe, resonant absorption can be observed in the low-energy region of epithermal neutrons. This resonance reaction is internalized in the absorption cross-section and emits gamma rays as it returns to the ground state.

The discussion of the preceding Eq. (1.31) emphasizes that neutrons have a phase shift based on the mean potential produced by the nucleus during scattering. This can be thought of as a refraction by the scatterer. With the incident wave vector denoted as k and the wavenumber inside the scatterer also represented as K, the refractive index n can be established by employing the ratio of them, as follows:

$$n \equiv \frac{K}{k}.$$
(1.43)

This can be written using the potential U and the kinetic energy E of the scatterer as follows

$$n^2 = 1 - \frac{U}{E} = 1 - \frac{bN\lambda^2}{2\pi}$$
(1.44)

The refraction index can be acquired by solving the Schrödinger equation for a neutron traversing a potential U:

$$n \simeq 1 - \frac{\lambda^2 N}{2\pi} \sqrt{b_{\mathrm{c}}^2 - \left(\frac{\sigma_{\mathrm{r}}}{2\lambda}\right)^2} + i\frac{\sigma_{\mathrm{r}} N\lambda}{4\pi}$$
(1.45)

where the σ_{r} is the cross-section expected of coherent term, which is written as $\sigma_{\mathrm{r}} = \sigma_{\mathrm{a}} + \sigma_{\mathrm{inc}}$. Since the imaginary part is small in most cases, the following relation is used:

$$n = 1 - \frac{\lambda^2 N b_{\mathrm{c}}}{2\pi}$$
(1.46)

This value is about $1-n \simeq 10^{-5}$ for a typical nuclide, which is slightly less than 1. The refraction angle θ' is larger than the incident angle θ in the case of reflected by the general material with refractive index n. In other words, neutron reflections are always accompanied by refracted waves.

1.2.4 Diffraction

We consider the wave function of a neutron incident on a scatterer such as a single crystal with periodic potential. If the periodic potential can be written as $\mathbf{R}$ in Bravais lattice, the wave function ψ satisfies the following conditions

$$\psi_j (\mathbf{r} + \mathbf{R}_{\mathrm{j}}) = \psi_j (\mathbf{r})$$
(1.47)

In this case, the wave function of the scattered wave that satisfies the wave equation Eq. (1.22) can be written as

$$\psi (\mathbf{r}) = \sum_q \psi_q e^{i\mathbf{q}\cdot\mathbf{r}}$$
(1.48)

where the ψ_q is the scattering amplitude, and q is the momentum transfer of scattered wave. This equation is just a rewriting of Eq. (1.27) with periodic boundary conditions. When the reciprocal lattice vector obtained from the Bravais lattice $\mathbf{R}$ is $\mathbf{H}$, the condition that the scattered waves enhance each other can be written from the Laue condition as

$$\mathbf{q} = \mathbf{k} - \mathbf{k}' = \mathbf{H}$$
(1.49)

where the $\mathbf{k}$ is the wave vector of incident neutron, $\mathbf{k}'$ is the wave vector of scattered wave. When considering coherent scattering, the wave vector satisfies

$$|\mathbf{k}| = |\mathbf{k}'| = k = \frac{2\pi}{\lambda} \tag{1.50}$$

since the wavelength does not change before and after scattering. If the direction of wave travel changes by 2θ before and after scattering, the wave vector satisfies

$$2k^2 - 2k^2 \cos 2\theta = |\mathbf{H}|^2 , \tag{1.51}$$

This is exactly Bragg's condition, which can be written as follows

$$2k \sin \theta = |\mathbf{H}| \tag{1.52}$$

Neutrons can be observed diffracting at wavelengths and angles that satisfy the Bragg condition for periodic potentials. This is one of the most widely known phenomena in neutron optics.

In the case of a single crystal sample, the diffraction direction is determined by the reciprocal lattice vector created by the crystal. The configuration in which the reciprocal lattice vectors are perpendicular to the crystal surface is called Bragg geometry, and the configuration in which they are parallel is called Laue geometry. Each configuration is shown in Figure 1.4. In Laue geometry, diffracted neutrons penetrate the crystal, so the combination of a sample with a small absorption cross section and highly penetrable neutrons is suitable for observation.
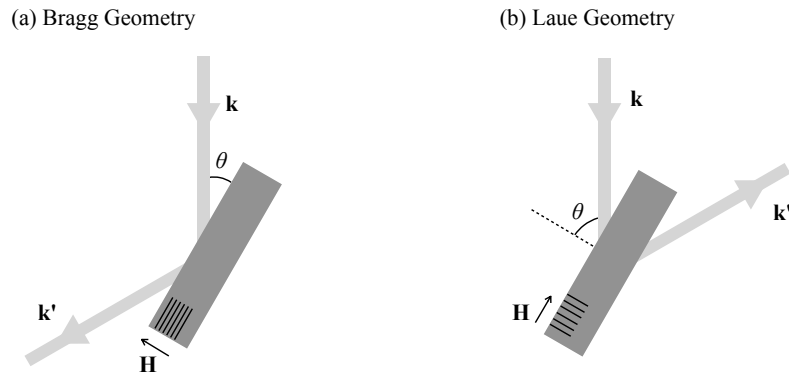
Figure 1.4: The diffraction configurations of (a) Bragg geometry and (b) Laue Geometry.

When considering diffraction by a single crystal of a certain thickness, the diffracted wave vector satisfies the equation $k' - k = H$, meaning the diffracted beam with wave vector k' meets the Bragg condition of $-H$ and is rescattered by the incident beam. Generally, a "dynamical" interchange of neutron intensity is expected between the incident beam direction and the Bragg diffraction beam direction within the crystal medium. This phenomenon is known as the dynamical diffraction of neutrons, leading to multiple scattering of the incident wave. Waves incident on a single crystal sample are characterized by waves propagating along the crystal lattice planes and those propagating between the lattices, which two states are called α and β state. Each type of wave function inside the crystal is distinguished by a slight difference in refractive index, resulting in four-wave functions: one for the reflection direction with α and β state and another for the forward direction with α and β state. Waves

exiting the crystal can be described by two wave functions, which are superimposing α and β states. This allows the observation of wave interference inside the crystal, with a position distribution in each direction, as shown in Figure 1.5. These interference patterns are known as pendellösung interference fringes. The periodicity of these fringes can be described using the pendellösung length, denoted as Δ_H. When observing these interference fringes, their representation at a detection position Γ can be expressed as follows:

$$I_0(\Gamma) = \frac{1 - \Gamma}{(1 + \Gamma)\sqrt{1 - \Gamma^2}} \cos^2\left[\frac{\pi D}{\Delta_H}\sqrt{1 - \Gamma^2} + \frac{\pi}{4}\right] \tag{1.53}$$

$$I_H(\Gamma) = \frac{1}{\sqrt{1 - \Gamma^2}} \sin^2\left[\frac{\pi D}{\Delta_H}\sqrt{1 - \Gamma^2} + \frac{\pi}{4}\right] \tag{1.54}$$

The diffraction intensity depends on the pendellösung length and the thickness of the crystal, and its period decreases with distance from the beam center ($\Gamma \to 1$). For a more detailed discussion, see Chapter 4.
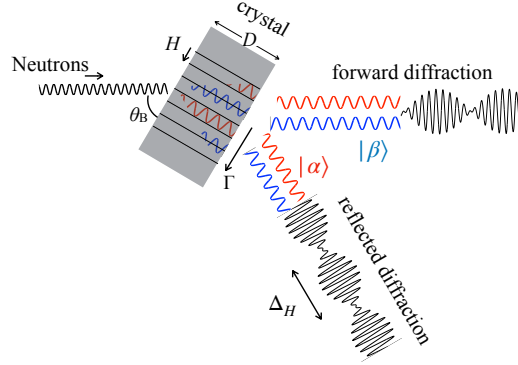
Figure 1.5: Experimental configuration of pendellösung interferogram.

1.2.5 Reflection

Neutrons scattered into matter interact with nuclei through Fermi pseudopotentials, not distinguishing individual nuclei. In the scenario where a neutron approaches a uniform bulk potential U_F on the xy plane, the potential, and force act exclusively in the direction perpendicular to the surface since the surface lacks structural features. For a neutron incident from a region $z > 0$ to a stationary potential U_F in the region $z \leq 0$, the wave function can be written as

$$\psi(z) = \begin{cases} Ae^{-ikz} + Be^{ikz} & (z > 0) \\ Ce^{ikz} & (z \leq 0). \end{cases} \tag{1.55}$$

Letting the incident neutron wave vector be $\mathbf{k} = (k\sin\theta_i, 0, k\cos\theta_i)$, the wave vector interacted by potential can be written using the condition that the wave functions in each region are continuous at the boundaries:

$$\mathbf{k}_r = (k\sin\theta_i, 0, -k\cos\theta_i), \tag{1.56}$$

$$\mathbf{k}_t = (k\sin\theta_i, 0, vk\cos\theta_i). \tag{1.57}$$

where the $\mathbf{k}_{\mathrm{r}}$ is the reflected neutron wave vector, and $\mathbf{k}_{\mathrm{t}}$ is the refracted neutron wave vector. This process is analogous to the classical reflection of light, as shown in Figure 1.6. Assuming the wave function remains continuous at the interface and the interaction is elastic, the conservation of momentum dictates that the incident and reflection angles are equal. For total reflection to occur, the energy of the neutron's normal component must be less than the potential, leading to the following equation:

$$\sin^2 \theta_{\mathrm{i}} < \frac{U_{\mathrm{F}}}{E_z} \tag{1.58}$$

The transmitted neutron is influenced by the material's refractive index, making Snell's law applicable to its refractive angle, denoted as θ_{t}:

$$\cos \theta_{\mathrm{i}} = n \cos \theta_{\mathrm{t}} \tag{1.59}$$

These characteristics are typical of neutron optics, demonstrating that neutrons reflect and refract similarly to light. The momentum of the reflected wave can be written from the law of conservation of momentum as

$$q = \frac{4\pi \sin \theta_{\mathrm{i}}}{\lambda} \tag{1.60}$$

Since the one-to-one correspondence between neutron momentum transfer and kinetic energy is established, the upper limit of reflectable momentum transfer can be determined.
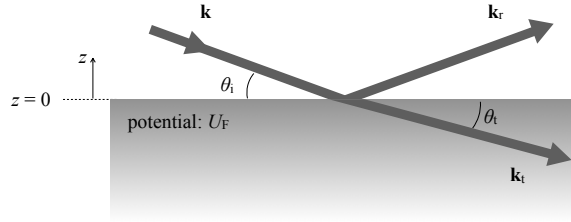
Figure 1.6: The reflection and refraction by the flat surface.

Next, consider the reflection of neutrons on a thin film. For neutrons incident from the region $z > 0$, if potential U_{F} exists in the region $0 \le z \le d$, the wave function can be written as

$$\psi(z) = \begin{cases} Ae^{-ikz} + Be^{ikz} & (z < 0) \\ De^{-ikz} + Fe^{ikz} & (0 \le z \le d) \\ Ce^{ikz} & (d < z). \end{cases} \tag{1.61}$$

There are two types of waves in each region, one traveling in the same direction as the incident particle and the other reflecting. By solving this wave equation with the boundary conditions satisfied, the reflection rate R and transmission rate T can be determined:

$$R = \left| \frac{B}{A} \right|^2 = \left[1 + \frac{4(E - U_{\mathrm{F}})E}{V^2 \sin^2 k'd} \right]^{-1}, \tag{1.62}$$

$$T = \left| \frac{C}{A} \right|^2 = \left[1 + \frac{U_{\mathrm{F}}^2 \sin^2 k'd}{4E(E - V)} \right]^{-1}. \tag{1.63}$$

The reflectivity of neutrons depends on the potential depth, which is related to the tunneling effect. The incident neutrons are reflected by two interfaces, which are the first and second layers. The

reflected neutron is represented by a composite function of the waves reflected by the two interfaces. These reflected waves interfere based on their phase shift, which is linked to the optical path difference and, consequently, the layer's thickness. The thickness of the layer determines which neutrons can be reflected, a concept aligned with the classical Bragg's law. The wavelength of reflected neutrons depends on the characteristic of the layer, which can be understood by the classical Bragg's law.

$$n\lambda = 2d\sin\theta \tag{1.64}$$

where n is a natural number that determines the diffraction order. The wavelength of the reflected neutron depends on the angle of incidence θ and the thickness d of the thin film, which produces interference oscillations called Kiessig fringes depending on the diffraction order. These oscillations reflect the potential and thickness of the thin film, and the period of the fringes shortens with increasing thickness. By examining the wavelength or angle of incidence dependence of these reflectances, the properties of the thin film layer can be studied.

In a material with multiple layers of thin films, Bragg reflection occurs at the boundaries of each layer. When layers with different potentials are stacked alternately with a periodicity of d, the momentum transfer of neutrons capable of reflection aligns with the Bragg condition, which is dependent on the stacking period. To calculate reflectivity in detail, we should consider the wave function. At the interface of the j-th layer, only the normal component of the wave function should be taken into account. The wave function $\psi_j(z)$ is given by

$$\psi(z) = f_j^t e^{ik_j z} + f_j^r e^{-k_j z} \tag{1.65}$$

where f^t and f^r denote the amplitudes of the waves in the incident and reflected directions. The j-th and $j+1$-th wave functions can be written as follows using their continuity

$$\begin{pmatrix} f_j^t \\ f_j^r \end{pmatrix} = M_{j+1} \begin{pmatrix} f_{j+1}^t \\ f_{j+1}^r \end{pmatrix} \ j = 0, 1, 2, ,, n \tag{1.66}$$

where n denotes the total number of layers and M is operator, which is written as

$$M_{j+1} = \frac{1}{2} \begin{pmatrix} \left(1 + \frac{k_{j+1}}{k_j}\right) e^{i(k_{j+1}-k_j)z} & \left(1 + \frac{k_{j+1}}{k_j}\right) e^{i(k_{j+1}+k_j)z} \\ \left(1 - \frac{k_{j+1}}{k_j}\right) e^{i(k_{j+1}+k_j)z} & \left(1 + \frac{k_{j+1}}{k_j}\right) e^{i(k_{j+1}-k_j)z} \end{pmatrix} \tag{1.67}$$

The amplitude of the reflected wave can be expressed as f_0^r and f_n^t. In the case that the amplitude of the incident wave is $f_0^t = 1$ and $f_n^r = 0$, the amplitude is composed of this equation:

$$\begin{pmatrix} 1 \\ R \end{pmatrix} = M_1 \cdot M_2 \cdot ... \cdot M_n \begin{pmatrix} T \\ 0 \end{pmatrix} = \begin{pmatrix} M_{11} & M_{12} \\ M_{21} & M_{22} \end{pmatrix} \begin{pmatrix} T \\ 0 \end{pmatrix} \tag{1.68}$$

From these equations, the amplitudes of the reflected and transmitted waves are given by

$$T = \frac{1}{M_{11}}, \ R = \frac{M_{21}}{M_{11}}. \tag{1.69}$$

The reflected and transmitted wave intensities are given by $\bar{T} = T \cdot T$ and $\bar{R} = R \cdot R$, respectively. The M component is determined by the potential and thickness of the stacked thin films. For a detailed description of these, see Ref.[54].

By alternately layering two materials with distinct potentials at a set period d, neutron reflectivity is enhanced by the Bragg diffraction provided by Eq. (1.64). Nickel (Ni) and Titanium (Ti) are commonly chosen for their significant difference in potential and low absorption rates. This configuration is known as a multilayer neutron mirror, which can achieve a reflection angle considerably larger than the Fermi

pseudopotential of typical materials. Mirrors with monochromatic layers, where the period of each layer matches d, selectively reflect neutrons of specific wavelengths. By gradually varying the thickness of these layers, the wavelength range of neutrons meeting the Bragg condition can be adjusted, forming what is termed a supermirror[55]. Additionally, using materials sensitive to magnetic fields, such as Fe or Permalloy, allows for the creation of magnetic mirrors with spin selectivity. The wavelength-dependent reflectivity in monochromatic mirrors and supermirrors is shown in Figure 1.7. When the momentum transfer exceeds the critical angle for reflection, the reflectivity sharply declines following a q^{-4} pattern characteristic of quantum mechanics. In multilayer neutron mirrors, the achievable momentum transfer for reflection is several times greater than that of a single nickel layer, known for its high pseudopotential. The performance ratio of the multilayer neutron mirror is generally evaluated relative ratio to the momentum transfer at the critical angle of reflection for a nickel monolayer, which is $q_{\mathrm{Ni}} = 0.215$ nm^{-1}.

$$m = \frac{q_{\mathrm{m}}}{q_{\mathrm{Ni}}} \tag{1.70}$$

This ratio is called m-value, and the larger this m-value is, the more neutron reflection with large momentum transfer can be realized.
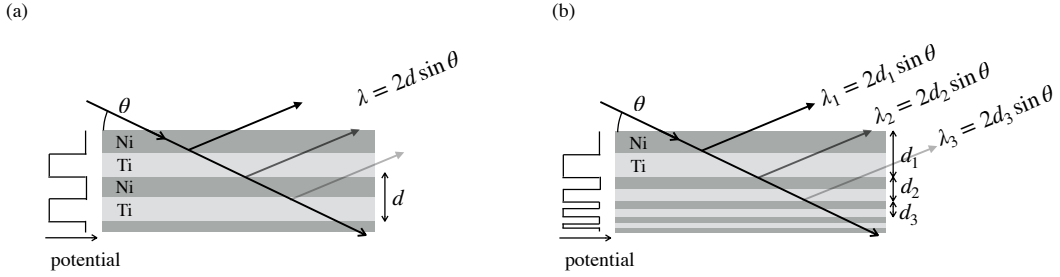
Figure 1.7: The reflection mechanism of (a) monochromatic multilayer and (b) supermirrors.

However, surface or interface roughness in a thin film can reduce the layer's reflectivity and alter the reflection curve. If there is an inter-diffusion or a density gradient of atoms at the interface, this diffusion zone is also considered as roughness. The compositional distribution at the interface is typically represented as a Gaussian distribution in terms of depth. The reflectivity $R(q)$ from a rough interface, where the compositional distribution at the interface has a standard deviation σ, is expressed as:

$$R(q) = R_{\mathrm{s}} \exp\left(-q^2 \sigma^2\right) \tag{1.71}$$

Here, R_{s} is the specular reflectance from an ideal interface without roughness. From these measurements, by analyzing the neutron reflectance at the material interface, we can gather information about the thickness and composition of each layer, as well as the roughness between layers. This technique is known as neutron reflectometry and is widely used in experiments involving physical properties.

In general physics experiments, neutron mirrors are extensively utilized as guides to direct neutrons from the source to the experimental setup, enhancing the statistical data available for the experiment. Monochrome mirrors, for instance, are employed to select long-wavelength monochromatic neutrons from white neutrons produced by a nuclear reactor. Supermirrors serve as guide tubes for white neutrons in pulsed neutron sources. Magnetic mirrors are used for polarizing neutrons. In these applications, the wavelength resolution, wavelength range, and reflectivity of the reflected neutrons

are crucial for experimental performance. Therefore, it is essential to design an ideal multilayer neutron mirror tailored to the specific requirements of each experiment.

Multilayer neutron mirrors are created by depositing thin films of materials like Ni and Ti onto glass substrates or other bases using sputtering or vapor deposition equipment. Common sputtering devices include ion beam or magnetron systems, which remove atoms from the target material and deposit them onto the substrate. There is ongoing research to achieve stable layering with a large number of layers. In Japan, groups at Kyoto University and JAEA have developed their own unique deposition technologies. For mirrors with high m-values, each layer's thickness is only a few nanometers, so imperfections at the interface are a primary cause of reduced reflectivity. Improvements in stacking techniques are expected to mitigate these imperfections, and research is actively being conducted to develop high-performance mirrors approaching an m-value of 10[56].

1.2.6 Facilities

Neutrons are generated through various physical processes such as nuclear fission, decay of nuclei, and spallation reactions. In space, they are produced by solar flares and space showers in the atmosphere, often being encountered. However, for experiments involving neutron optics, the available neutron energy is a minute fraction of what is generated through these natural processes. To efficiently create low-energy neutrons suitable for experiments employing neutron optics, specialized neutron experimental facilities exist. These facilities can be used as high-intensity neutron sources by efficiently generating using nuclear fission, nuclear fusion, and spallation reactions. Neutrons produced by these methods typically possess energies of several MeV. To obtain low-energy neutrons suitable for experiments, a cooling process is applied using heavy water or liquid hydrogen. The cooled neutrons then diffuse radially, and the energy follows the Boltzmann distribution. Because neutrons cannot be induced electromagnetically, shielding is generally used to shape the beam before pulling it into the experimental setup. The section involves a description of the neutron experimental facilities utilized for these purposes.

Reactor Neutron Source

Reactor neutron sources employ neutrons generated through nuclear fission for scientific experiments. On the NIST Center for Neutron Research (NCNR) at the National Institute of Standards and Technology (NIST) in Maryland, USA, neutron generation arises from the fission of ^{235}U. Control rods made of Cd and B, placed amidst the ^{235}U fuel rods, manage the quantity of produced neutrons, sustaining a critical state. The operational power is 20 MW. One method utilizes D_2O, H_2O, or graphite moderation to cool down to 315 K. This produces a wide-ranging neutron spectrum extending up to energies that conform to a Boltzmann distribution centered at 26 meV. The other, a moderator using liquid hydrogen at 20 K generates neutrons with an energy level of approximately 1.7 meV[57].

JRR3 in Tokai-mura, Ibaraki, serves as Japan's most powerful neutron source. It operates as a research reactor using uranium fission with a maximum power of 20 MW. The facility comprises 26 cores, beryllium reflectors, and control rods with six fuel components, alongside two moderators. One uses circulating light water to extract thermal neutrons, while the other employs liquid hydrogen for cold neutron production. A neutron guide path extends from the moderator to the experimental hall for conducting experiments[58].

Accelerator Neutron Source

In accelerator neutron sources, neutrons are generated through fusion or spallation reactions induced by irradiating target materials with accelerated charged particles. The energy of the charged particles needs to surpass the energy threshold required for the reaction, a value dictated by the target

material. For the ^{7}Li-p and ^{9}Be-p reactions, an energy of approximately 2 MeV is typically employed, especially in small neutron sources. Since small neutron sources allow neutron experiments to be conducted on a lab scale without fission, they are used for testing equipment to be installed in large experiments and for experiments that require continuous intermittent beam use[59, 60]. The spallation reaction serves as a high-intensity neutron source. In this reaction, charged particles accelerated to a few GeV interact with heavy metals containing a high number of neutrons in their nuclei. The neutron yield per accelerated charged particle is around 20. The number of neutrons produced by 1 kW of accelerated particle is about 2–3×10^{12} n/sec for nuclear reactions and low energy protons, about 3×10^{13} n/sec in a nuclear reactor, and about 2.6×10^{14} n/sec in a spallation neutron source, which means that spallation reaction has the highest efficiency. This type of neutron source has been in practical use for about 20 years now, with the development of large charged particle accelerators and the ability to deal with the problem of heat generated in the target. Globally, examples include LANSCE in the USA[61], CSNS in China[62], and the ESS, currently under construction in Sweden[63].

The Materials and Life Science Experimental Facility (MLF) at the Japan Proton Accelerator Research Complex (J-PARC), situated in Tokai-mura, Ibaraki, boasts access to the world's most intense neutron source[64, 65]. In this facility, protons accelerated to 3 GeV are directed into liquid mercury, initiating spallation reactions that yield neutrons. The maximum beam power is 1 MW, and the produced neutrons undergo cooling by moderators before being directed to various beamlines. There are three types of moderators: coupled, decoupled, and poison types using liquid hydrogen, each offering different wavelength resolutions and statistical characteristics. To ensure efficient neutron generation, the moderators and targets are covered with reflective material, excluding the beam ports. Protons are delivered in pulses with a width of about 100 ns at 25 Hz, resulting in pulsed neutron generation. As neutrons generated with various energies possess different velocities, the neutron wavelength can be determined based on the distance and time of flight (TOF).

1.2.7 Detectors

Since neutrons lack the ability to directly interact with and ionize matter, they are converted into charged particles before detection, where they manifest as electrical signals. Fast neutrons, lacking the ability to ionize matter, are measured using charged particles generated through elastic scattering with atomic nuclei. For slow neutrons, charged particles resulting from neutron-induced nuclear reactions are employed for measurement. The neutron detector is distinguished into two categories: time-integrating detectors, and time-differentiating detectors. Both types of detectors employ reactions that emit charged particles with a significant capture cross-section and suitable energy.

$$n + {}^{10}\text{B} \quad \rightarrow \quad {}^7\text{Li} + \alpha + 2.8 \text{ MeV (7\%)} \tag{1.72}$$

$$n + {}^{10}\text{B} \quad \rightarrow \quad {}^7\text{Li}^* + \alpha + 2.3 \text{ MeV} \rightarrow {}^7\text{Li} + \alpha + 0.48 \text{ MeV (93\%)} \tag{1.73}$$

$$n + {}^6\text{Li} \quad \rightarrow \quad \alpha + {}^3\text{He} + 4.79 \text{ MeV} \tag{1.74}$$

$$n + {}^3\text{He} \quad \rightarrow \quad {}^3\text{H} + p + 0.764 \text{ MeV} \tag{1.75}$$
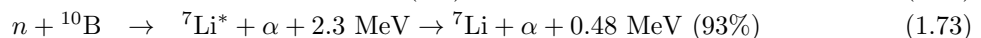
The absorption cross sections for each reaction depend on the neutron energy, these are 5330 barn for ^{3}He, 3840 barn for ^{10}B, and 940 barn for ^{6}Li at 25 meV for neutrons. The higher the energy of the emitted gamma rays, the greater the energy imparted to the reaction products. Using the wave height separation method allows for the effective removal of backgrounds such as gamma rays. The larger the absorption cross-section, the higher the detection efficiency. Excited atoms or ion pairs are generated as a result of collisions between charged particles in the detector material. The detection of neutrons can be categorized into three primary types based on the physical phenomena arising from their interaction with the material. The first type involves detection through ionization, the second through scintillation, which is a luminescent phenomenon, and the third through pyrophoresis (using imaging plates). Imaging plates, similar to scintillators, convert incident radiation into light but do

not emit fluorescence immediately; rather, they do so when stimulated with a laser[66]. Proportional counters filled with ^{3}He gas are relatively easy to make and handle, in addition to having high detection efficiency. However, they are not suitable for experiments that require high positional resolution due to the large detectable area. By using a micro-pixel chamber to detect charged particles generated by ^{3}He gas, a detector with high positional resolution can be used[67, 68]. ^{10}B converter-based detectors use gas electron multipliers to detect neutrons[69, 70]. Scintillator-based detectors can be used in combination with resistance-segmented photomultiplier tubes to provide position-resolved detectors[71]. Both position-resolving detectors rapidly process the electrical signals representing neutrons via application-specific integrated circuit (ASIC) chips and a field programmable gate array (FPGA), and so on, and store the signals as data.

1.3 Expansion of Neutron Optics

In modern physics, understanding gravity and strong interactions is essential for a unified explanation of physical phenomena. Advanced physics research requires exploring the fifth force, deepening our understanding of quantum mechanics, verifying nuclear forces precisely, and investigating fundamental symmetry breaking. Past experiments using neutron optics have provided important results for the development of fundamental physics. Currently, many experimental plans using neutron optics aim to further explore fundamental physics. The relevance of neutron optics in these studies is not only undiminished but is also receiving increasing attention in the scientific community.

Experiments in neutron optics exploring fundamental physics are achieved by reducing statistical and systematic uncertainties and by constructing smart experimental setups. The use of pulsed neutron sources has significantly improved statistical uncertainties. Additionally, the measurement of wavelength dependence using the neutron time-of-flight method has contributed to reducing systematic uncertainties. In neutron experiments where focusing using electromagnetic forces is not feasible, neutrons are utilized within experimental setups by shaping the beam using shielding. To avoid losing statistical quantities, it is necessary to draw a large-area neutron beam into the experimental apparatus. As the area of the neutron beam increases, the optical components used also inevitably become larger. Despite this, the required shape and installation precision of each component remain unchanged, necessitating the use of large, precise optical components. Developing such optical components is extremely challenging, and so far, neutron optics have often compromised shape accuracy to improve statistical quantities, a significant difference from X-ray optics, which can utilize focusing systems.

However, now that the statistical quantity issues have been addressed with the advent of pulsed neutron sources, achieving high precision in neutron optical components could lead to significant improvements in measurement accuracy. These circumstances suggest that the development of high-accuracy neutron optics can expand the exploration area of fundamental physics experiments. In the following sections, the development of neutron optics is divided into three directions.

1.3.1 Large Optical Components with Maintained Accuracy

Neutron optical components need to use a large-area neutron beam to maintain statistical quantities, as neutrons cannot be focused. In addition to shaping the beam using shielding, neutron transport can be facilitated by conduits using neutron mirrors. Neutron reflection occurs when neutrons are reflected at the interface due to the Fermi pseudopotential of the material. The critical angle of reflection θ_c is given by the following formula:

$$\theta_c = \sqrt{\frac{b_c N}{\pi}}\lambda, \tag{1.76}$$

where N represents the atomic density. The critical angle of neutron reflection can be expressed using the critical angle of nickel, which has a large potential, and the m-value as:

$$\theta_c = 0.0174 m\lambda \ [\text{rad}]. \tag{1.77}$$

From this, it is clear that the critical angle of reflection is inversely proportional to the wavelength of the neutron. If the mirror's surface is not an ideal plane, the incidence angle will vary depending on the shape accuracy. When the wavelength of reflected neutrons is fixed, and the mirror surface has a standard deviation σ of slope error, with the ideal reflection angle denoted as θ_0, the reflectivity of observed reflected neutrons can be written as:

$$R(\theta_0) = \int_\theta R(\theta) \frac{1}{\sqrt{2\pi\sigma^2}} \exp\left(\frac{\theta - \theta_0}{2\sigma^2}\right) d\theta \tag{1.78}$$

As this equation shows, the variation of reflectivity $R(\theta)$ with respect to θ requires the standard deviation of the mirror's slope error, σ, to be sufficiently small. If the reflectivity dependent on θ also follows a Gaussian distribution with a standard distribution of σ_R and assuming $\sigma = \sigma_R$, the reflectivity decreases by about 22%. The decrease in reflectivity depends on the momentum transfer distribution of reflectivity, but generally, slope error better than $1/10$ of the incidence angle is required. Typically, the energy of transported neutrons is 25 meV for thermal neutrons, and for an $m = 3$ mirror, the critical reflection angle is 9 mrad, demanding a slope error of 0.9 mrad.

On the other hand, experiments searching for the violation of time-reversal symmetry using polarized neutrons, as described in section 1.1.4, utilize epithermal neutrons near 1 eV. For epithermal neutrons with an energy of about 1 eV, the reflection angle is an order of magnitude smaller than that for thermal neutrons. Even using a supermirror with an m-value of 3, the reflection angle is only about 1.5 mrad. Therefore, a mirror reflecting epithermal neutrons requires a slope error of 0.15 mrad. Moreover, to reflect a neutron beam of approximately several centimeters square at a reflection angle of 1.5 mrad, a footprint of more than 6 meters is needed. Technically, installing a neutron mirror over 6 m long with a precision greater than 0.15 mrad is challenging. To address this issue, research is being conducted on multilayer neutron mirrors with a high m-value, but it is still in the development stage.

Non-specular reflection dependent on surface roughness, as described in Section 1.2.5, leads to a decrease in reflectivity due to its dependence on the momentum transfer of reflected neutrons. For a nickel monolayer film mirror reflecting neutrons at the critical angle, the momentum transfer is 0.215 nm^{-1}. If the mirror has a roughness of 1 nm, its reflectivity decreases by 5%. In contrast, for a neutron mirror with 1 nm of roughness reflecting 0.028 nm (1 eV) neutrons, the decrease in reflectivity is as much as 86%. To prevent this reduction in reflectivity, the mirror surface's roughness needs to be finely controlled, proportional to the square of the wavelength. To reduce the reflectivity loss of 1 eV epithermal neutrons to a similar degree as 0.25 eV thermal neutrons, the surface roughness must be below 0.025 nm. Thus, the required precision of the mirror increases with the square of the wavelength used, demanding higher accuracy in surface roughness and shape. Realizing reflective optical components for epithermal neutrons necessitates overcoming these precision challenges. Solutions to this challenge are discussed in section 2.2.1, with demonstration experiments presented in Chapter 3.

1.3.2 Component Shape Accuracy

The interactions observed between neutrons and matter depend on the distance of interaction. The physical quantities in various experiments are obtained by subtracting the interaction distance from the observed quantities, and hence, their accuracy is contingent on the precision with which this interaction distance is determined. For example, in experiments using crystal diffraction, the interaction distance corresponds to the crystal's thickness, necessitating precise determination of this

value. When neutrons are incident on a crystal under Bragg conditions, interference fringes reflecting the interactions within the crystal can be measured. The periodicity of these fringes allows for precise determination of the interactions acquired by neutrons inside the crystal. Neutrons diffracted in the crystal create interference fringes reflective of these internal interactions. The periodicity of these fringes can be written as:

$$\phi_{\mathrm{P}} = \frac{D}{\Delta_H} = \frac{v_H D \tan \theta_{\mathrm{B}}}{\pi H} \tag{1.79}$$

Here, D is the crystal thickness, θ is the incidence angle, and H is the reciprocal lattice vector of the crystal plane. The v_H denotes the crystal's averaged potential and can be expressed as:

$$v_H = \left(\frac{4\pi}{a^3} \sum e^{iQ \cdot x} \right) e^{-W} \left[b_{\mathrm{N}} + (Z - f_{\mathrm{e}}(Q)) \, b_{\mathrm{ne}} + b_5(Q) \right] \tag{1.80}$$

The initial sigma represents the crystal's periodic structure, W is the crystal temperature factor, b_{N} is the nuclear scattering length, f_{e} is the atomic form factor, b_{ne} is the neutron-electron scattering length, and b_5 denotes scattering due to the fifth force. As this formula indicates, the measurement of interference fringes due to dynamical diffraction can be used to search for the fifth force. However, the sensitivity of the search is limited by the precision of the physical quantities included in the other terms. In particular, the crystal's periodic structure and thickness are the most dominant factors of systematic uncertainty. Due to the difficulty in accurately determining these factors, the use of neutron dynamical diffraction in fundamental physics experiments has been limited since its demonstration in the 1970s. Precise measurement of the crystal thickness, which is geometrically determined, or experiments using a relative measurement system that can eliminate this factor, are therefore required.

The crystal thickness term is eliminated using a neutron interferometer measurement. The neutron interferometer can measure the forward scattering length by crystals. The obtained phase shift by the inserted sample using the crystal interferometer can be written as

$$\phi_{\mathrm{I}} = \langle b \rangle \lambda D = \frac{16}{a^2 \sqrt{3}} 4\pi v_0 D \sin \theta_{\mathrm{I}} \tag{1.81}$$

where the $\langle b \rangle$ is the scattering density, given by the product of the scattering length and the atomic density. The θ_{I} is the Bragg angle for neutron interferometer, whose value can determined with high presition by the same method of pendellösung measurements. The ratio of the phase shift obtained from pendellösung interferometry to that obtained from interferometry can be written as

$$\frac{\phi_{\mathrm{P}}}{\phi_{\mathrm{I}}} = \frac{2v_H \tan \theta_{\mathrm{PB}} H_{\mathrm{I}}}{v_0 \sin \theta_{\mathrm{BI}} H_{\mathrm{P}}} \tag{1.82}$$

where the θ_{PB} is the Bragg angle for pendellösung interference measurement, θ_{BI} is the Bragg angle for neutron interferometer, H_{P} is the reciprocal lattice vector for pendellösung interference measurement, and H_{I} is reciprocal lattice vector for neutron interferometer. The crystal thickness term is eliminated from the two measurements.

The interesting scattering length can be written from the ratio of the phase shifts obtained by the two measurements as

$$\frac{v_H D_{\mathrm{P}}}{v_0 D_{\mathrm{I}}} = e^{-W} \left(1 - (1 - f_{\mathrm{e}}(Q)) \frac{b_{\mathrm{ne}}}{b(0)} + \frac{b_5(Q) - b_5(0)}{b(0)} \right) \tag{1.83}$$

where the D_{P} is the crystal thickness for pendellösung measurement, D_{I} is the crystal thickness for interferometer measurement, whose values are assumed as same. The $b(0)$ is the literature value of forward scattering length, which generally refers to the nuclear scattering length, but since the fifth force term was not assumed in the previous experiment, the experimental value is written as the

forward scattering length. By using the atomic structure factor of literature values, the temperature factor and neutron-electric scattering length can be determined, and a fifth force can be explored. These values are determined from the momentum dependence of the averaged potential.

In the search for the fifth force, the dominant uncertainties in v_H are primarily determined by the atomic structure factor and the neutron-electron scattering length. The estimated accuracy in determining $v_H D$ from these uncertainties is around 10^{-5}. Given that the sensitivity of neutron interferometer phase shift measurements is about 0.02 rad, a phase rotation of approximately 2000 rad is required. This phase rotation depends on the thickness of the sample, necessitating a single-crystal sample with a thickness of about 5 mm to achieve the aforementioned phase. The thickness of the single-crystal sample used must be determined with the same level of accuracy as the determination of the averaged potential. Therefore, a thickness accuracy of about 0.25 µm is required. Since a typical single-crystal sample has a thickness error of several µm, it is necessary to improve the sample thickness accuracy by an order of magnitude to effectively search for fifth force. The solution to this challenge is discussed in Section 2.2.2, and the demonstration experiment is described in Chapter 4.

1.3.3 Component Installation Accuracy

High-precision optical components need to be installed in experimental apparatuses with accuracy equivalent to the precision of the components themselves. For example, in the case of neutron interferometers, each component must be installed within the accuracy specified by the coherent length. The interaction of neutrons can be measured by a neutron interferometer as a phase difference acquired by neutron waves separated into two paths. The interference fringes obtained by splitting and then recombining the neutron waves reflect the difference in interactions between the two paths. The conventional interferometers achieve neutron interference by controlling neutron waves through diffraction at lattice planes cut from silicon single-crystal ingots. However, the interactions measurable by a neutron interferometer are proportional to the interaction time, necessitating either longer wavelengths or larger scales. In interferometers using single-crystal ingots, achieving these conditions is structurally challenging, leading to a demand for interferometers operating on entirely different principles.

Neutron interferometers utilizing neutron mirrors offer an experimental system that can accommodate both long-wavelength neutrons and larger-scale setups. Although continuous development and research have been conducted, practical implementation has not been achieved due to the difficulty in positioning neutrons within their coherence length. The coherence length of neutrons, as described in Section 1.2.2, can be explained by the dispersion of neutron wavelengths. When considering a wave spread in three dimensions, its coherence length can be broken down as follows:

$$\sigma_k^{x,y,z} L_{x,y,z}^{\mathrm{c}} = \sqrt{2} \tag{1.84}$$

where the z-direction is considered the direction of wave propagation, with x and y directions representing the transverse coherence length, and the x-direction indicating the longitudinal coherence length. The σ_k represents wave vector dispersion and is dependent on the experimental setup. For general cold neutrons, the value of wave vector dispersion $\sigma_{\mathrm{k}} \simeq 0.4$ nm^{-1} leads to the coherence length of approximately 3 nm. To observe the interference of neutron waves, neutron optical components must be installed with the aforementioned precision. Solutions to this challenge are discussed in Section 2.2.3, and the demonstration experiments are described in Chapter 5.

1.4 Summary of Introduction

In modern physics, understanding gravity and strong interactions is crucial for a unified explanation of physical phenomena. Further progress in physics requires exploring fifth force, deepening the understanding of quantum mechanics, precisely verifying nuclear forces, and studying fundamental

symmetry breaking. Neutron optics, used in past fundamental physics experiments, has significantly contributed to the development of basic physics. Today, many experimental plans using neutron optics to explore fundamental physics are proposed, and the relevance of neutron optics continues to grow.

Neutron optics is described using the Born approximation, assuming that neutron wavelengths are sufficiently larger than nuclear potentials. As a result, neutron optics allows the use of optical phenomena like interference, reflection, and diffraction. These phenomena enable the measurement of various physical quantities, such as gravity, nuclear forces, and material structures. However, the accuracy of these measurements is determined by statistical and systematic uncertainties. While statistical uncertainties have dramatically improved with the use of pulsed neutron sources, uncertainties originating from optical components remain unresolved. This is due to the difficulty in focusing neutrons using electromagnetic forces, necessitating the use of large optical components and complicating the development of components meeting the required precision. To enhance the accuracy of physical measurements, this issue must be resolved.

The challenges associated with optical components can be categorized into three areas, as shown in Section 1.3: the development of enlarged optical components with maintained accuracy, the accuracy of component shape, and the precision in component installation. This paper aims to expand neutron optics by addressing these challenges of component accuracy. The advancement of neutron optics will not only improve the accuracy of measurements in neutron optics-based fundamental physics experiments but also expand the range of feasible experiments.

In the following chapters, Chapter 2 will outline the necessary developments to expand neutron optics. These developments will tackle the three identified challenges using advanced machining technologies. The solutions to these challenges will be demonstrated through experimental proof in Chapters 3, 4, and 5, showcasing the progress in neutron optics. Chapter 6 discusses the impact of expanded neutron optics on fundamental physics. Finally, Chapter 7 concludes this dissertation.

Part II

Methods

Chapter 2

Extension of Neutron Optics Using Advanced Machining Technology

Neutron optics serves as an effective tool for investigating fundamental physics, yet the scope of its exploration is nearing its potential limits. To surpass these constraints, enhancing the precision and broadening the region of phenomena manageable by neutron optics is essential. Addressing this challenge, I propose the utilization of advanced machining technology for the development of neutron optical components. This technology, which began with aspherical lens machining around 1980, marked a significant change in the manufacturing process. The traditional process, once reliant on spherical symmetry and loose abrasive grains, evolved into a cutting procedure employing a machining device with approximately 1 nm precision. This advancement enabled rapid and mass production of components demanding near-nanometer precision. This advancement encompasses a suite of ultra-precision mechanical component technologies, including guide systems, feed mechanisms, length measuring systems, and control systems for machining equipment. The development of shape-measuring devices to assess workpieces also supports this technology. Furthermore, to achieve high-precision machining and evaluation of workpieces without compromising reproducibility due to disturbances and other factors, advanced design technology is indispensable. This dissertation collectively refers to these design, machining, and evaluation methodologies as "Advanced Machining Technology".

Advanced machining technology has been increasingly applied in physics experiments, notably in X-ray focusing systems[72], sequentially timed all-optical mapping photography (STAMP)[73], near-infrared spectroscopy[74], and in measuring the roundness of silicon spheres for determining the Planck constant[75]. However, its application in neutron optics is relatively nascent, with limited uses such as in the development of neutron mirrors[76, 77, 78], suggesting significant untapped potential. By utilizing this technology for the development of neutron optical components, the accuracy of each aforementioned component can be enhanced. Developing these components in-house allows for flexible adjustment of the guaranteed accuracy to align with the experimental system, thus improving the efficiency of the development process. It also facilitates fine-tuning of the equipment before and after experiments, accelerating the development cycle. Improving the accuracy of each component will reduce the uncertainty in physics experiments, enabling the investigation of new areas in physics.

In the subsequent sections, Section 2.1 provides a detailed explanation of the advanced machining technology. Section 2.2 outlines a method to demonstrate that neutron optics can be developed utilizing this technology.

2.1 Advanced Machining Technology

The advent of aspherical lenses around 1980 marked the beginning of ultra-precision machining technology, a key component of advanced machining technologies. Since the 13th century, lens machining has relied on spherical symmetry and loose abrasive grains to achieve the desired precision. This process evolved with the introduction of diamond tool cutting, enabling the mass production of aspherical plastic lenses by creating molds. Today, ultra-precision machining equipment with a control resolution of 1 nm or less is a reality. It's employed in fabricating various consumer device components, such as hard disk media and polygon mirrors. The achievement of high control resolution has allowed the ductile mode machining of brittle materials like glass, silicon, and germanium, similar to how metallic materials are processed, by using extremely small depths of cut.

Ultra-precision machining technology operates by transferring the precise motion trajectory of the machining device to the workpiece using a single-crystal diamond tool. The development of these machining tools is supported by ultra-precision mechanical component technologies, including guidance systems, feed mechanisms, length measuring systems, and control devices. The performance of ultra-precision machined workpieces is assured by evaluating them with an accuracy equal to or greater than the machining accuracy. Since contact-based workpiece evaluation can lead to scratches and deformation, non-contact measurement methods using light or similar means are generally employed, allowing for evaluations with an accuracy of up to 0.1 nm. Workpieces and machining tools made of metal are not immune to temperature-induced deformation. For instance, 1 m of iron will deform by 12 µm with a temperature change of 1 K. Therefore, the temperature is controlled to about 0.0001 K to mitigate this effect.

In the following sections, the advanced machining technology equipment suite utilized in this study is introduced. This section can be skipped if not deemed necessary.

2.1.1 Ultra-High Precision Machining

When planning machining processes, it is crucial to consider in advance the specific type of machining required to achieve the target accuracy. The shape accuracy of the workpiece is determined by various factors, as outlined in the Table 2.1. This table details the factors contributing to accuracy reduction in relation to each aspect required for machining. While the precision of a workpiece is primarily influenced by the machining device's accuracy, it's essential to account for a multitude of factors. These include the machining method, the accuracy of workpiece installation, tool selection, and environmental considerations such as external disturbances. Therefore, all these aspects must be taken into account to ensure the desired accuracy in the machining of the workpiece.

Table 2.1: Machining Accuracy Relationship Table.

	Machine	Environments	Workpiece	Tools	Methods
Machining precision	◯				
Work stability	◯			◯	◯
Tool stability			◯	◯	◯
Temperature	◯	◯	◯	◯	◯
Roundness				◯	
Time dependence			◯		◯
Violation		◯			◯
Workpiece installation			◯	◯	

The high-precision aspheric and free-form surface grinders available at RIKEN are the ULG-100A (H3) and ULG-100D (5A) from Toshiba Machine Co. The appearance of the two machines is shown

in Figure 2.1, and the configuration of the available axes is shown in Figure 2.2. These machining centers are specialized ultra-precision machines, specifically engineered for high-precision turning and grinding of free-form surfaces. The primary distinction between the two machines lies in their machining accuracy, with the ULG-100D (5A) capable of achieving higher precision. The performance of ULG-100D (5A) is summarized in Table 2.2. This heightened accuracy in ultra-precision machines is determined by several critical factors.

- Accuracy of stage movements

- Accuracy of stage position measurements

- Accuracy of grinding tools

- External factors such as temperature and vibrations

These factors are briefly discussed below.

(a) ULG-100A(H3) (b) ULG-100D(5A)
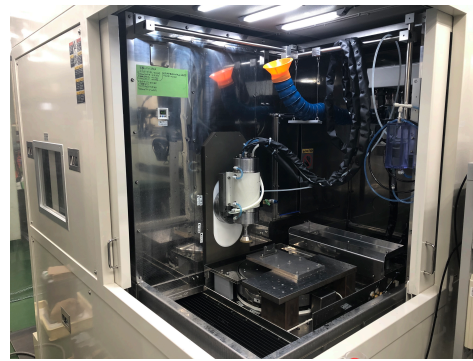
Figure 2.1: Image of the processing machine.
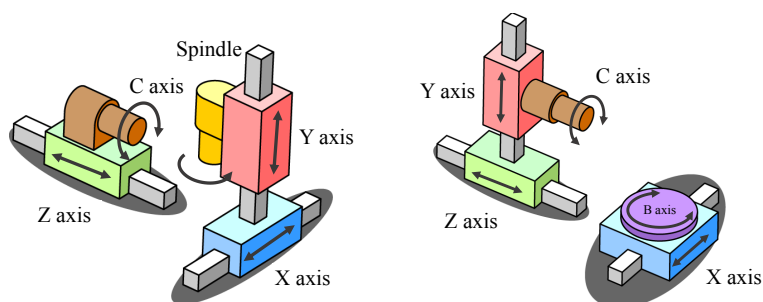
Figure 2.2: Axes configuration of the processing machine for (left) ULG-100A(H3) and (right) ULG-100D(5A).

Table 2.2: Performance table of ULG-100D(5A).

Axes	Resolusion	Minimum unit	Range	Velocity	Runout	Uncertainty
Linear axis (X)	0.1 nm	1 nm	450 mm	1000 mm/min	0.3 μm / 450 mm	±0.05 μm
Linear axis (Y)	0.1 nm	1 nm	150 mm	3000 mm/min	0.2 μm / 150 mm	±0.05 μm
Linear axis (Z)	0.1 nm	1 nm	300 mm	1000 mm/min	0.2 μm / 300 mm	±0.05 μm
Rotation axis (B)	0.00001 deg	0.00001 deg	-	< 300 rpm	0.2 μm	-
Rotation axis (C)	0.00001 deg	0.0001 deg	-	< 2000 rpm	0.05 μm	-
Spindle (ABC-20MP)	-	-	-	10000–60000 rpm	-	-

General-purpose machining centers typically employ a screw feed mechanism to move the stage. This method involves transmitting the rotational power of the screw to the stage, thereby allowing very precise positioning in a fixed direction, especially when bearings with high rigidity in the feed direction are used. However, this approach has its drawbacks, including backlash in the screw rotation. Additionally, vibration components in the drive direction and other disturbing forces, such as power-induced vibration and screw pitch errors, can adversely affect the stage, diminishing its movement accuracy. To address these issues, ultra-precision machines often utilize a linear motor drive. The operational principle of a linear motor drive is similar to that of a rotary motor, except that it operates along a linear axis. In this setup, a fixed magnet and an electromagnet are positioned between the stage and the guideway. The stage movement is facilitated by the attraction and repulsion between their magnetic poles. This movement method, being non-contact and not requiring a deceleration mechanism, allows for highly accurate stage movement due to its high coupling accuracy and non-contact nature.

In general machining centers, three primary types of guideways are utilized: sliding guideways, hydrostatic guideways, and rolling guideways. The rolling guideways system is frequently utilized in precision machining equipment due to its low motion error resulting from friction. This makes it a preferred choice for applications requiring high accuracy. However, it's important to note that this system is not without its challenges. It does not have a mechanism to prevent errors caused by deformation due to dimensional differences in the rolling components. Additionally, vibrations caused by the elastic deformation of the rolling components as they pass through can also introduce errors, impacting the overall precision of the machining process. Ultra-precision milling machines address the aforementioned issues by employing V-V rolling guides. The V-V rolling guideway mitigates dimensional errors through the use of two V-shaped guides to steer the stage. This configuration enhances the accuracy of stage movement, enabling it to follow commands with a precision of approximately 1 nm. This motion of accuracy is particularly crucial in applications where ultra-precision is essential, ensuring that the machining process meets the stringent requirements for precision and reliability.

In ultra-precision machines, the accuracy of stage position measurement is of utmost importance. To achieve this high level of precision, a lattice interference encoder utilizing a hologram scale is employed. This encoder works on the principle that when a laser is incident on a hologram with a periodic structure, the resulting intensity pattern is a sinusoidal wave that mirrors the period of the hologram. For instance, if the hologram has a period of 250 nm and the sine wave generated by the hologram's interaction with the laser is divided into 250 analog-to-digital (AD) conversion divisions, the position can be identified with a resolution of 1 nm[79]. This high-resolution measurement capability is essential for precisely determining the position of each stage in ultra-precision machines, ensuring accurate and reliable machining operations.

External factors such as temperature and vibration are critical considerations in the operation of this machine. To mitigate these, the lubricating oil supplied to the machine's moving surfaces is temperature-controlled and continuously circulated to maintain a uniform temperature throughout the machine. Machining is standardized at 23°C to ensure consistency.

Vibrations affecting the machine are categorized into three types: internal vibrations from machine components and operator movement, external vibrations from ground movements caused by nearby railroads or construction sites, and natural external forces from earthquakes or wind. To address these, the machine is installed on an active vibration isolation device, which primarily counters vibrations from the ground. For vibrations not eliminated by this isolation device, an internal vibration suppression mechanism, known as a torque command filter, is used. Additional measures are also important, such as distancing workers from the machine during operations, installing the machine away from direct sunlight, conducting machining at night when external vibrations are minimal, and minimizing machining duration to reduce temperature variation effects. Neglecting these factors can significantly impact machining accuracy, preventing the machine from reaching its full potential. Therefore, careful management of temperature and vibration is essential for optimal machine performance.

2.1.2   Quantitative Evaluation Method for Component Accuracy

The created components are quantitatively evaluated using measurement devices appropriate for the desired information. Here, I define a coefficient to assess the accuracy of the component. For simplicity, let's consider a two-dimensional component with an imperfect shape as illustrated in Figure 2.3. The macro shape of the component is represented by function $F(x)$. Flatness refers to the deviation of a planar object from a geometrically perfect plane (geometric plane). It can be expressed using the difference between the ideal function and the actual function, as follows:

$$\text{flatness [m]} = [(F(x) - F_{\mathrm{i}}(x))]_{\text{Max}} \tag{2.1}$$

This value is widely used in the manufacturing industry to ensure the accuracy of a workpiece's shape. However, flatness cannot represent periodic shape features and does not incorporate the area of the component in its evaluation. As a result, the flatness of an component tends to return better values for smaller measurement areas, making it unsuitable for quantitative assessments. This kind of evaluation index is not appropriate for neutron optics, which uses reflective optical systems. Therefore, for assessing neutron optics component, the slope error, derived by differentiating flatness with respect to position, is more suitable. Slope error is defined as follows:

$$\text{slope error [rad]} = \left[\frac{d}{dx} \left(F(x) - F_{\mathrm{i}}(x) \right) \right]_{\text{Max}} \tag{2.2}$$

This quantity represents the angular deviation of the component's shape from its ideal plane, and can be used to define the reflection angle in reflective optical systems. It's important to note that slope error may yield meaningless values at certain points, such as the edges of the component, so its application is limited to effective ranges. The parallelism between two planes, A and B, can also be defined similarly using slope error.

$$\text{parallelism [rad]} = \left[\frac{d}{dx} \left(F_{\mathrm{i}}^{\mathrm{A}}(x) - F_{\mathrm{i}}^{\mathrm{B}}(x) \right) \right]_{\text{Max}} \tag{2.3}$$

The assessment of slope error and parallelism is conducted for components with sizes of several millimeters or larger. While macroscopic shapes are evaluated for their slope error, microscopic shapes are assessed based on roughness. The maximum height roughness within the measurement range is represented by Rz, as shown on the right side of the Figure 2.3. The average roughness is calculated using the difference between the highest peak and the lowest valley within a reference length, as follows:

$$\text{roughness [m]} = \frac{1}{L} \int_{\mathrm{L}} |f(x) - f_{\mathrm{i}}(x)| \, dx \tag{2.4}$$

where L is the effective length indicating the measurement range. The roughness evaluation can identify fine scratches caused by cutting marks during machining or dust particles. The effective length is generally defined on a scale of mm or less. The component used for neutron optics are evaluated by their slope error, parallelism, and roughness.

2.1.3   Evaluation Instruments

The accuracy of manufactured workpieces is assessed using measuring devices with a higher resolution than the machining process itself. These evaluation devices are crucial for assessing the installation accuracy of workpieces and tools during machining, as well as for evaluating components during experiments. Two distinct types of geometry and installation accuracy evaluation devices are described below, each with its unique features: contact type and non-contact type.
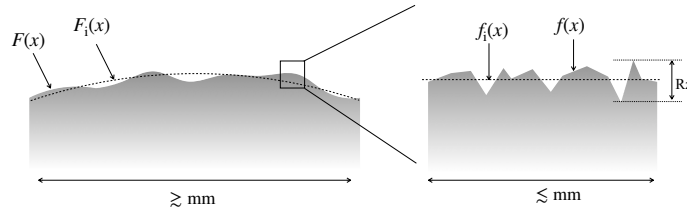
Figure 2.3: Macroscopic and microscopic shape evaluation methods.

1D Contact Sensors

The MU-CHECKER from Mitutoyo Corp. was utilized for measurement purposes. This device features a measurement range of ± 0.5 mm. The expected measurement accuracy is approximately 1 µm. As the measurement target is defined by the contact area of the probe, this allows for the measurement of macroscopic displacements.

Ultra-high accuracy CNC coordinate measuring machine

The Legex 707 (3DFD) from Mitutoyo Corp. was used for shape measurements. The measurement is conducted by bringing the contact point, made of a red ruby at the tip of the measuring instrument, into contact with the object being measured. This instrument is specifically designed for high rigidity, superior damping, and precise motion. It is also calibrated to accommodate vibrations and temperature changes. This calibration is crucial for its ability to comprehensively analyze and eliminate potential error factors, ensuring accurate and reliable measurements. As a result of this design and calibration, the device can perform shape measurements with an accuracy of $0.28 + L/1000$ µm, where L represents the length of the object being measured. This formula indicates that the measurement accuracy is dependent on the size of the object, ensuring precise measurements across a range of object sizes.

Non-contact 3D shape measuring machine

The PFU-3 from Mitaka Kohki Co. was utilized for shape and roughness measurements. This device features a laser with a wavelength of 635 nm, and it boasts a measurement accuracy of ± 0.5 µm. This instrument is capable of measuring both the microscopic and macroscopic shapes of an object by moving the stage that carries the object. This functionality allows for a comprehensive evaluation of the object's dimensions and shape across different scales.

Write laser interferometer

The NewView 7200 from Zygo Corp. was employed for roughness measurements. This instrument utilizes white light interferometry to acquire interference fringes based on the varying distance to the reflective surface of the measurement target in response to incident white light. The shape of the object is determined by these interference fringes. The vertical distance is calculated using frequency domain analysis, a proprietary interference peak detection method developed by Zygo. Owing to this advanced methodology, this instrument achieves extremely high measurement accuracy. It is capable of resolving details to less than 0.1 nm in the vertical direction within a measurement range of 0.4×0.3 mm. This level of precision makes it highly suitable for applications requiring ultra-fine measurement resolutions.

HeNe laser interferometer

The flatness and slope error measurements were conducted using the Verifire from Zygo Corp. This instrument operates on the Fizeau interferometric principle and employs a HeNe laser at 633 nm. The instrument is capable of emitting a laser beam with diameters of 102–152 mm, and it boasts a high measurement accuracy of less than 0.06 nm within that range[80]. This capability allows for the measurement of an object's shape within the laser-irradiated area in a single measurement session. This approach effectively eliminates the movement errors that can occur when repositioning the object, thereby enhancing the reliability and precision of the measurements. This single-measurement capability is particularly beneficial for assessing large or complex surfaces where maintaining consistent positioning can be challenging.

Autocollimator

The autocollimator was employed for parallelism measurements between two measurement objects. In this process, a laser emitted from a point source is collimated through a lens. The parallelism of the measurement object is then assessed by detecting the position of the laser reflected off the object. Generally, an autocollimator is capable of measuring relative changes in the yaw and roll directions of the measurement target. When two measurement targets are simultaneously illuminated, the reflected laser is detected at two distinct positions, varying based on the parallelism of these targets. The accuracy of parallelism measurement with an autocollimator depends on several factors: the precision of the lens curvature, the size of the laser collimation, and the positional resolution of the detector. Typically, the resolution of this method is about 5 µrad. This level of precision makes autocollimators a valuable tool for precise alignment and angle measurements in various applications.

2.2   Approach Method

To explore fundamental physics, the development of neutron optics is essential. The advancement of neutron optics can be achieved by enhancing the precision of each component and expanding the range of phenomena that can be handled. Neutron optics components require precision at the micrometer to nanometer scale, necessitating improvements in the development accuracy of these components. In neutron optics, which traditionally uses large components, the focus has often been on improving the statistical quantity of neutrons rather than addressing uncertainties due to the shape accuracy of components. Additionally, the variation in components used across different experimental systems has led to a lack of widespread development in neutron optics. In this context, neutron optics can advance by utilizing advanced machining technologies, including general technologies, for the development of components. The advancement of neutron optics can be approached in three ways: "improvement of large optical components with maintained accuracy", "improvement of component shape accuracy", and "improvement of component installation accuracy". The following sections will explain how these three methods contribute to the advancement of neutron optics. Experiments that demonstrate the advancement of neutron optics using these three methods are presented in the subsequent Part III.

2.2.1   Improvement of Large Optical Components with Maintained Accuracy

In neutron reflection optics, the required accuracy of surface roughness increases in proportion to the square of the wavelength of the neutrons used, and the required accuracy of shape increases in proportion to the wavelength, as explained in Section 1.3.1. To achieve epithermal neutron reflection, development of a mirror with 0.15 mrad slope error, a 6 m footprint, and 0.025 nm surface roughness is required. When compared to typical mirrors with several mrad of slope error, a footprint of about

100 mm, and surface roughness of approximately 0.1 nm, developing an epithermal neutron reflection mirror seems unrealistic. Considering a more practical system, if we assume the use of a multilayer mirror with an $m = 6$ and an incident neutron width of 1 mm, the critical reflection angle for 1 eV neutrons becomes 3 mrad. In this case, the required flatness of the mirror is 0.3 mrad. Even with the typical mirror surface roughness of 0.1 nm, this would only result in a 2% reflectivity loss. Such a mirror can be fabricated by combining conventional machinery with a glass substrate. The shape accuracy of the mirror produced can be quantitatively assessed using the array of measurement instruments employed in advanced machining technologies, as described in Section 2.1.3. Experiments reflecting epithermal neutrons using this large planar mirror are discussed in Chapter 3.

2.2.2 Improvement of Component Shape Accuracy

The interactions observed between neutrons and matter depend on the interaction distance. In various experiments, physical quantities are obtained by subtracting the interaction distance from the observed measurements. Therefore, the accuracy of these measurements depends on the precision with which the interaction distance is determined. In experiments using crystal diffraction, the interaction distance corresponds to the crystal's thickness, necessitating precise determination of this value. In experiments searching for the fifth force using neutron dynamical diffraction, the accuracy of the single-crystal sample's thickness becomes the most dominant source of systematic error, posing a significant challenge. The absolute value of the sample thickness can be eliminated by the combined measurement of coherent scattering length and forward scattering length, using dynamical diffraction and neutron interferometer respectively. It is important to note that the sample thickness needs to be the same value in both experiments. The required parallelism accuracy for the sample in this context is less than 1 μm. This level of precision can be achieved by employing ultra-precision machining with a grinding method on single-crystal samples. Conducting experiments with samples processed in this way enables the search for the fifth force. This research is explained in Chapter 4.

2.2.3 Improvement of Component Installation Accuracy

Neutron interferometer is achieved by controlling neutron waves with precision at the nanometer scale. Neutron interferometers, which are composed of recombining neutron waves that have been split into two paths, are widely used as devices to precisely measure neutron interactions. Existing neutron interferometers control neutron waves with accuracy within the coherence length using diffraction in silicon single crystals. However, to improve measurement sensitivity, the development of neutron interferometers using methods other than crystal diffraction is sought, as sensitivity enhancement is achieved through enlargement or the use of longer wavelengths. Interferometers using neutron mirrors can resolve these issues and enable high-sensitivity measurements, thus allowing for precise exploration of fifth force. The installation precision of neutron mirrors is determined by the coherence length, which is approximately 30 nm. To install each component with this level of precision, etalon substrates, widely used in laser optics, can be employed. The installation precision of each mirror can be achieved with micro-radian accuracy using autocollimators. These techniques were utilized to install optical components and verify whether they can improve installation accuracy and measure neutron interference. This research is described in Chapter 5.

Part III

Demonstration

In this part, we fulfill the requirements discussed in chapter 1 for large optical components with maintained accuracy, component shape accuracy, and component installation accuracy using the advanced machining technologies outlined in chapter 2, and conduct demonstration experiments.

In neutron reflection optics, as explained in Section 1.3.3 the precision required for mirrors increases with the square of the wavelength of the neutrons used, necessitating higher surface roughness precision and greater shape accuracy proportional to the wavelength. To realize epithermal neutron reflection in a practical system, if we assume the use of a multilayer mirror with $m = 6$ and an incident neutron width of 1 mm, the critical reflection angle for 1 eV neutrons becomes 3 mrad. At this point, the required slope error for the mirror is 0.3 mrad, which is described in Section 2.2.1. Even with the typical mirror surface roughness of 0.1 nm, this would only result in a 2% reflectivity loss. Such mirrors can be fabricated by combining conventional machinery with a glass substrate. The shape accuracy of the mirrors produced can be quantitatively assessed using the array of measurement instruments employed in advanced machining technologies, as described in Section 2.1.3. A neutron mirror meeting these conditions was developed, and experiments measuring the reflection of epithermal neutrons were carried out. These demonstration experiments are explained in Chapter 3.

In neutron optics, the interactions observed between neutrons and matter depend on the interaction distance. In experiments searching for the fifth force using neutron dynamical diffraction, the accuracy of the single-crystal sample's thickness becomes the most dominant source of systematic error, posing a significant challenge. The absolute value of the sample thickness can be eliminated by the combined measurement of coherent scattering length and forward scattering length, using dynamical diffraction and neutron interferometer respectively. It is important to note that the sample thickness needs to be the same value in both experiments. To carry out this requirement, the precision of parallelism required for the sample is less than 1 µm. To achieve this, ultra-precision machining with a grinding method was applied to single-crystal samples. Previous research has demonstrated that combining experiments using ultra-precisely machined silicon single crystals with neutron interferometers can increase the range of search for fifth force by up to two orders of magnitude. Adding experiments using ultra-precisely machined germanium single crystals can further enhance the sensitivity of these searches. This research is discussed in Chapter 4.

In Chapter 5, I discuss the practical application of neutron interferometers using multilayer mirrors, achieved by improving the installation accuracy of components. Neutron interference is accomplished by controlling neutron waves with precision at the nanometer scale. Neutron interferometers, constructed by recombining neutron waves that have been separated into two paths, are widely used for precise measurements of neutron interactions. Existing neutron interferometers control neutron waves within the coherence length using diffraction in silicon single crystals. However, to enhance measurement sensitivity, larger-scale or longer-wavelength approaches are required, leading to the demand for the development of neutron interferometers using methods other than crystal diffraction. I focused on neutron interferometers, which use neutron mirrors to control neutron wave motion. By using each mirror as an optical substrate used for laser optics and a laser surveying system, I developed an interferometer that met the required accuracy. By measuring the neutron nuclear scattering length using the developed interferometer, we confirmed that the interferometer functions properly. The development of this interferometer has made it possible to improve the accuracy of the measurement of neutron interactions and opened up the possibility of various physics experiments.

Chapter 3

Demonstration of Large Optical Components with Maintained Accuracy: Epithermal Neutron Reflection

The successful operation of spallation neutron sources, driven by intense proton beams, has enabled energy-resolved intense neutrons in the thermal and cold regions and also in the epithermal regions[81, 62, 64, 65]. In this description, we refer to neutrons with kinetic energy E_n in the region of 0.5–1 eV as "near-epithermal" neutrons. The energy resolution of the pulsed near-epithermal neutron beam facilitates efficient observations of neutron scattering with a large energy transfer in materials and precise studies of neutron-induced compound nuclear states for symmetry breaking at fundamental levels[31, 32, 33].

The use of transport optics for near-epithermal neutrons can significantly improve the efficiency of neutron applications in fundamental and practical experiments. A specular neutron reflector on the surface and interface of materials is the most commonly utilized optical device, which transports grazing-angle incident neutrons[82]. The transport systems using magnetic potentials have also been developed, however, their use is limited due to the requirement of huge magnetic fields and long effective lengths[83]. In transport using optical potentials, neutrons are reflected by the Fermi pseudopotential of the interfacial material[84]. The neutron supermirror is one of the most widely used in recent neutron facilities, which m-value is within the range of 2–3[85, 86, 87, 88, 89, 90]. Neutron mirrors are also employed in focusing systems, polarizers, and monochromators, underscoring their indispensable role in various scientific experiments. In contrast, the transport device for near-epithermal neutrons is still in the development stage. Because the near-epithermal neutron transport requires the m-value of approximately 10 or greater. In addition, the shape of the mirror requires 10 times more precision than that of conventional mirrors. For these reasons, specular reflection of near-epithermal neutrons has not been observed.

In this chapter, I approached the optical reflection measurement of near-epithermal neutrons as a first step toward realizing epithermal neutron optics. To reflect epithermal neutrons, I fabricated a multilayer mirror with a length of 300 mm and slope error of 0.3 mrad with $m = 6$. For the reflection measurements, I created a low-divergence beam using crystal diffraction from the silicon wafer and employed a neutron detector with high spatial resolution. By grazing incident epithermal neutrons on this mirror and measuring their optical reflection, I demonstrated that large optical components with

maintained accuracy could advance neutron optics.

3.1 Specular Reflection of Near-epithermal Neutrons

Neutrons are reflected at the interface by the Fermi pseudopotential of the material. The critical grazing angle of the reflection θ_c is given as

$$\theta_c = \sqrt{\frac{b_c N}{\pi}}\lambda,$$ (3.1)

where N represents the atomic density. In the case of Ni, which is widely used as a neutron reflector and has a large potential, its reflection angle can be written using neutron wavelengths as follows

$$\frac{\theta_c}{\lambda} = 0.0174 \text{ [rad/nm]}.$$ (3.2)

Generally, the energy of the neutron transported is 25 meV, which is a thermal neutron, so its reflection angle is 5 mrad. On the other hand, near-thermal neutrons with an energy of 500 meV have a reflection angle of 0.7 mrad, one order of magnitude smaller than thermal neutrons. Even if a supermirror with $m = 2$–3 is used, its reflection angle is about 2 mrad, which is insufficient to control neutrons with a beam area of several cm. From this, the reflections of high-energy neutrons with small reflection angles are not suitable for transport guides. Nonetheless, the recent introduction of pulsed neutron sources necessitates the development of robust control systems for epithermal neutrons. Neutron mirrors in conduit systems represent a well-established neutron control technology with a substantial reservoir of knowledge. Moreover, their adaptability to applications involving monochromators, focusing optics, and polarization components is readily attainable. I have contemplated expanding the scope of neutron mirror applications to encompass near-epithermal neutrons.

Reflective optics for epithermal neutrons are unsuitable for practical application due to their limited reflection angles, and no proof of principle experiments have been conducted to date. In the initial stages, it is imperative to ascertain whether epithermal neutrons can indeed undergo optical reflection. As previously discussed in Chapter 1, neutron reflection relies on the Fermi pseudopotential of matter. This pseudopotential assumes validity when the density of scatterers in the material is significantly lower than the neutron wavelength. The precision of this approximation approaches a practical limit as the neutron wavelength decreases. The experimental exploration of this adaptive limit is a crucial step that remains to be undertaken for neutron reflection, and it is essential to provide empirical validation in this context.

3.2 Accuracy Requirements for Mirrors

In order to achieve the reflection of epithermal neutrons with small reflection angles, the following specific developments are needed.

- Expansion of reflection critical angle

- Low divergence beam generation

- Quantitative observation of microscopic neutron orbital changes

- Improvement of smoothness in the mirror

Expanding the critical reflection angle enables alterations in neutron orbits that are detectable with practical neutron detectors. The application of supermirrors is a means to achieve this expansion. While most widely used supermirrors feature m-values of 2 or 3, some employ $m = 6$ mirrors[91], and development on $m = 10$ mirrors is underway[92, 93]. To discern slight modifications in neutron orbit resulting from the small reflection angle and the incident neutron orbit, generating a low-divergence beam is essential. The assessment of such subtle changes in neutron orbit necessitates the utilization of neutron detectors with high position resolution. The quality of neutron mirrors influences the occurrence of off-specular reflections[94]. Consequently, the development of mirrors meeting these requirements is of utmost importance.

3.3 Mirror Fabrication

I utilized an $m = 6$ monochromatic mirror to achieve a large reflection angle. This mirror was produced using an ion beam sputtering system located at Kyoto University. This mirror consists of NiC/Ti layers with a total of effectively 1600 layers; the thickness of each layer is 5 nm. Individual layers exhibit a full-width variation of $\delta d/d = 8\%$, which serves to diminish the reduction in reflectance due to slight misalignments in the angle of incidence. The reflection angle for a 0.5 eV neutron reflected using an $m = 6$ mirror is 4.2 mrad.

The mirrors were sputtered onto a glass substrate of $300 \times 70 \times 1.1$mm. The flatness of the glass substrate formed by the amorphous layer is generally about 0.2 nm, so the sputtered layer can be deposited stably. On the other hand, the substrate undergoes significant deformation due to layer stress, and the flatness is approximately $\gtrsim 10$ mrad. This slope error is larger than the reflection angle of a neutron with an energy of 0.5 eV, which means that the neutron reflection angle has a relative error of 100%.

To solve this problem, the glass substrate on which the mirrors were deposited was bonded to an aluminum substrate with good shape accuracy. The aluminum substrate was machined by a general-purpose machine tool, and its slope error was measured. Since the surface roughness of the machined aluminum substrate was less than that measured by laser interferometry, the contact-type shape measuring device was used to measure the surface. The results of the shape measurement of the aluminum jig are shown in Figure 3.1. The slope error of the substrate is approximately 0.02 mrad, which is about two orders of magnitude more accurate than the reflection angle of epithermal neutrons. The mirrors were bonded to the aluminum substrate using wax that melts at about $60°$C. The wax was applied to the aluminum substrate heated on a hot plate and cooled by placing a weight on the mirror to be glued. Annealing of the wax in an oven was also performed but to no avail. The slope error of the glued mirrors was measured using a laser interferometer and the results are shown in Figure 3.2. The slope error of the bonded mirror was 0.3 mrad, which was one order of magnitude smaller than the reflection angle of the 0.5 eV neutrons, and was approximately two orders of magnitude smaller than typical neutron mirrors sputtered onto glass substrates.

The mirror, glued to an aluminum jig, was fixed to the moving stage by means of a three-point support. The mirror stage was made using a micrometer and a hinge mechanism to fix and control the mirror with the necessary precision. This enabled the alignment of the neutron incidence angle and roll direction.

3.4 Specular Reflection for Cold Neutrons

To compare the reflectivity between near-epithermal and cold neutrons, we measured the cold neutron reflectivity of the mirror in advance at BL10. The experiment setup is shown in Figure 3.3. For a beam traveling along the z-axis, a mirror is placed on the yz-plane and the neutron is varied by
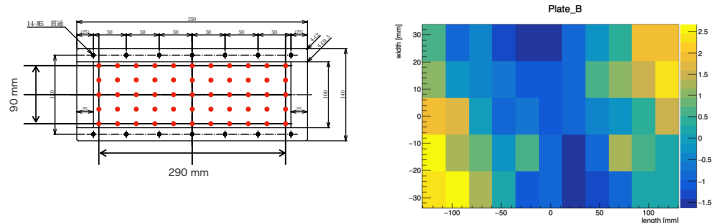
Figure 3.1: The measured shape of aluminum substrates. The left figure shows the measured point, and the right figure shows the measured

a small angle in the x-direction. The reflections by the mirror were measured by a neutron detector capable of time and 2D position detection[69, 70]. The x distribution of the direct neutron and reflected neutrons are shown in Figure. 3.5. The red distribution represents the direct beam, and the blue distribution represents the reflected beam. The direct neutrons were detected around $x = 53$ mm, and the reflected neutrons were detected around $x = 43$ mm. The reflection angle is based on the position of the two peaks and the distance from the mirror to the detector. The positional shift between direct and reflected neutrons was 9.56 mm, which positions of each distribution were obtained from the fitting with a Gaussian function. Since the distance between the mirror and the detector was 768 mm, the obtained reflection angle was 6.22 mrad.

The wavelength dependence of reflectivity is determined from the TOF spectra of the detected neutrons. The TOF spectra of each measurement are shown in Figure 3.5, which reflected neutron was obtained from the region of the red line in Figure 3.4. The reflectivity of the mirror can be determined by calculating the division of the direct beam spectrum by the reflected spectrum. The TOF dependence of the obtained reflectivity is shown in Figure 3.6, where the reflectivity in the total reflection region ($q < 0.13$ nm^{-1}) is normalized to be 1. The reason for this is that not all neutrons hit the mirror, which is evident in Figure 3.4. The momentum transfer is obtained from the wavelength and reflection angle. The wavelength was determined using the TOF method, with the distance between the neutron source and the detector being represented as 14.768 m. The reflectivity in the region of $q < 0.13$ nm^{-1} was due to the total reflection by the Fermi pseudopotential of NiC/Ti. This peak represents the reflection arising from Bragg diffraction of the multilayer, exhibiting a reflectivity of 35%. The multilayer structure was purposely designed to possess a broadened peak width, whose standard deviation was measured to be ± 0.09 nm^{-1}. This broadening relaxes the angular tolerance required for aligning a monochromatic multilayer mirror to reflect a monochromatic beam, a task that is otherwise difficult.

3.5 Configuration of Reflectivity Measurements of Near-epithermal Neutrons

For the epithermal neutron reflection measurements, neutrons diffracted by the Si wafer were used as the induction beam to the mirror in order to produce a low-divergence beam. The experimental setup in BL10 is shown in Figure 3.7.

The neutron beams were collimated to 20×80 mm by a pair of slits (slit 1 and slit 2) made of 5 mm thick B$_4$C[95]. The frame overlap was eliminated by the mechanical chopper located 7.2 m away from the moderator[96]. The collimated neutrons were directed in different directions from the beam axis
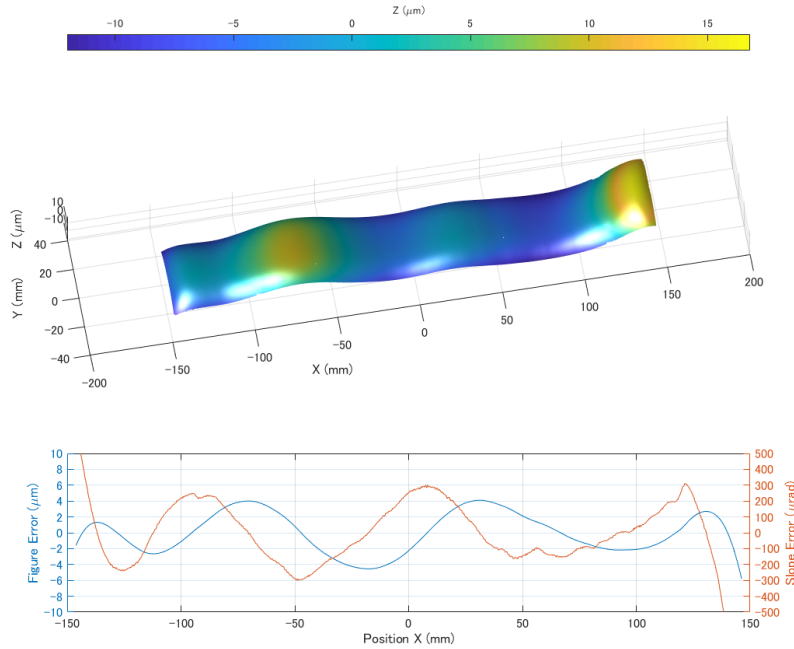
Figure 3.2: Flatness of mirror substrate bonded on the aluminum substrate.

by Bragg diffraction on silicon wafers. The diffracted neutrons were incident to the mirror through slit 3, which was a 50 mm-thick sintered B_4C blocks with the aperture of 1.13 mm wide. The holder of slit 3 was covered with a rubber sheet containing ^{10}B to absorb scattered neutrons and to define the diffracted neutron beam by 67 mm in the y-direction. The mirrors on the custom-made stage can be aligned in both the θ and roll directions. The alignment in the roll direction was accomplished with the laser. The diffracted and reflected neutrons were detected by a micro-pixel ^{3}He-containing chamber (μ-PIC)-based neutron detector capable of recording the arrival time and 2D position with a spatial resolution of 350 µm[67, 68]. The neutron detector was positioned 665 mm away from the center of mirrors to detect changes in trajectory resulting from neutron reflections accurately. The neutron path length between the moderator and detector was 14.93 m. The neutron wavelength in the pulsed neutron source was determined from the TOF and the distance from the moderator to the detector.

3.6 Diffraction by the Silicon Wafer

The diffracted neutron by the silicon wafers was used as the incident neutrons to the mirror, which can reduce the background of fast neutrons and flash gamma from the neutron source. The stack of 17 wafers of 5-inch diameter and 0.625 mm thickness was used instead of single bulk silicon so that the decrease of the intensity of diffracted neutrons is suppressed by the small misalignment among wafers. The measured TOF spectrum of neutrons diffracted by the silicon wafers is shown in Figure 3.8. The diffracted neutrons were observed only at specific wavelengths that satisfied the Bragg condition. By fitting each peak with a Gaussian function, the TOF observed diffracted neutrons were determined.
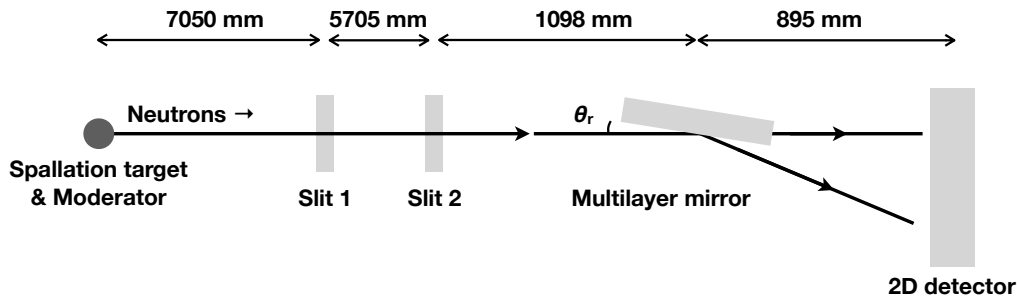
Figure 3.3: Diagram of the experimental configuration of reflectivity measurement using cold neutrons.

The observed neutrons around 12 ms were due to diffraction by (111) of the Miller index, and higher-order diffraction can be confirmed at an earlier TOF region. The observed tof for each diffracted neutron, normalized by the diffraction order, is shown in Figure 3.9. The normalized TOF depending on the diffraction order deviates from the fast direction by about 0.3%. This is presumably due to the shift of the TOF origin, but since wavelength resolution is not important in this study, we ignore it. The diffraction angle of a silicon wafer was obtained using (111) plane diffraction and the neutron wavelength from TOF. The diffraction angle was $\theta_B = 29.5$ deg, which was obtained by Bragg's law as $2a/\sqrt{3}\sin\theta_B = n\lambda$, where the λ is neutron wavelength, $a = 0.5431$ nm[97] is the lattice constant, and n is the diffraction order.

The divergence of diffracted neutrons was determined from the spatial distribution. The standard deviation of the diffracted neutron by (111) plane is 1.5585 ± 0.0008 mm, which was obtained by the fitting for Figure 3.10. The beam divergence was $\theta_{\mathrm{div}} = (\sigma_{\mathrm{FWHM}} - w)/L = 2.761 \pm 0.001$ mrad, where the $w = 1.13$ mm is the slit width, $L = 920$ mm is the length between detecter and slit, and the $\sigma_{\mathrm{FWHM}} = 3.670 \pm 0.002$ mm is the full-width half maximum of the distribution.

The spatial spectra of diffracted neutrons were subtracted for background by using the spatial distribution in the area where the diffraction conditions were not satisfied. As an illustration, the TOF spectrum and position distribution of (777) diffractions by a silicon wafer are displayed in Figure 3.11. Within the TOF spectrum, the section enclosed by the black line, where the diffraction wave was observed, is identified as the signal region. The position distribution within this region is indicated by the red line in the figure. In contrast, the background (BG) was computed from the position distribution in the TOF region both before and after the signal region. The BG of the signal region was interpolated by averaging the position distributions in the two areas marked by the black lines before and after the signal region. The intensity distribution of the interpolated BG is depicted by the blue line in the figure. Normalizing the neutron intensity involved subtracting the position distribution in the BG region (blue) from the position distribution in the signal region (red).

3.7 Specular Reflection of Near-epithermal Neutrons

The diffracted neutrons were incident to the mirror to measure the near-epithermal neutron reflection. The spatial distributions of the reflected neutrons are shown in Figure 3.12 with the diffracted neutrons. These spatial distributions subtracted the background distributions, which were obtained from the region of the unsatisfied Bragg condition. The neutrons diffracted by (111) observed at
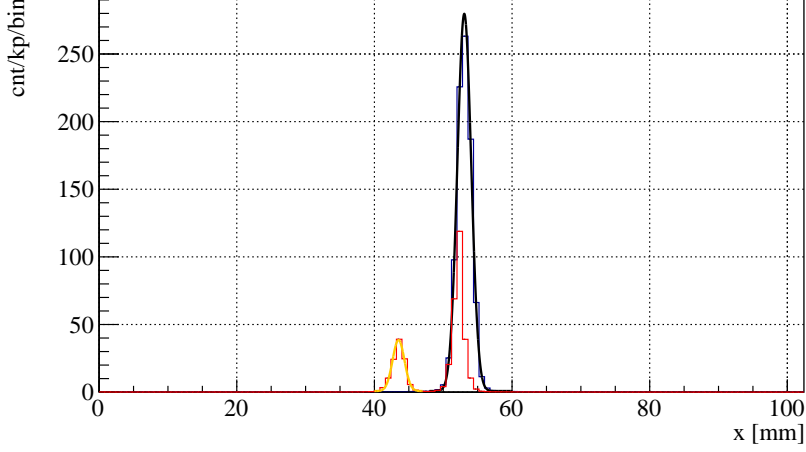
Figure 3.4: The distribution of the direct beam (blue) and reflected neutrons (red).

$x = 0$ mm (see Figure 3.12a). In the spatial distribution of higher-order diffraction (see Figure 3.12b–g), the diffracted neutrons were also observed around $x = 0$ mm. The diffraction by (222) and (666) were not observed consistently with the distinction law. The highest order diffraction we observed was (999).

In the spatial distribution with the mirror, the specular reflection of the neutrons diffracted by (111) was observed at $x = -5.5$ mm (see Figure 3.12a). The reflection angle at the mirror was $\theta_{\mathrm{R}} = 4.09$ mrad, which was obtained using the detection position and the length from the mirror to the detector. Since we used the monochromatic mirror, the reflections of diffracted neutrons of (333) and (444), which do not satisfy the reflectable momentum transfer of the mirror, were not observed (see Figure 3.12b, c). The significant reflection peaks of neutrons diffracted by (555), (777), (888), and (999) were observed in the range of $-9 < x < -5$ mm (see Figure 3.12e–g). Since the maximum energy of the reflected neutrons diffracted by (999) was 0.7 eV, we successfully observed the specular reflection of near-epithermal neutrons.

3.8   Reflection Angle of Near-epithermal Neutrons

To evaluate the reflection angle, we define the positional shift Δx as the difference between the position of the reflected neutrons and that of the diffracted neutrons. These positions of diffracted and reflected neutrons were obtained by fitting the spatial distribution with a Gaussian function. Monochromatic reflection is more reflective at $6Q_{\mathrm{c}} = 1.3$ nm^{-1} because the mirror used is $m = 6$. When the angle between the direct beam and the reflected beam is θ, the momentum transfer is written as

$$q = 4\pi \frac{\sin \theta/2}{\lambda}. \tag{3.3}$$

The position of the observed reflected neutron x is

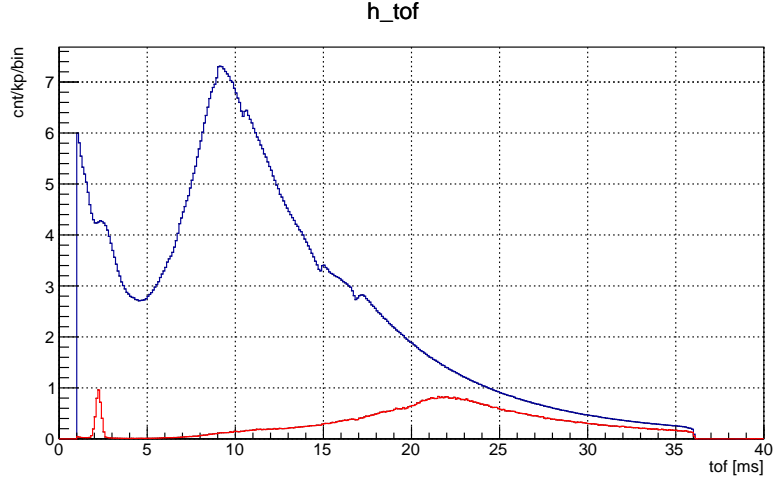$$\Delta x = L \tan \theta. \tag{3.4}$$

h_tof

Figure 3.5: The TOF spectra of direct beam (blue) and reflected neutrons (red).

the relationship between neutron wavelength λ and detection position x is

$$\frac{\Delta x}{\lambda} \approx \frac{6Q_{\mathrm{c}}L\lambda}{2\pi}, \tag{3.5}$$

where we use the approximation of $\tan\theta = \theta$, $\sin\theta = \theta$. The experimental values are the distance between the mirror center and the detector is $L = 665$ mm and the $6Q_{\mathrm{c}} = 1.3$ nm^{-1} represents the momentum transfer of the monochromatic reflection. Considering a mirror width of 300 mm and a beam width of 1.13 mm, the Eq.(3.5) has a following value:

$$\frac{\Delta x}{\lambda} = 136.5 \pm 30.2 \text{ mm/nm.} \tag{3.6}$$

The wavelength dependence of the measured positions of the reflected neutrons obtained in the experiment is shown in Figure 3.13. Since there is a linear relationship between reflection positional shift and wavelength, it was fitted with a linear function. The dependence between Δx and λ determined by the measurement was 112 ± 5 mm/nm. This measured value deviates from the expected design value by 19.7%, implying that the neutron beam isn't precisely hitting the center of the mirror. The beam's impact point on the mirror was 131 mm away from the mirror's center, which is notably shorter. Consequently, the actual mirror-to-detector distance was estimated to be 534 mm, accounting for the total mirror length of 300 mm. Given an angle of incidence of 4.09 mrad, a deviation of 131 mm in the z-direction corresponds to a displacement of 0.536 mm in the x-direction. This discrepancy is feasible, considering the inherent limitations in aligning the mirror accurately in the x-direction.

The detected position of the reflected neutron at $\lambda = 0$ was estimated through extrapolation via fitting and resulted in 1.84 ± 0.28 mm. This measurement poses a geometric issue since the slit width is 1.13 mm, rendering the obtained position geometrically impractical. This discrepancy is expected to the trajectory of diffracted neutrons caused by the silicon wafer. The positions where diffracted neutrons were observed without mirrors are illustrated in Figure 3.14 for each diffraction order. Notably, the direction of diffracted neutrons varies based on the diffraction order. The positions where diffracted neutrons are observed exhibit a shift of approximately 0.25 mm, all in the negative direction, corresponding to the direction where reflected neutrons are observed. This observation
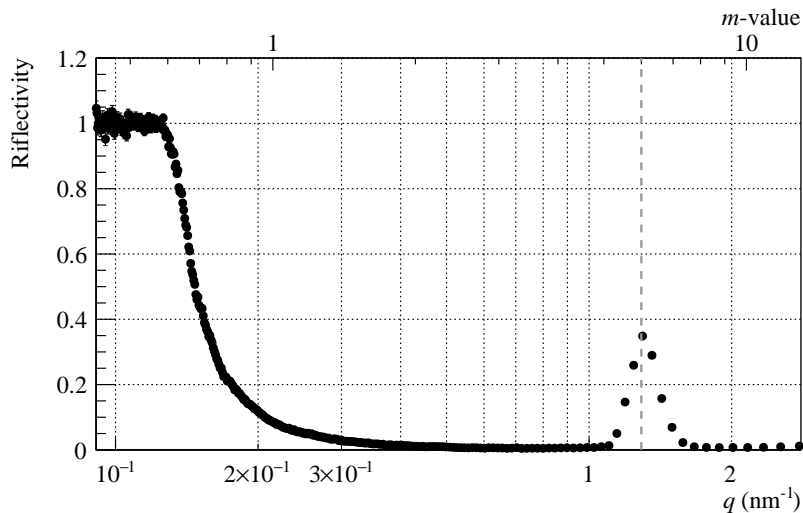
Figure 3.6: The measured reflectivity of the multilayer neutron mirror used in this experiment as a function of the neutron momentum transfer q. The dashed line represents $m = 6$, where the momentum transfer is $q = 1.3$ nm^{-1}.

suggests that the reflection angles become relatively shallower with higher diffraction orders. The cause of this problem is unknown and should be resolved in the next experiment.

3.9 Reflectivity of Near-epithermal Neutrons

The reflectivity R for each neutron energy was calculated using

$$R = \frac{I_{\text{reflection}}}{I_{\text{diffraction}} - I_{\text{grazing}}}, \tag{3.7}$$

where the $I_{\text{reflection}}$ was the intensity of reflected neutrons integrated with the region of $-14 < x < -4$ mm, I_{grazing} was the intensity of detected neutrons integrated with the region of $-4 < x < -1$ mm, and $I_{\text{diffraction}}$ was the intensity of diffracted neutrons integrated with the region of $-5 < x < 5$ mm. The I_{grazing} represents the neutrons that were not irradiated by the mirror. The observed reflectivity of each near-epithermal neutron is shown in 3.15, along with the cold neutron reflectivity as Designed R. The reflectivities of near-epithermal neutrons at (111), (333), and (444) were consistent with the designed value. In contrast, the reflectivity higher than (444) was not consistent with the design values. The reflectivity of (888) was $7.9 \pm 0.6\%$, which was unexpectedly smaller than the design value of 31.5%. It suggests a slight misalignment of the mirror position and rough surface of the mirror. The origin of this discrepancy has not been identified due to statistical limitations.

Finally, the observed reflectivity and positional shifts of each near-epithermal neutron are summarized in Table 3.1, along with the cold neutron reflectivity as Designed R. Improved measurement with better statistics would be necessary for the quantitative understanding of neutron reflectivity for practical applications. A more detailed discussion can be expected by increasing the statistics through future improvements, such as the use of the large m-value supermirror.
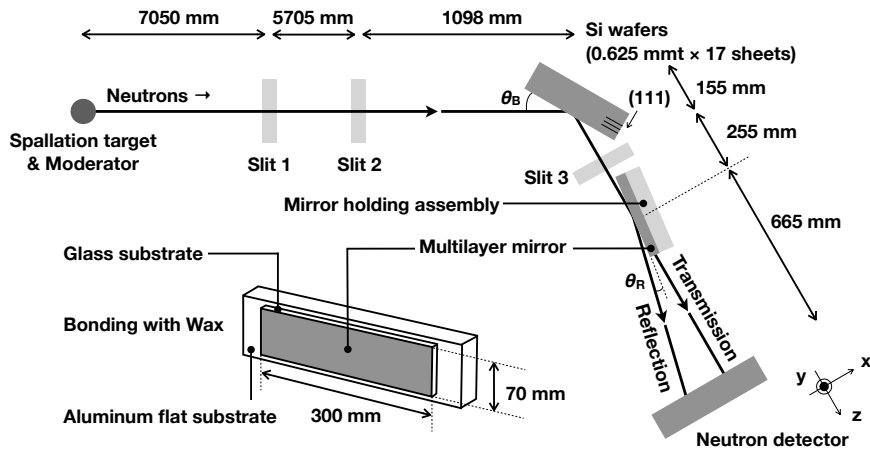
Figure 3.7: Schematic top view of the experimental setup at J-PARC MLF BL10. Note that the size of the figure is not in scale. The neutrons incident from the left side in this figure.

Table 3.1: The characteristics of neutrons diffracted by the silicon wafers.

Order	E (eV)	q (nm^{-1})	R (%)	Designed R (%)	Δx (mm)
(111)	0.008 58	0.166	25.3 ± 0.0	25.0	5.5 ± 0.0
(333)	0.0772	0.499	1.4 ± 0.0	0.9	—
(444)	0.137	0.666	2.1 ± 0.0	0.5	—
(555)	0.215	0.832	3.7 ± 0.1	0.6	8.5 ± 0.1
(777)	0.420	1.17	7.3 ± 0.5	9.3	6.6 ± 0.1
(888)	0.549	1.33	7.9 ± 0.6	31.5	6.0 ± 0.1
(999)	0.695	1.50	10.7 ± 2.9	6.8	5.1 ± 0.3

3.10 Conclusion

Given the recent utilization of pulsed neutron sources, there has been a growing demand for the practical implementation of reflective optics for epithermal neutrons across various fields. As a preliminary step toward achieving this reflective optics, the experimental confirmation of the optical reflection of near-epithermal neutrons was pursued. The reflective experiment employed a $m = 6$ multilayer neutron mirror with a slope error of 0.3 mrad. Diffracted neutrons from a silicon wafer were employed for the incident neutrons directed toward the mirror. This method allowed for the use of a low-noise environment with a neutron beam exhibiting a small divergence angle and facilitated the separation of reflected neutrons from direct beams. A μ-NID with a resolution of 350 µm was used as a neutron detector to observe small orbit changes of reflected neutrons. The optical reflections of epithermal neutrons were measured by employing grazing diffracted neutrons onto a mirror. The experimental findings revealed the observation of optical reflections of epithermal neutrons with energies up to 0.7 eV due to the achievement of large optical components with maintained accuracy. The positions at which the reflected neutrons were observed aligned with the expectations from geometric optics. However, the actual reflectivity deviated from the theoretical predictions by up to 24%. The cause of this variance remains unknown and is expected to be revisited and revalidated in the future with improved statistical analyses.

The realization of epithermal neutron reflective optics will lead to significant advances in exper-
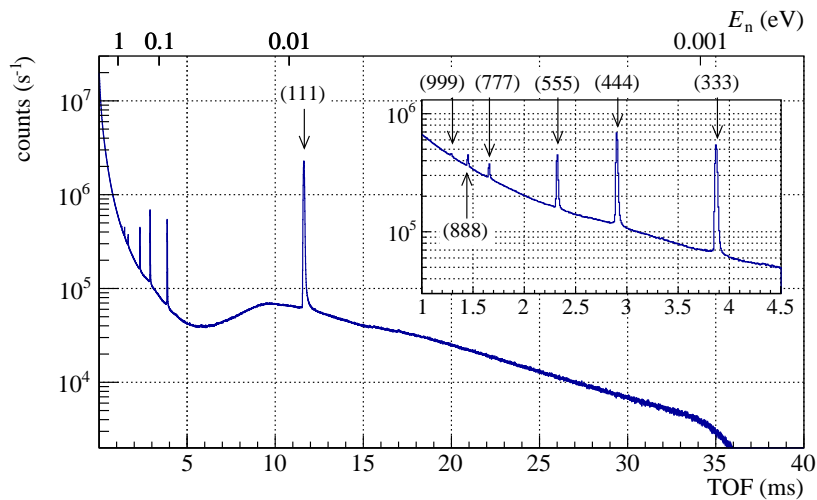
Figure 3.8: The TOF spectrum of the diffracted neutrons by the silicon wafers. The inset figure shows the enlarged spectrum in the TOF region from 1 ms to 4.5 ms.

imental systems. Mirrors with intricate shapes, including elliptical surfaces, have been successfully developed by depositing films onto Ni-P plated metal substrates[77]. Advancements in recent research have also expanded the methods for generating multilayer mirrors, contributing to the potential development of neutron mirrors with $m = 10$[93, 92]. This progress suggests that the fusion of these technologies could lead to the creation of an optical system adept at efficiently transporting epithermal neutrons.

The realization of epithermal neutron reflection optics can also be used to validate theories describing neutron optics. Neutron optics relies on an approximation where the potentials arising from individual nucleons are indistinguishable. However, the energy extent to which this approximation remains valid is yet undetermined. While certain studies have approached this issue theoretically, there has been no experimental verification. Exploring the adaptive boundaries of neutron optics becomes essential for its advancement. It not only aids in understanding the limits of the approximations utilized in describing neutron interactions but also quantifies their accuracy in constructing theoretical frameworks. Expanding the domain of neutron optics to include epithermal neutrons is poised to significantly contribute to the progression of various neutron experiments.

The near-epithermal neutron reflection measurement experiment can influence the experimental and theoretical system using neutron optics described above due to the realization by the development of a large element that maintained accuracy. This demonstrates that the development of large elements that maintain accuracy will advance neutron optics.
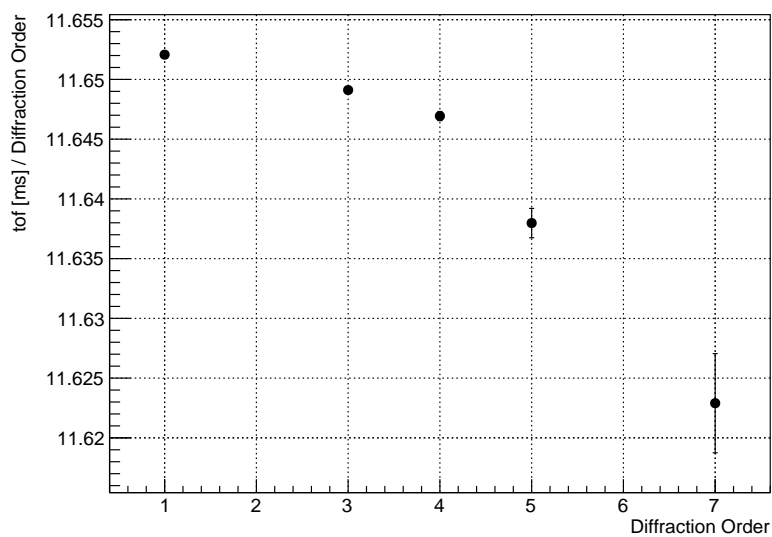
Figure 3.9: The normalized TOF of each diffraction.
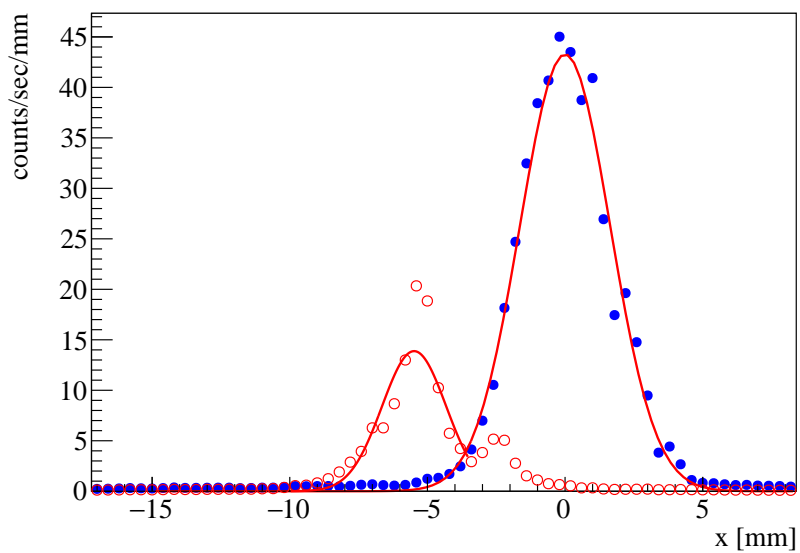
Figure 3.10: Spatial distribution of the transmitted (blue) and reflected (red) neutrons diffracted by (111) plane.
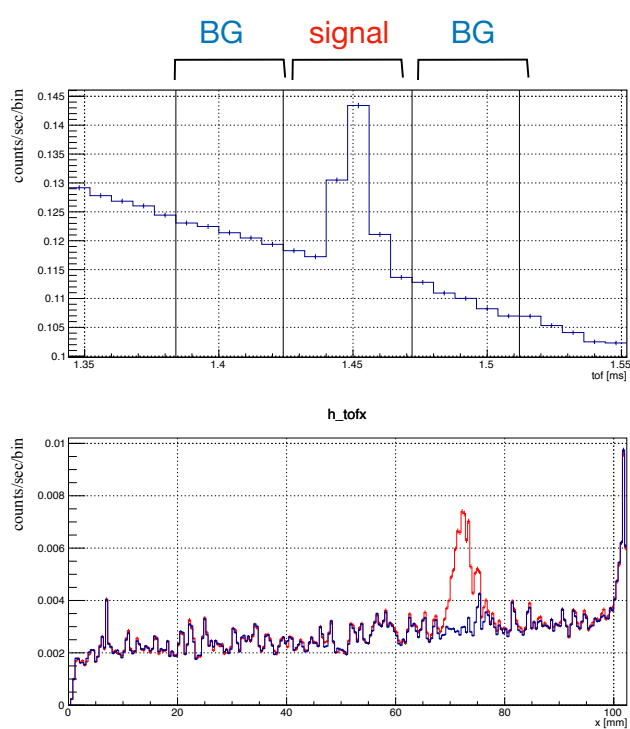
Figure 3.11: The TOF spectra (above) of diffracted waves by (777) reflected by a mirror, and their positional distribution (below).
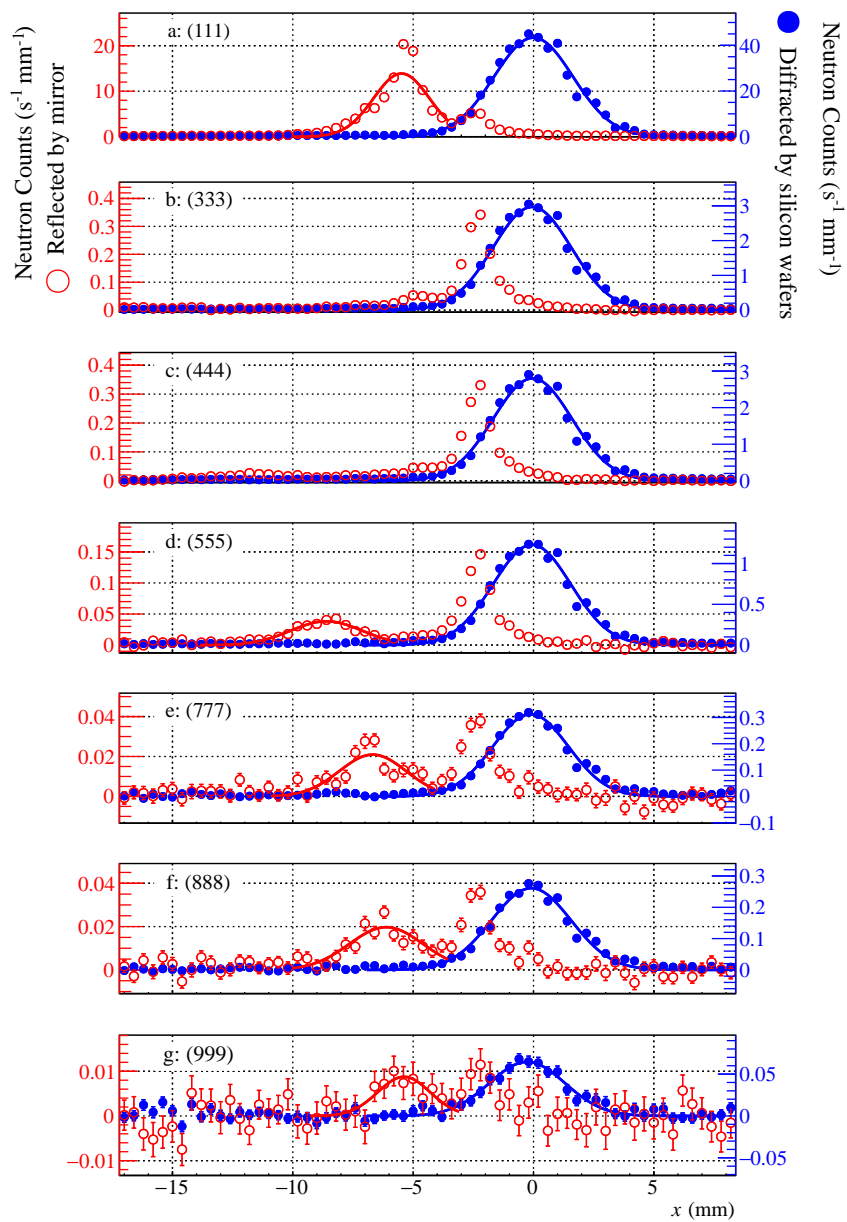
Figure 3.12: The spatial distributions of the neutrons diffracted by the silicon wafers (blue, closed circle) and reflected by the mirror (red, open circle). These distributions have included statistical uncertainties. The counts of neutrons diffracted by silicon wafers are shown on the right axis, and those reflected by the mirror are shown on the left axis. From top to bottom, they show (111) to (999) diffraction, respectively.
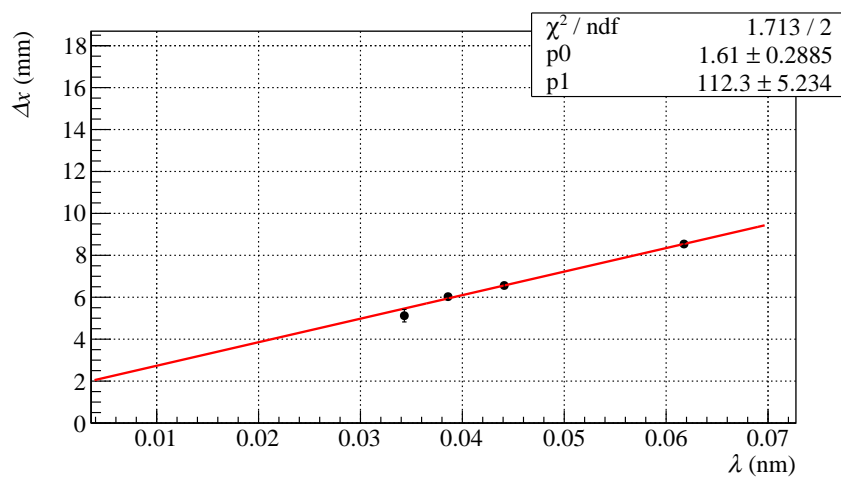
Figure 3.13: The wavelength dependence of the positional shift Δx.
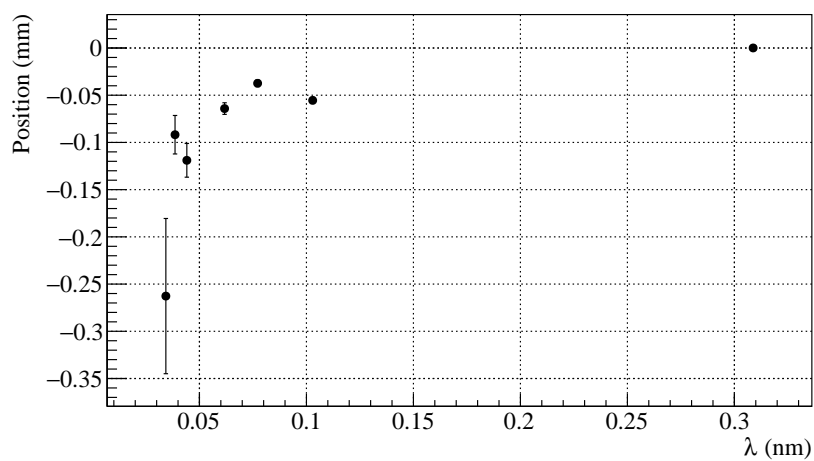
Figure 3.14: The detected position of the diffracted neutron by the Si wafer.
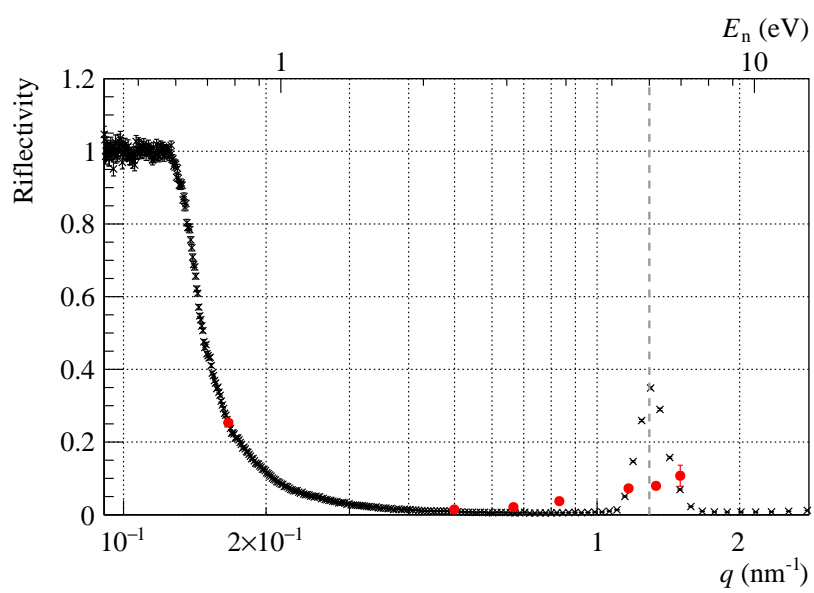
Figure 3.15: Reflectivity of epithermal neutrons plotted with results of reflectivity using cold neutrons.

Chapter 4

Demonstration of Improved Component Shape Accuracy: Pendellösung Interferometry

New physics, which can explain physical phenomena in general terms beyond the Standard Model of particle physics, predicts the existence of the fifth force. The fifth force can be described by measuring the gravitational interaction with an additional term, and search experiments are being conducted worldwide. Search experiments using neutrons can place strong limits on the effective distance on the nm scale, but their search range is far from the range predicted by the new physics, and a further improvement in search sensitivity is needed.

I have performed a search for the fifth force using pendellösung interferences. Pendellösung interferences are observed as interference fringes indicating interactions inside a crystal when neutrons are incident on a single crystal sample to satisfy the Bragg condition. While the interactions inside the crystal can be determined with high precision, the accuracy of the measurement is dictated by the experimental setup, such as the size of the crystal. In particular, the crystal thickness, which is the most dominant source of systematic error, must be determined with high precision. Therefore, we eliminated the term of crystal thickness from the experimental values by combining experiments using neutron interferometry. To eliminate this term, the sample thickness must be uniform over the entire area used in the experiment. In order to achieve uniform thickness of the sample, crystal fabrication was performed using ultra-precision machining techniques.

In previous studies, we have succeeded in updating the search range for the fifth force by up to two orders of magnitude in experiments using silicon single crystals. To extend this search range, we are planning to conduct experiments using germanium. In order to perform this experiment, we have calculated the range of the fifth force that can be explored by using germanium and processed the samples.

4.1   Pendellösung Interferometry

Pendellösung Interferometry is caused by the interference of waves inside single crystals with periodic potentials. This phenomenon was demonstrated in 1968 as neutron kinetic diffraction and has been the cornerstone of widely used neutron diffraction experiments[98]. Here we will understand pendellösung Interferometry using the wave function in periodic potentials as a starting point.

In the scattering by the periodic potential, the wave function of the scattered wave can be written

as

$$\psi\left(\mathbf{r}\right) = \sum_q \psi_q e^{i\mathbf{q}\cdot\mathbf{r}}. \tag{4.1}$$

The Schrödinger equation can be written as follows

$$\left(k_0^2 - (k_j + q)^2\right)\psi_q^j = \sum_{q'} v_{q-q'}\psi_q^j \tag{4.2}$$

where v is the eigenvalue of the wave function and can be written as follows

$$v(\mathbf{r}) = 2m\tilde{V}(\mathbf{r}) \tag{4.3}$$

using the Fourier transferred potential $\tilde{V}$. Considering the momentum transfer satisfying the diffraction condition in a scatterer with reciprocal lattice vector H up to second order, we can write it in terms of $q = 0$ and $q = H$. From this condition, the wave equation(4.2) can be expressed as

$$\begin{pmatrix} K_0^2 - k_0^2 + v_0 & v_{-H} \\ v_H & K_H^2 - k_0^2 + v_0 \end{pmatrix} \begin{pmatrix} \psi_0 \\ \psi_H \end{pmatrix} = 0, \tag{4.4}$$

where K_0, and $K_H = K_0 - H$ are the wave vectors inside the crystal, and the k_0 is the wave vector of incident wave. In order for this to have a non-zero solution, the secular equation of the left-term determinant must be zero. The incident neutron satisfying the diffraction condition can be written in terms of the following two wave vectors:

$$k_0^2 = v_0 + \frac{1}{2}\left(K_0^2 + K_H^2\right) \pm \sqrt{\frac{1}{4}\left(K_H^2 - K_0^2\right)^2 + v_H v_{-H}}, \tag{4.5}$$

$$k_0^2 = v_0 + \frac{1}{2}\left(K_H^2 - K_0^2\right) + K_0^2 \pm \sqrt{\frac{1}{4}\left(K_H^2 - K_0^2\right)^2 + v_H v_{-H}}. \tag{4.6}$$

It can be seen that K_0 has two states. Here, the component of K_0 perpendicular to H is defined as K_ζ, and the parallel component as K_ξ. When the neutrons incident on the crystal, K_ζ causes a slight wavenumber shift δK_0 by the refractive index. The wave vector inside the crystal can be written as

$$K_\zeta^\pm = k_0^2 - \frac{1}{4}H^2 + (\delta K_0)^2 - v_0 \mp \sqrt{(\delta K_0 H)^2 + v_H v_{-H}}, \tag{4.7}$$

where the solution at $\delta K_0 = 0$ is the wave vector of incident neutrons with momentum corresponding to the exact Bragg condition, and δK corresponds to the vector component of the internal crystal wave along the Bragg plane. Each solution in $\pm$ of Eq. (4.7) creates two dispersion surfaces. A dispersion surface is a hyperbola connecting the points where $K_H + K_0 = H$ when shifted by δK. The relationship between the momentum of incident neutrons in the crystal and the dispersion surface is shown in Figure 4.1. The separation due to dispersion by δK depends on v_H and thus on the potential between the scattering center and the neutrons. From this, the effective refractive index can be written as

$$n^\pm = \frac{K_\zeta^\pm}{k_0} = \left(1 - \frac{1}{k_0^2}\left(v_0 + \delta K_0 H \pm \sqrt{(\delta K_0 H)^2 + v_H v_{-H}}\right)\right)^{\frac{1}{2}} \tag{4.8}$$

$$\approx 1 - \frac{1}{2k_0^2}\left(v_0 + \delta K_0 H \pm \sqrt{(\delta K_0 H)^2 + v_H v_{-H}}\right) \tag{4.9}$$

It can seen that there are two different effective refractive indices in each of the two eigenstates, which physically lead to two eigenstates. These two eigenstates are generally called the α state and the β
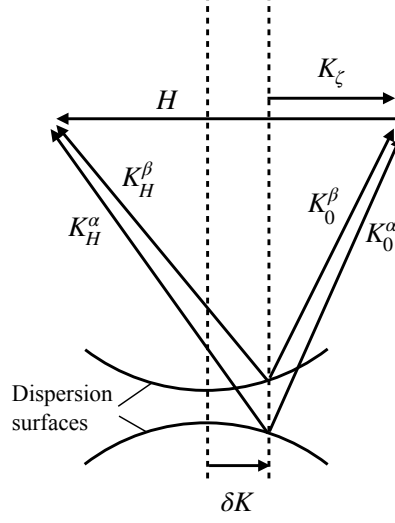
Figure 4.1: dispersion surface.

state, and interference fringes are obtained when they interfere with each other. Rewriting the wave numbers inside the crystal using these different refractive indices, we obtain

$$K_0^\alpha = n^+ k_0 \tag{4.10}$$

$$K_0^\beta = n^- k_0 \tag{4.11}$$

$$K_H^\alpha = \left(1 - n^+\right) k_0 \tag{4.12}$$

$$K_H^\beta = \left(1 - n^-\right) k_0 \tag{4.13}$$

and the wave function inside the crystal can be rewritten as follows

$$\Psi\left(\mathbf{r}\right) = \psi_0^\alpha e^{i\mathbf{K}_0^\alpha \cdot \mathbf{r}} + \psi_0^\beta e^{i\mathbf{K}_0^\beta \cdot \mathbf{r}} + \psi_H^\alpha e^{i\mathbf{K}_H^\alpha \cdot \mathbf{r}} + \psi_H^\beta e^{i\mathbf{K}_H^\beta \cdot \mathbf{r}}. \tag{4.14}$$

where ψ_0^α and ψ_0^β denote the amplitudes of diffracted transmitted waves, and ψ_H^α and ψ_H^β denote the amplitudes of diffracted reflected waves. By adapting the two refractive indices to the Eq. (4.4), the wave function outside the crystal can be written as

$$\frac{\psi_H^{\alpha,\beta}}{\psi_0^{\alpha,\beta}} = \frac{\left(K_0^{\alpha,\beta}\right)^2 - k_0^2 + v_0}{-v_{-H}} = \frac{-v_H}{\left(K_H^{\alpha,\beta}\right)^2 - k_0^2 + v_0}. \tag{4.15}$$

The respective amplitudes satisfied

$$\psi_0^\alpha + \psi_0^\beta = 1, \ \psi_H^\alpha + \psi_H^\beta = 0 \tag{4.16}$$

by the boundary conditions. From these expressions (4.9), (4.15), and (4.16), we obtain the wave

function inside the crystal

$$\psi_0^\alpha \;=\; \frac{1}{2}\left(1 - \frac{\delta K_0 H}{\sqrt{(\delta K_0 H)^2 + v_H v_{-H}}}\right) \tag{4.17}$$

$$\psi_0^\beta \;=\; \frac{1}{2}\left(1 + \frac{\delta K_0 H}{\sqrt{(\delta K_0 H)^2 + v_H v_{-H}}}\right) \tag{4.18}$$

$$\psi_H^\alpha \;=\; -\frac{1}{2}\frac{v_H v_{-H}}{\sqrt{(v_H v_{-H})^2 + (\delta K_0 H)^2}}\sqrt{\frac{v_H}{v_{-H}}} \tag{4.19}$$

$$\psi_H^\alpha \;=\; +\frac{1}{2}\frac{v_H v_{-H}}{\sqrt{(v_H v_{-H})^2 + (\delta K_0 H)^2}}\sqrt{\frac{v_H}{v_{-H}}} \tag{4.20}$$

which is the wave function inside the crystal.

For the wave function at the crystal outgoing surface, since the wave number of the diffracted wave must return to the incident energy, the wave function can be written as

$$\chi(\mathbf{r}) = \chi_0 \exp(i\mathbf{k}_0 \cdot \mathbf{r}) + \chi_H \exp(i\mathbf{k}_H \cdot \mathbf{r}) \tag{4.21}$$

which wave vector of the diffracted wave satisfies $k_H = k_0$. When considered as a vector, its value is

$$\mathbf{k}_H = \mathbf{k}_0 + \mathbf{H} + \delta\mathbf{K_0} \tag{4.22}$$

The incident neutron interacts with the potential for the length affected by the potential, in other words, for the thickness D of the crystal. The phase shift of the wave vector ϕ_P can be written as

$$\phi_P = \int_D d\zeta \left(K_\zeta^\alpha - K_\zeta^\beta\right). \tag{4.23}$$

The length of interaction within the crystal depends on δK_0. The difference of wave vectors propagated in the crystal can be expressed from Eq.(4.7) as

$$\phi_P = D\frac{\sqrt{v_H v_{-H}}}{K_{\zeta B}}\sqrt{\eta^2 + 1}, \tag{4.24}$$

where the η is the wave vector displacement weighted by $v_H v_{-H}$, which can be written as

$$\eta \equiv \frac{\delta K_0 H}{\sqrt{v_H v_{-H}}}. \tag{4.25}$$

Since the phase shift between the two wavenumber vectors depends on the thickness of the crystal, a variable called the pendellösung length is defined

$$\Delta_H \equiv \frac{\pi H}{\sqrt{v_H v_{-H}}}\frac{1}{\tan\theta_B}. \tag{4.26}$$

The boundary conditions for the wave function outside the crystal

$$\chi_0 \;=\; \psi_0^\alpha + \psi_0^\beta \tag{4.27}$$

$$\chi_H \;=\; \psi_H^\alpha + \psi_H^\beta \tag{4.28}$$

The wave function Eq. (4.14) rewritten using this condition is

$$\chi_H^2 \quad = \quad \frac{1}{1+\eta^2} \sin^2\left[\frac{\pi D}{\Delta_H}\sqrt{1+\eta^2}\right] \tag{4.29}$$

$$\chi_0^2 + \chi_H^2 = 1 \tag{4.30}$$

where χ^2 denotes the probability density, and absorption in the crystal is neglected. The position Γ in the emitting plane of the crystal normalized by θ_B is written as

$$\Gamma = \frac{\tan\Omega}{\tan\theta_B} = \frac{y}{1+y^2} = \frac{x}{D\tan\theta_B} \tag{4.31}$$

where the defining region is $-1 < \Gamma < 1$. The incident neutrons leave the crystal via the path shown in Figure 4.2. The intensity distributions of forward and reflected diffraction waves can be described
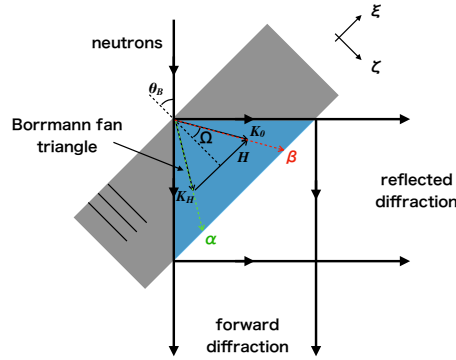
Figure 4.2: Relationship between incident neutrons and crystals in Laue diffraction.

by the superposition of these waves. This can be written using Γ as

$$I_0(\Gamma) \quad = \quad \frac{1-\Gamma}{(1+\Gamma)\sqrt{1-\Gamma^2}}\cos^2\left[\frac{\pi D}{\Delta_H}\sqrt{1-\Gamma^2}+\frac{\pi}{4}\right] \tag{4.32}$$

$$I_H(\Gamma) \quad = \quad \frac{1}{\sqrt{1-\Gamma^2}}\sin^2\left[\frac{\pi D}{\Delta_H}\sqrt{1-\Gamma^2}+\frac{\pi}{4}\right] \tag{4.33}$$

Note that the phase of the periodic function is shifted by $\pi/4$ from the Eq. (4.30)[99]. The more exact solution is represented by a spherical wave, see the following references [100, 101, 102, 103] for a discussion.

4.2 Phase Shift of Pendellösung Fringe

Pendellösung interference relies on both the average momentum of the neutron beam along the Bragg plane and the geometry of the position-space slit used. The dynamic diffraction Hamiltonian, along with the corresponding Green's function inside the crystal, is most easily solved in the coordinate system (ξ, ζ), where ξ is parallel to H, and ζ is parallel to the mean momentum of the neutron. In Laue geometry, ξ-direction is parallel, and ζ-direction is perpendicular to the crystal plane. Greek

letters are used for crystal coordinates and Latin letters for beam coordinates. In beam coordinates, z is vertical, and x is horizontal. It is evident that pendellösung interference fringes, which depend on Γ, can only be resolved at the center of the Bormann fan. In addition to the loss of visibility of interference fringes due to the k_ζ-dependence of the pendellösung phase shift, pendellösung oscillations can only be resolved at the center of the Bohrman fan. To illustrate this point, consider the position-space neutron profile of the diffracted beam with respect to the beam coordinates.

$$|\langle x \mid \psi \rangle|^2 = \int dk_\zeta \, |\langle k_\zeta \mid \psi_0 \rangle|^2 \, \frac{1 + \sin\left[\frac{2\pi D}{\Delta_H}\sqrt{1-\Gamma^2}\right]}{\sqrt{1-\Gamma^2}} \tag{4.34}$$

where x is the displacement of the incident wave packet, which must be averaged over the incident slit, while x' is the outgoing position, which is ultimately averaged over the outgoing slit. Since the Bormann fan is defined by $-D\sin\theta_{\mathrm{B}} < (x'-x) < D\sin\theta_{\mathrm{B}}$, the denominator and argument of the sin function are always real numbers. For the crystal thickness used in this experiment, the sinusoidal part becomes highly oscillatory at the edge of the Bormann fan $(x'-x) \to \pm D\sin\theta_{\mathrm{B}}$ because the crystal thickness is much larger than the pendellösung length $D \gg \Delta_H$. This function is plotted in Figure 4.3. Resolvable pendellösung oscillations occur only in the center of the Bormann fan, the region defined by $-\sqrt{D\Delta_H}\sin\theta_{\mathrm{B}} < (x'-x) < \sqrt{D\Delta_H}\sin\theta_{\mathrm{B}}$.
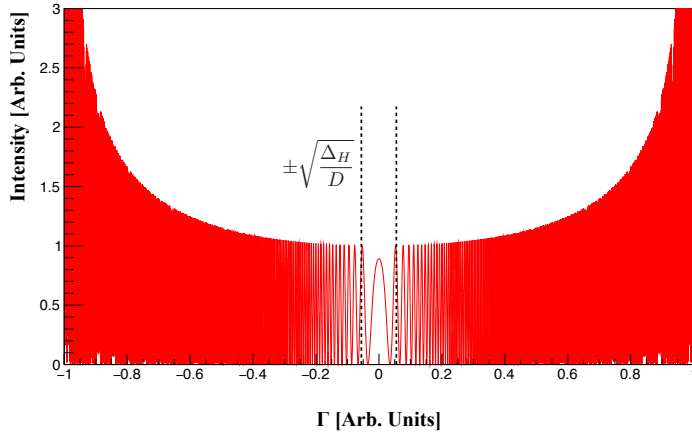
Figure 4.3: The spatial intensity distribution of reflected diffraction waves of pendellösung interference fringes. I used these parameters to calculate this fringe: $\Delta_H = 21$ μm, $D = 6.68$ mm, and $\theta_B = 44$ deg.

It is clear that the integrated intensity of the central part can be written as $2\pi D/\Delta_H$ from the Eq. (4.33). This can be written as a change in the crystal thickness D as follows

$$I(\theta_P) = A + B\cos\left(\frac{2\pi\phi_{\mathrm{P}}}{\cos(\theta_P - \theta_0)} + \phi_{\mathrm{calc}}\right) \tag{4.35}$$

where the parameter $\phi_{\mathrm{P}} = \frac{D}{\Delta_H}$ has interesting value and ϕ_{calc} is a constant determined by the collimation condition, generally $\pi/4$. The A and B are constants determined by the beam intensity and background. The parameter θ_{p} is the rotation by an axis perpendicular to the crystal plane, which changes the effective thickness of the crystal. From this, the observed interference fringes are shown in the Figure 4.4. The physical parameters are determined by this interference fringe.

Figure 4.4: The Observable intensity distribution of the pendellösung oscillation.

4.3 Averaged Crystal Potential

The integrated pendellösung interference fringes lead the pendellösung length, which can be written using the effective potential v_H as

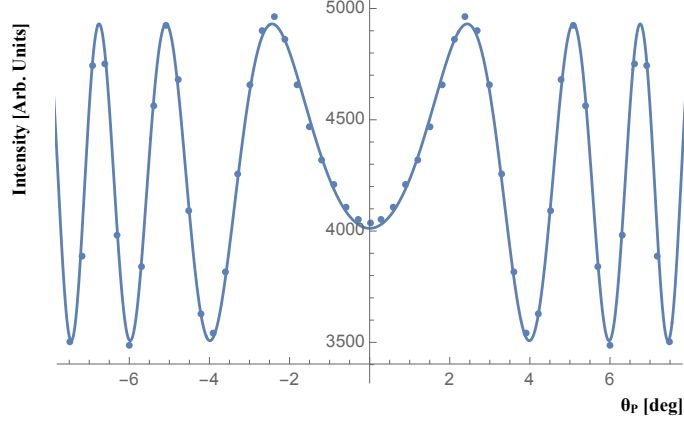$$\Delta_H = \frac{\pi H}{v_H \tan \theta_{\mathrm{B}}} \tag{4.36}$$

where the effective potential can be written in terms of a Fourier expanded potential from Eq. (4.3). For periodic potentials, the periodic structure is disturbed by temperature factors, inelastic neutron phonon scattering, thermal diffuse scattering, cubic anharmonic effect, and these higher-order terms. When only first-order terms are considered, the averaged potential is associated with only one reciprocal lattice vector, and the single term of the sum over H is conserved. Thus, the averaged potential can be written as

$$v_H = 2m\tilde{V} = \frac{2m}{a^3}\tilde{V}(H)\left\langle \sum_n \exp\left(i\mathbf{H}\cdot\mathbf{x}_n\right)\right\rangle \tag{4.37}$$

where the inside of the bracket represents the temperature average. The potential term is described by Fermi pseudopotentials. The Fourier expanded potential using periodicity can be written as

$$\tilde{V} = \frac{2\pi}{m}b(Q) \tag{4.38}$$

where $b(Q)$ is the scattering length depending on the momentum transfer, which parameter can be written using nuclear scattering b_{N}, electromagnetic scattering b_{EM}, and fifth force b_5 as follows

$$b(Q) = b_{\mathrm{N}} + b_{\mathrm{EM}}(Q) + b_5(Q) \tag{4.39}$$

In the following subsections, each of these terms will be explained.

Temperature Factor

The inside term of brackets in Eq. (4.37) can be separated into temperature-dependent and non-temperature-dependent terms.

$$\langle \exp\left(i\mathbf{H} \cdot \mathbf{x}_n\right) \rangle \rightarrow \exp\left(i\mathbf{H} \cdot \mathbf{x}_n\right) \langle \exp\left(i\mathbf{H} \cdot \mathbf{u}_n\right) \rangle \tag{4.40}$$

Here, the temperature-independent term is defined as

$$K_H \equiv \exp\left(i\mathbf{H} \cdot \mathbf{x}_n\right). \tag{4.41}$$

This value is determined by the crystal structure used. For materials with diamond structure, such as silicon and germanium, the value depends on the crystal plane and can be written as

$$K_H = \sum_n \exp\left(i\mathbf{H} \cdot \mathbf{x}_n\right) = \begin{cases} 8 & \text{for } h+k+l = 4m \\ \sqrt{32} & \text{for } h+k+l = 4m \pm 1 \\ 0 & \text{for } h+k+l = 4m \pm 2 \end{cases} \tag{4.42}$$

where the (h, k, l) represents Miller index of the crystal, and the m is natural number. Noteworthy is the case $h + k + l = 4m \pm 2$, in which the diffraction intensity is zero, which is called the forbidden rule.

The u_n is represented using the phonon generation and annihilation operator since the crystal has a periodic potential. At this point, $\mathbf{u}(\mathbf{x})$ in Eq. (4.40) is written as follows

$$\mathbf{u}(\mathbf{x}) = \int d^3k \sqrt{\frac{1}{2m\omega_k}} \left(\mathbf{a}_k + \mathbf{a}_{-k}^\dagger \exp\left(i\mathbf{k} \cdot \mathbf{x}\right) \right) \tag{4.43}$$

where the a_k is the generation and annihilation operator of the phonon, which is written as

$$a_k |n_k\rangle = \sqrt{n_k} |n_k - 1\rangle \tag{4.44}$$

$$a_k^\dagger |n_k\rangle = \sqrt{n_k + 1} |n_k + 1\rangle \tag{4.45}$$

the crystal temperature factor can be written as follows

$$\langle \exp\left(i\mathbf{H} \cdot \mathbf{u}\right) \rangle = \exp\left[-\frac{1}{2} \left\langle (\mathbf{H} \cdot \mathbf{u})^2 \right\rangle \right] = \exp \langle \mathbf{H} \cdot U \cdot \mathbf{H} \rangle = e^{-W} \tag{4.46}$$

where the U is the mean square displacement matrix, which is written as $U_{ij} = u_i u_j$[104]. The component of U is called the anisotropic mutation parameter (ADP) [105]. The occurrence of the off-diagonal components in U depends on the symmetry of the system. From there, the exponent of the Eq. (4.46) can be written as

$$W = \frac{1}{2} \langle \mathbf{H} \cdot \mathbf{u} \rangle^2 = \frac{1}{2} \mathbf{H} \cdot U \cdot \mathbf{H} = \frac{1}{6} \mathbf{H}^2 \langle u^2 \rangle = \frac{B}{16\pi^2} H^2 \tag{4.47}$$

where B is the called temperature factor (or Debye–Waller factor), which can be used to write down the temperature-dependent potential of the crystal. The measured value and theoretical calculations of the temperature factor have been done in the past, see the reference[106] for measurements in germanium and reference[107] for theoretical calculations.

Neutron-Electric Scattering Length

The potential in momentum space at the neutron electron scattering length can be written using Dirac factor F_1 and Pauli factor F_2 as

$$\tilde{V}(Q) \quad = \quad j_n^\mu \tilde{A}_\mu(Q) \tag{4.48}$$

$$= \quad \bar{u}(p') \left(\gamma^\mu F_1 + \frac{\sigma^{\mu\nu} q_\nu}{2m_n} F_2 \right) u(p) \tilde{A}_\mu(Q) \tag{4.49}$$

where the u is the spinor of Dirac, γ^μ is matrix of Dirac, and $\sigma^{\mu\nu} = \frac{i}{2}[\gamma^\mu, \gamma^\nu]$[108]. The momentum transfer $(p' - p)^2 = -Q^2 = -\mathbf{q}^2$, which can be written as $|p' - p|^2 = Q^2 \ll m^2$. $\tilde{A}(Q)$ is the 4-dimensional potential in the crystal. Let $G_E(Q)$ be the shape factor for scattering by electrons and $G_M(Q)$ be the shape factor for scattering by magnetism. It can be expanded by Q^2 in the low energy region.

$$G_E(Q) = F_1(Q^2) - \frac{Q^2}{4m^2} F_2(Q^2) \tag{4.50}$$

$$G_M(Q) = F_1(Q^2) + F_2(Q^2) \tag{4.51}$$

It is these form factors that are obtained experimentally. Here we consider G_E, the coupling between the neutron current and the electrostatic potential Q. The relation between G_E and Q is obtained by scattering electrons onto a target containing neutrons. The formulation of this form factor has also been studied in recent years. However, this is completely different from the energy band used in this experiment. To discuss this at low energies such as those used in this experiment, we only need to consider the slope of $G_E(Q)$ near $Q \sim 0$.

$$G_E(Q) \quad = \quad \left(\frac{\partial F_1}{\partial(Q^2)} \right) Q^2 - \frac{F_2}{4m^2} Q^2 \tag{4.52}$$

$$= \quad -\frac{1}{6} \left\langle r_n^2 \right\rangle Q^2 \tag{4.53}$$

where $\left\langle r_n^2 \right\rangle$ is the effective charge radius of the neutron, $\left\langle r_n^2 \right\rangle = -0.1161 \pm 0.0022 \text{ fm}^2$[109]. The neutron electron scattering length at this time can be written as

$$b_E(Q) \quad = \quad \frac{1}{3a} \left(\frac{m}{m_e} \right) \left\langle r_n^2 \right\rangle Z \left[1 - f_e(Q) \right] \tag{4.54}$$

$$= \quad -b_{ne} \left[Z - f_e(Q) \right] \tag{4.55}$$

where the Z is atomic number and $f_e(Q)$ is the atomic form factor[110]. The atomic form factor takes different values for different atoms and can be obtained either by experimental Bragg diffraction using x-rays or by calculations using Confucius mechanics[111, 112, 113].

Fifth Force

The fifth force is expressed by adding an additional term to the gravitational interaction that can be described by the universal law of gravitation. This is called the Yukawa potential, which represents an interaction that does not obey the inverse square law at short distances. In this case, the potential that the neutron undergoes can be written as

$$b_5(Q) \quad = \quad -\frac{m}{2\pi} g^2 Q_n Q_N \frac{\lambda_5^2}{1 + Q^5 \lambda^2} \tag{4.56}$$

$$= \quad \alpha_G 2Gm^2 M \frac{\lambda_5^2}{1 + Q^2 \lambda_5^2} \tag{4.57}$$

where g^2 is the coupling constant and Q_n and Q_N are the neutron and nuclear charges, respectively[114]. The fifth force is found to depend on the mass M of the matter. Therefore, experiments with multiple nuclei are useful to evaluate unknown systematic errors in exploratory experiments.

4.4 Combined measurement using Neutron Interferometer

Measurements of the integrated pendellösung interference fringes allow for measurements of the crystal temperature factor, the neutron electron scattering length, and even a search for the fifth force. However, the only value obtained by experiment is the period ϕ_P given by the Eq. (4.35). In this section, we describe a method for precisely determining the scattering length from experimental data.

The phase shift determined by the measurement of pendellösung interference is written as

$$\phi_P = \frac{D}{\Delta_H} = \frac{v_H D}{2\pi k \cos\theta_B} \tag{4.58}$$

where the D is crystal thickness, k is the wave vector of incident neutron, and the θ_B is the Bragg angle. The term of $k\cos\theta_B$ can be written as

$$k\sin\theta_B = \frac{H}{2\tan\theta_B} \tag{4.59}$$

using Bragg condition. The H represents the reciprocal lattice vector, which is determined by

$$H = \frac{2\pi a}{\sqrt{k^2 + h^2 + l^2}} \tag{4.60}$$

where the h, k, l is the Miller index, and the a is the lattice constant, whose value is well determined by previous research. The θ_B is determined by the 2 measurements with high precision encoder, which is the plus Bragg condition and minus Bragg condition with the same lattice plane. By using the difference between the encoder values in each measurement, the phase shift and Bragg angle can be determined to a first-order approximation.

The remaining term, crystal thickness, is eliminated using a neutron interferometer measurement. The neutron interferometer can measure the forward scattering length by crystals. The obtained phase shift by the inserted sample using the crystal interferometer can be written as

$$\phi_I = \langle b \rangle \lambda D = \frac{16}{a^2\sqrt{3}} 4\pi v_0 D \sin\theta_I \tag{4.61}$$

where the $\langle b \rangle$ is the scattering density, given by the product of the scattering length and the atomic density. The θ_I is the Bragg angle for neutron interferometer, whose value can determined with high precison by the same method of pendellösung measurements. The ratio of the phase shift obtained from pendellösung interferometry to that obtained from interferometry can be written as

$$\frac{\phi_P}{\phi_I} = \frac{2v_H \tan\theta_{PB} H_I}{v_0 \sin\theta_{BI} H_P} \tag{4.62}$$

where the θ_{PB} is the Bragg angle for pendellösung interference measurement, θ_{BI} is the Bragg angle for neutron interferometer, H_P is the reciprocal lattice vector for pendellösung interference measurement, and H_I is reciprocal lattice vector for neutron interferometer. The crystal thickness term is eliminated from the two measurements.

Finally, the interesting scattering length can be written from the ratio of the phase shifts obtained by the two measurements as

$$\frac{v_H D_{\mathrm{P}}}{v_0 D_{\mathrm{I}}} = e^{-W}\left(1 - (1 - f_{\mathrm{e}}(Q))\frac{b_{\mathrm{ne}}}{b(0)} + \frac{b_5(0) - b_5(0)}{b(0)}\right) \tag{4.63}$$

where the D_{P} is the crystal thickness for pendellösung measurement, D_{I} is the crystal thickness for interferometer measurement, whose values are assumed as same. The $b(0)$ is the literature value of forward scattering length, which generally refers to the nuclear scattering length, but since the fifth force term was not assumed in the previous experiment, the experimental value is written as the forward scattering length. By using the atomic structure factor of literature values, the temperature factor and neutron-electric scattering length can be determined, and a fifth force can be explored. These values are determined from the momentum dependence of the averaged potential.

4.5 Accuracy Requirement for Crystal

Since the two experiments, which are pendellösung experiment and interferometer experiment, are performed independently, the sample thickness must be uniform for all measurements. The accuracy of phase shift determination is about 5×10^{-5} in all experiments. For a 5 mm thick sample, the required accuracy of the crystal thickness is about 0.25 µm. In practice, the phase shift is affected by the average thickness of the area irradiated by the beam, so the peak-to-valley (PV value) value of the sample thickness must be smaller than ~ 1 µm. This process also helps to improve the contrast of the resulting interference fringes.

I used silicon and germanium single-crystal samples with good single-crystalline quality for our neutron experiments. The overview photograph of the germanium crystal used in this experiment is shown in Figure 4.5. Germanium single crystals are bonded to low thermal expansion cast metal with wax. These materials, categorized as hard brittle material, are typically processed using abrasive techniques due to their propensity for brittleness and cracking. Abrasive processing is effective for achieving a mirror-like finish on the workpiece surface. However, controlling the amount of polishing is challenging because it involves wandering abrasive grains. Specifically, when using a lapping machine, the workpiece often ends up with a convex shape due to increased abrasive contact towards the edges. Consequently, the parallelism of the workpiece is limited to ~ 10 µm, complicating the precise assurance of parallelism in relation to slope error. Moreover, the accuracy is significantly influenced by how the workpiece is positioned, which adds to the difficulty in ensuring reproducibility.

I addressed this problem by machining the crystal using one of the advanced machining technologies, specifically grinding with an ultra-precision machining system. Grinding is an abrasive machining process based on the motion transfer method. It involves a forced infeed approach where the tool receives a fixed infeed, and the tool's motion trajectory is precisely transferred to the workpiece. The process needs to make a rotating grinding wheel contact the workpiece. The machining amount is directly linked to the machining accuracy through the tool path of cut and feed accuracy to the workpiece. Hence, to achieve high machining accuracy, the machine's structure and motion mechanism need to be highly rigid, and a fine, accurate tool feed is essential. Furthermore, the tool must be composed of a material that is both rigid and resistant to wear, and it must be finished with a high level of precision. In other words, if the machine tool and the tool possess a highly rigid and accurate motion mechanism, the precision of the machine tool can be transferred to the workpiece with equivalent accuracy. High repeatability in machining is attainable as long as the tool's geometry remains consistent.

Machining of workpieces is typically carried out through plastic deformation, which persists even after the removal of an external force. The counterpart process is elastic deformation. The deformation experienced by a workpiece due to plastic deformation can be categorized into two main modes: brittle
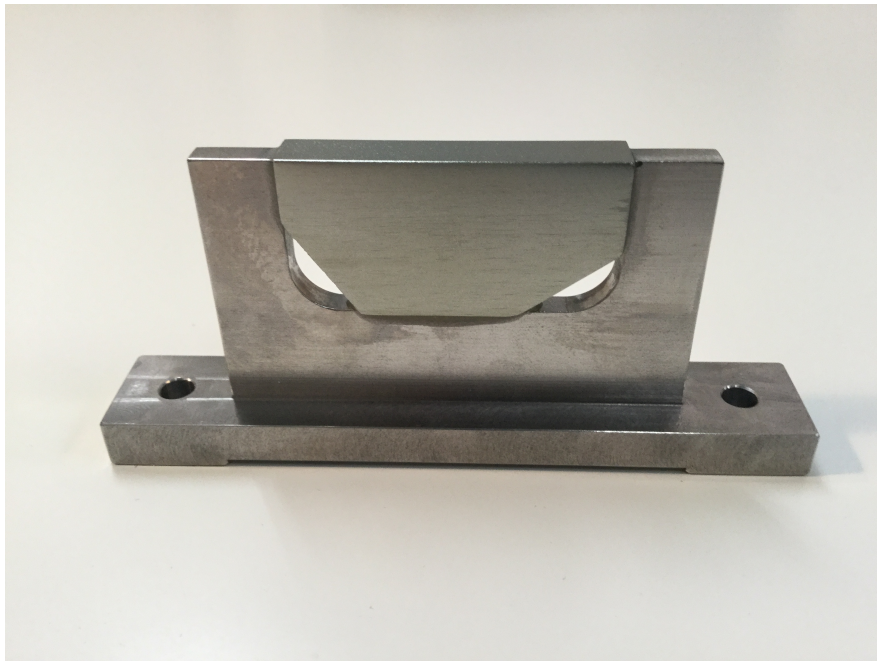
Figure 4.5: Germanium crystal fixed on holding tool.

fracture and ductile fracture. A brittle fracture refers to the instantaneous failure of a workpiece that occurs primarily at high strengths. The surface of a workpiece subjected to brittle fracture breaks along a fracture plane known as the plane of fracture. Conversely, in ductile fracture, the fractured area is transferred to the workpiece surface through the formation of a machining alteration layer. Silicon and germanium are classified as brittle materials and generally undergo brittle fracture. However, it is recognized that ductile fracture can be achieved by machining at a thickness below the cut thickness, known as the ductile-to-brittle transition point (denoted as dc-value). This dc-value is generally around 100 nm, and plastic working is attained by maintaining a depth of cut smaller than this value.

Ultra-precision machining of silicon and germanium samples was conducted using an ultra-precision machining device equipped with a grinding wheel. The shape measurements of the machined germanium specimens are presented in Figure 4.6. The crystal thickness ranged from 6.6940 – 6.651 mm, and the maximum error in the crystal thickness was effectively machined to less than 1.1 µm within the 10×10 mm^2 area of neutron irradiation. This level of shape accuracy aligns with the accuracy required for this study and is sufficiently precise not to impede the experiment. For a detailed description of germanium processing, see Ref. [115].

A work alteration layer, devoid of crystal structure, forms on the surface treated with ductile machining. This layer is uniformly removed from the entire crystal through a chemical etching process, which eliminates a thickness equivalent to the altered layer. By employing these methods, crystals with uniform crystal structure and thickness are obtained.

4.6 Previous Results

In this section, we briefly describe the results of the experiments that have been performed. The measurement of $b(Q)$ using pendellösung interferometry and $b(0)$ using neutron interferometer were performed at the Neutron Interferometry and Optics Facility (NIOFa) at NIST. Here, neutrons from
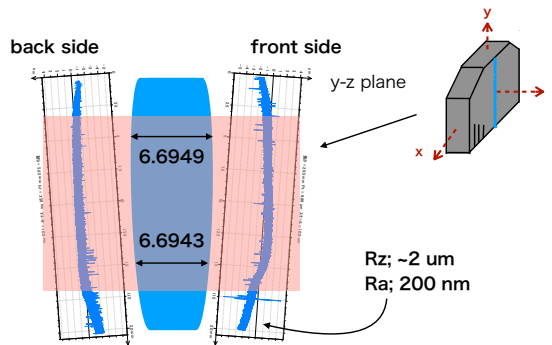
Figure 4.6: The overall shape of the crystal after processing.

the reactor neutron source are taken out to the experimental setup by diffraction from pyrolytic graphite (PG), making available neutrons at wavelengths of 2.2 Å and 4.4 Å. The neutrons enter the crystal sample after wavelength selection using a beryllium filter to improve the monochromaticity of the wavelengths. Two Cd slits were placed in front of the crystal and one after the crystal, which were used to shape the neutron beam. The interference fringes are obtained by rotating the crystal θ_P to change its effective thickness. The diffracted neutrons are detected by a ^{3}He detector and stored as data. Interferograms were measured for (111), (220), and (400) planes. The results of this experiment can be found in reference[116, 117]. The most noteworthy result of this research is the updated range of existence of the fifth force by up to two orders of magnitude. However, this search range is not far from the range of existence predicted by the new physics, and further search sensitivity improvement is needed. Increased search sensitivity is achieved by strongly constraining the momentum dependence of the averaged potential by increasing the number of crystal planes to be measured. However, the unknown systematic uncertainty of the term dependent on the atomic number of the crystal cannot be eliminated. To solve this problem, measurements using germanium crystals have been proposed. Since the atomic number of germanium is double that of silicon, the effect of the fifth force is also expected to be double. In fact, it is almost canceled out by the nuclear scattering length, but the sensitivity will be slightly improved. Since germanium has different crystal temperature factor and atomic structure factors than silicon, the unknown systematic uncertainty of these values can be estimated.

4.7 Calculation of Uncertainty

In this section, we describe the calculation of the range of existence of the fifth force, which is explored in experiments using germanium crystals. The measured value of the scattering length ratio is written by

$$\frac{b(Q)}{b(0)} = e^{-W}\left[1 - Z\frac{b_{\mathrm{ne}}}{b(0)}\right] + f_{\mathrm{e}}(Q)\frac{b_{ne}}{b(0)} + e^{-W}\frac{b_5(Q) - b_5(0)}{b(0)} \qquad (4.64)$$

where Q is the momentum transfer, W is Debye–Waller factor, Z is atomic number, f_{e} is atomic form factor, b_{ne} is electric scattering length. The left term is measured, and the right term is assigned the theoretical value. To estimate b_{ne} and B, the third term changes to 0, and to estimate the fifth force, the b_{ne} and B are assigned PDG average and previously measured value, respectively. From the Si measurement data, the relative uncertainties of measured scattering lengths can be estimated 5×10^{-5}

in each Q. Assuming that the statistical uncertainty estimated for the germanium measurement is the same as in the experiment with silicon, the estimated experimental values are

$$\frac{b(111)}{b(0)} = 0.987186 \pm 0.000050 \tag{4.65}$$

$$\frac{b(220)}{b(0)} = 0.966708 \pm 0.000067 \tag{4.66}$$

$$\frac{b(400)}{b(0)} = 0.934455 \pm 0.000088 \tag{4.67}$$

The other term for germanium is determined by the literature value. The temperature factor is

$$W(Q) = \frac{B}{16\pi^2} H^2 \tag{4.68}$$

$$B = 0.552 \pm 0.004 \text{ Å}^2 \tag{4.69}$$

from the reference[118], the forward scattering length is

$$b_{\text{Ge}}(0) = 8.185 \pm 0.020 \text{ fm} \tag{4.70}$$

from the reference[119], the lattice constant is

$$a = 5.657820 \pm 0.000009 \text{ Å} \tag{4.71}$$

from the reference[120], and the atomic form factors are

$$f_e(111) = 27.42 \pm 0.07 \tag{4.72}$$
$$f_e(220) = 23.35 \pm 0.11 \tag{4.73}$$
$$f_e(311) = 21.44 \pm 0.09 \tag{4.74}$$
$$f_e(400) = 19.40 \pm 0.07 \tag{4.75}$$

from the reference[121]. Note that the anharmonic term is ignored. The relative uncertainty of $b(Q)/b(0)$ is shown in figure 4.7. The total uncertainty (black line) is the convoluted theoretical uncertainty which is the total of atomic form factor (AAF), b_{coh}, b_{ne}, and temperature factor uncertainties. The measured uncertainty (red line) is estimated by the measurement data of Si which is 5.1×10^{-5} for (111), 6.9×10^{-5} for (220), and 9.4×10^{-5} for (400). This total and atomic form factor uncertainty between each lattice plane is interpolated linearly. The fifth force uncertainty (gray line) is calculated by the sum of measured uncertainty and total uncertainty using error propagation. The fifth force constraint is estimated using the right term of the uncertainty of Eq. (4.76). The constraint estimation can be obtained by assignment of measured value for $b(Q)/b(0)$, reference value for 2nd and 3rd term, respectively. This uncertainty is shown in Figure 4.7 in the gray line.

$$e^{-W} \frac{b_5(Q) - b_5(0)}{b(0)} = \delta \left[\frac{b(Q)}{b(0)} - e^{-W} \left(1 - Z \frac{b_{ne}}{b(0)} \right) - f_e(Q) \frac{b_{ne}}{b(0)} \right] \tag{4.76}$$

Note that the mean of δ is the uncertainty of the inside function.

4.8 Calculation of Exclusion Region of Fifth Force

The scattering length by the fifth force is written by

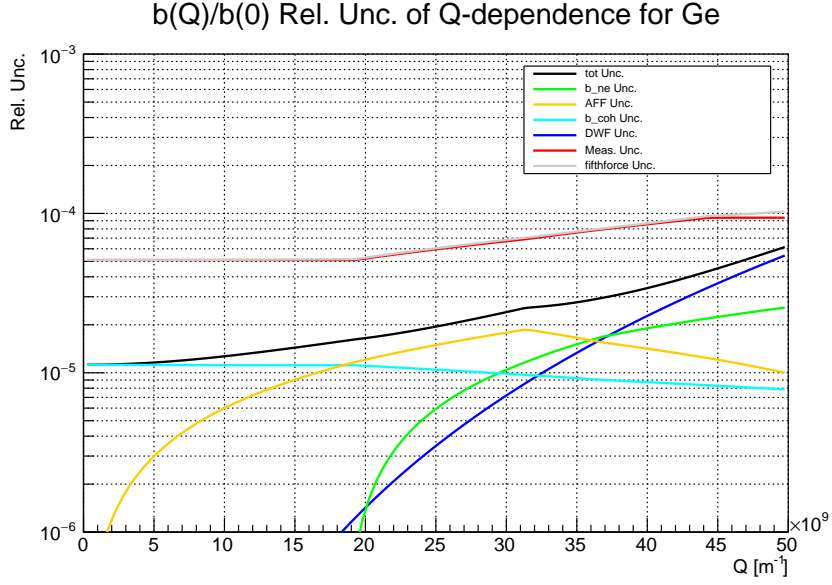$$b_5(Q) = \alpha_G \frac{2Gm^2M}{\hbar^2} \left(\frac{\lambda_5^2}{1 + Q^2\lambda_5^2} \right) \tag{4.77}$$

Figure 4.7: The relative uncertainty of Q-dependence.

where the α_{G} is the normalized parameter by the gravity, λ_5 is the effective interaction length of fifth force, m is neutron mass, the M is the nuclear mass, Q is the momentum transfer, and G is the gravitational force constant. In the case of using silicon, The b_5 can be calculated using $G = 6.67430 \times 10^{-11}$ m^{3}kg^{-1}s^{-2}, $m = 939.565413$ MeV/c^2, $M = 28.0855/N_A$ g, N_A is an Avogadro constant,

$$b_5(Q) = 1.57 \times 10^{-21} \ [\mathrm{m}^{-1}] \ \alpha_G \left(\frac{\lambda_5^2}{1 + Q^2\lambda_5^2} \right) \ \text{for Silicon} \tag{4.78}$$

In the case of Germanium, the M change to $M = 72.63/N_A$ g for germanium,

$$b_5(Q) = 4.06 \times 10^{-21} \ [\mathrm{m}^{-1}] \ \alpha_G \left(\frac{\lambda_5^2}{1 + Q^2\lambda_5^2} \right) \ \text{for Germanium} \tag{4.79}$$

From these, the fifth force constraint is calculated by

$$4.06 \times 10^{-21} \ [\mathrm{m}^{-1}] \ \frac{e^{-W}}{b(0)} \alpha_G \lambda_5^2 \left(\frac{Q^2\lambda_5^2}{1 + Q^2\lambda_5^2} \right)$$
$$= \delta \left[\left(\frac{b(Q)}{b(0)} \right)_{\mathrm{meas.}} - e^{-W} \left(1 - Z\frac{b_{\mathrm{ne}}}{b(0)} \right) - f_e(Q)\frac{b_{\mathrm{ne}}}{b(0)} \right] \tag{4.80}$$

Note that the right term is

$$\left(\frac{b(Q)}{b(0)} \right)_{\mathrm{meas.}} = e^{-W} \left(1 - Z\frac{b_{\mathrm{ne}}}{b(0)} \right) + f_e(Q)\frac{b_{\mathrm{ne}}}{b(0)} \tag{4.81}$$

because the $b(Q)/b(0)$ is calculated using the theoretical value which is not measured in the Ge case yet. The e^{-W} and $b(0)$ have an uncertainty, so these factors are moved to the right term to simplify the calculation.

$$\alpha_G \lambda_5^2 \left(\frac{Q^2 \lambda_5^2}{1 + Q^2 \lambda_5^2} \right)$$
$$= \delta \left[\left(\left(\frac{b(Q)}{b(0)} \right)_{\text{meas.}} - e^{-W} \left(1 - Z \frac{b_{\text{ne}}}{b(0)} \right) - f_e(Q) \frac{b_{\text{ne}}}{b(0)} \right) \frac{b(0)e^W}{4.06 \times 10^{-21} \ [\text{m}^{-1}]} \right] \quad (4.82)$$

The α_G and λ_5 are estimated using this equation (4.82). To explain easier, we call each term

$$f_1(Q) = \alpha_G \lambda_5^2 \left(\frac{Q^2 \lambda_5^2}{1 + Q^2 \lambda_5^2} \right) \quad (4.83)$$

$$f_2(Q) = \left(\left(\frac{b(Q)}{b(0)} \right)_{\text{meas.}} - e^{-W'} \left(1 - Z \frac{b_{\text{ne}}}{b(0)} \right) - f_e(Q) \frac{b_{\text{ne}}}{b(0)} \right) \frac{b(0)e^W}{4.06 \times 10^{-21} \ [\text{m}^{-1}]} \quad (4.84)$$

The Eq. (4.84) equal to zero is to perform a simple calculation. The estimated fifth force constraint will be the minimum estimation. In the case of silicon, the experimental values are given and are not strictly zero.

The χ^2 is calculated using

$$\chi^2(\alpha_G, \lambda_5) = \sum_Q \left(\frac{f_1(Q, \alpha_G, \lambda_5) - f_2(Q)}{\delta \left[f_2(Q) \right]} \right)^2. \quad (4.85)$$

Since the calculated χ^2 means the probability of the existence of the Fifth Force, the point where the upper-side dominance probability is 5% becomes the 95% confidence level. The critical values for the χ^2 test are 7.815 for a degree of freedom of 3 and 12.59 for a degree of freedom of 6. The calculated constraints of α_G and λ_5 using Si and Ge data are shown in Figure 4.8. It can be seen
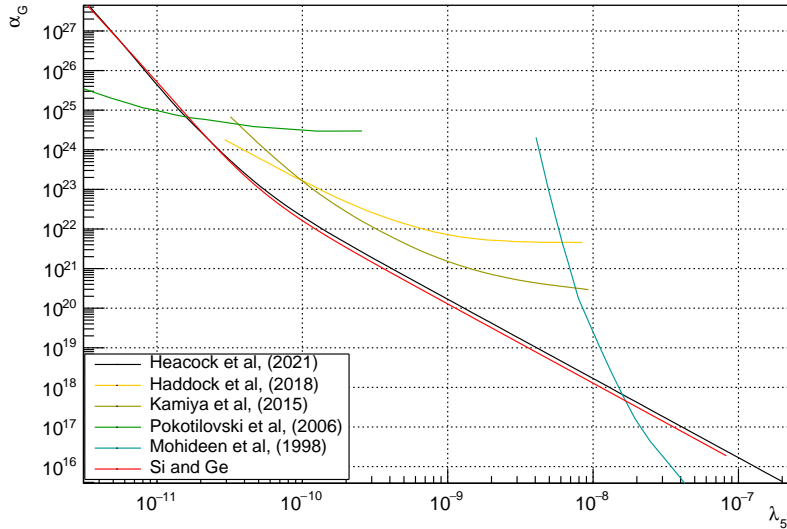

Figure 4.8: The exclusion map of fifth force constraint with the data of Ge and Si.

that the exclusion zone does not change significantly from the measurements with silicon. The ratio of the area excluded by the measurement with silicon to the area excluded by the additional germanium measurement is shown in the Figure 4.9. From these, the constraint with Ge measurement is a factor
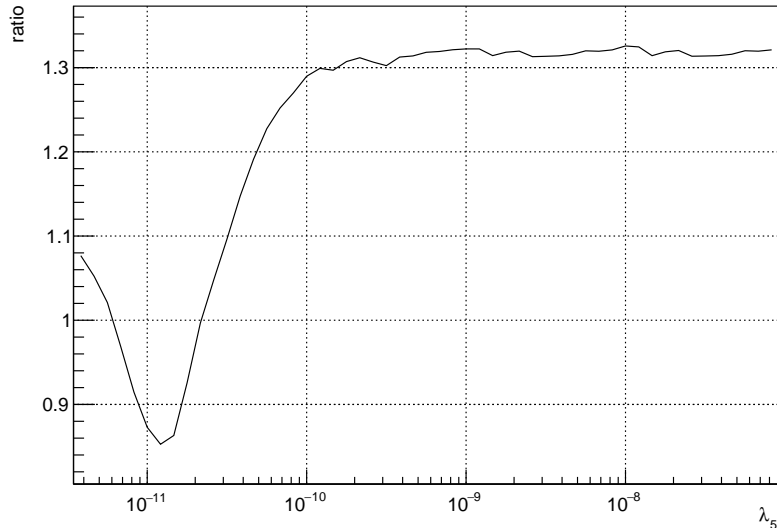
Figure 4.9: The improvement ratio of Si only and Si & Ge constraints.

of 1.3 at minimum.

In order to improve the search range of experiments using germanium, it is necessary to improve the precision of the determination of each physical quantity used. From Figure 4.7, it can be seen that precise measurements of the atomic structure factor and crystal temperature factor are necessary. However, since these values are obtained in separate experiments, the determination accuracy cannot be easily improved. Therefore, we conclude that the first step is to strengthen the momentum dependence of the phase shift by measuring pendellösung fringes on multiple crystal planes.

4.9   Conclusions

The global search for the fifth force is a pursuit rooted in predictions from new physics beyond the Standard Model of elementary particles. The pendellösung interference method, employed in measuring interference fringes, offers the world's highest sensitivity for probing the fifth force. Experiments using silicon single crystal with ultra-high precision machining have succeeded in enhancing the exploration range by up to two orders of magnitude compared to previous research. Despite this progress, the achieved range falls considerably short of the predicted existence range posited by new physics. To address this, we considered enhancing search sensitivity through the use of germanium. The calculated search range for germanium was approximately 1.3 times larger than that for silicon. To further improve the search range, enhancing the precision of determining the crystal temperature factor and the atomic structure factor is crucial. However, as both factors are derived from other experiments, improving their determination accuracy is not a straightforward task. From these, we assert that the initial step towards enhancing search sensitivity is to tightly constrain the momentum shift dependence of the phase shift using multiple crystal planes. This process can give important results for neutron-electric scattering length and temperature factors[117]. The experiment is being conducted at NIST, where beam access has been halted for several years to facilitate beam line updates and reactor accidents. Throughout this period, discussions will focus on strategies to enhance the accuracy of various physical quantities.

The most important achievement was the reduction of systematic uncertainty by applying ultra-precision processing to the single-crystal samples used in the experiments. In conventional kinetic diffraction experiments, interference fringes that precisely reflect the potential inside the crystal can be observed, but it has been difficult to precisely extract the values due to uncertainty in the crystal thickness. By using ultra-precision machining, the uncertainty derived from the sample geometry accuracy was reduced. This result shows that it is possible to advance the neutron optics by improving the component shape accuracy.

Chapter 5

Demonstration of Improved Component Installation Accuracy: Development of Neutron Interferometers Using Multilayer Mirrors

Neutron interferometers, characterized by a neutron wave that is divided into two paths and then merged while sustaining its coherence[122], are employed for the precise quantification of interactions involving neutrons[123]. In particular, the Mach–Zehnder type neutron interferometer, utilizing diffraction of Si single crystal and first demonstrated by Rauch in 1974[50], has found broad application in various physics experiments. These range from neutron-nuclear scattering length measurements[124, 125, 126], demonstrations of classical physics with elementary particles[19, 127], validations of quantum mechanics[25, 128, 129, 130, 131, 27], to explorations of exotic interactions expected by new physics[132, 14]. More recently, a proliferation of proposed experiments using neutron interferometers to investigate new physics highlights their undiminished significance[24, 133, 134, 44, 135, 22].

The sensitivity of the measured interactions is proportionally linked to the neutron wavelength and the interaction length. However, neutron interferometers using Si crystal are restricted by the lattice constant in terms of available neutron wavelengths and also constrained in size by the dimensions of the ingot[122]. There is ongoing advancement in the development of neutron interferometers capable of high-sensitivity measurements to overcome these limitations[136, 137, 138]. Among them, Jamin-type neutron interferometers using neutron mirrors function by reflecting neutrons via an artificially fabricated multilayer structure that separates and recombines neutron paths[139, 140, 141]. This multilayer configuration permits the selection of neutron wavelengths based on specific design parameters[91]. However, since multilayer mirrors need to be installed with an accuracy of about 30 nm, which is the coherent length, they have not been put into practical use until now.

I have developed a novel neutron interferometer, synergistically integrating unpolarized neutron mirrors with a pulsed neutron source capable of identifying the wavelength from the time of flight (TOF) at J-PARC. The multilayer mirrors were installed to meet the required accuracy using etalon substrates and autocollimators used in laser optics. This interferometer possesses the capability to simultaneously measure phase shifts at varying wavelengths, offering a notable statistical advantage. Moreover, it facilitates the tracking and compensation of time-varying disturbances lasting longer than

the pulse interval[142]. These features overcome the problems of conventional ones using multilayer mirrors. In a demonstrable feat, we have executed measurements of the neutron-nuclear scattering lengths for an array of nuclei. This chapter outlines the principle of our interferometer and the experiment result.

5.1 The Quantum Phase Shift of Matter Waves

This seciton examines the fundamental operation of a typical neutron interferometer. The quantum phase of the neutron interferometer is described as a wave that evolves in both space and time following the Feynman-Dirac path integral along a trajectory defined by classical mechanics. The phase, denoted as $\phi(x,t)$, of the wave function $\Psi(x,t)$ should be considered a scalar field that spreads throughout the entire apparatus, specifically a neutron interferometer. This apparatus includes various components such as the slits, phase-shifting interactions, and detectors. The neutron interferometer has a geometric resemblance to the classical optics Mach–Zehnder interferometer and possesses a topological equivalence to a ring, as depicted in Figure 5.1. At a designated point A on the ring, an initial wave Ψ_0 is introduced into the ring and then coherently split into two components: one travels clockwise on path I, while the other moves counterclockwise on path II around the ring. Following interactions with a potential $V(x', v', t')$ that relies on the position x' along the trajectories, the time t', and sometimes the neutron's velocity v', these two waves merge and interfere within a confined region of space near point B. This interference results in the creation of an exit beam, which is a combined form of the two wave functions I and II that have traversed the respective paths. Notably, the differences in phase serve as the sole measurable quantities. This situation is akin to the aspects of position, momentum, angular momentum, or time measurements in classical and quantum mechanics, where only relative observables can be measured, always in relation to a reference system.
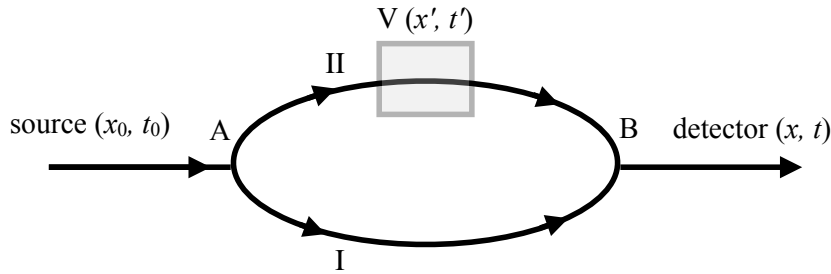

Figure 5.1: General scheme of the interferometer experiment.

The phase accumulated on either path is a line integral over the Lagrangian $\mathcal{L}$ in space-time given by

$$\phi(x,t) = \frac{1}{\hbar} \int \mathcal{L} \, dt'$$
(5.1)

The Lagrangian $\mathcal{L}$ is related to the Hamiltonian $\mathcal{H}$ by a Legendre transformation

$$\mathcal{L} = \mathbf{p} \cdot \mathbf{v} - \mathcal{H}$$
(5.2)

where p is the canonical momentum of the neutron and v is the group velocity. Thus, Eq. (5.1) gives the phase at the detector at position x as a function of time t, namely

$$\phi(\mathbf{x},t) = \frac{1}{\hbar} \int_{x_0}^{x} \mathbf{p} \cdot \, d\mathbf{s} - \frac{1}{\hbar} \int_{t_0}^{t} \mathbf{\Psi} \, dt' = \int_{x_0}^{x} \mathbf{k} \cdot \, d\mathbf{s} - \int_{t_0}^{t} \omega \, dt'$$
(5.3)

where the wave vector $k = 2\pi/\lambda$ corresponding to the de Broglie wavelength λ, and ω is the frequency related to the total energy of the wave at any point (x', t') along the trajectories. We must evaluate the line integrals in Eq. (5.3) along each of the paths in Figure 5.1, namely

$$\phi_\mathrm{I}(x,t) = \frac{1}{\hbar} \int_{x_0}^{x} \mathbf{p}_\mathrm{I} \cdot d\mathbf{s} - \frac{1}{\hbar} \int_{t_0}^{t} \mathcal{H}_\mathrm{I} dt' \tag{5.4}$$

and

$$\phi_\mathrm{II}(x,t) = \frac{1}{\hbar} \int_{x_0}^{x} \mathbf{p}_\mathrm{II} \cdot d\mathbf{s} - \frac{1}{\hbar} \int_{t_0}^{t} \mathcal{H}_\mathrm{II} dt' \tag{5.5}$$

Thus, the last terms cancel due to energy conservation and the phase difference for the waves traversing the two paths is

$$\Delta\phi(x,t) = \phi_\mathrm{II}(x,t) - \phi_\mathrm{I}(x,t) = \frac{1}{\hbar} \int p_\mathrm{II} \cdot ds - \frac{1}{\hbar} \int p_\mathrm{I} \cdot ds \tag{5.6}$$

which is a path integral around the ring in Figure 5.1. In neutron interferometry, it is the phase shift delta $V(x,t)$ caused by the potential V that is of physical interest. This potential-dependent phase shift is a line integral along the classical trajectory of the neutron. The stationary phase shift is represented by a potential $V(x)$ that changes momentum due to energy conservation:

$$\frac{(p - \delta p)^2}{2m} + V(x) = E \rightarrow v\delta p \approx -V(x) \tag{5.7}$$

and

$$\Delta\phi = \frac{1}{\hbar} \oint \delta p \ ds = -\frac{1}{\hbar} \oint V(x) \ dt \tag{5.8}$$

This is the basic equation for most interferometer measurements.

The canonical momentum p must be used in evaluating this potential-dependent phase shift to account for gauge invariant potentials. In general, it consists of two parts

$$p = p_\mathrm{kinetic} + p_\mathrm{hidden} \tag{5.9}$$

Considering the case where the potential depends only on position and not on time t or velocity v, the neutron's total energy E is a constant of the motion. The force is said to be conservative, and the neutron decelerates when entering the region R where V is non-zero and accelerates when leaving R (and vice versa when the sign of the potential changes). There is no hidden momentum in this case, and the phase shift depends only upon the action of the kinetic momentum.

$$\Delta\phi = \frac{1}{\hbar} \int_R \Delta p_\mathrm{kinetic} \ ds \tag{5.10}$$

where the kinetic momentum is given by the product of the neutron's mass and velocity v,

$$p_\mathrm{kinetic} = mv \tag{5.11}$$

and the phase shift can be written as

$$\Delta\phi = \frac{2\pi}{\lambda} \int \Delta L \ dx \tag{5.12}$$

where the ΔL represents the optical length difference between two paths considered refraction. When the potential difference between the two paths is ΔV, the resulting phase shifts can be written as follows:

$$\Delta\phi = \frac{2\pi m_\mathrm{n} \lambda L}{\hbar^2} \Delta V \tag{5.13}$$

where the L is the interaction length. When ΔV is constant, the observed phase shift is proportional to the neutron wavelength λ and interaction length L. For a more detailed description, see Ref[122].

In the case of zero-force situations when $\mathcal{H}$ is independent of time, the phase shift $\Delta\phi$ may depend explicitly upon the geometry and topology. The hidden part of the momentum arises in situations where the potential is velocity-dependent. In the Aharonov–Casher (AC) effect experiment, the velocity-dependent potential comes from the spin-orbit coupling of the neutron's motion to the electric field generated by a line of charge. In the Sagnac effect experiments, the hidden momentum depends on the state of rotation of the frame of the interferometer, that is, its frequency of angular rotation.

5.2   Conventional Neutron Interferometers

Neutron interferometers constructed using silicon single crystals stand as the most commonly employed apparatus in contemporary physics experiments. The inception of the silicon crystal neutron interferometer draws inspiration from X-ray interferometers and was initially demonstrated by Rauch et al. in 1974. The silicon crystal neutron interferometer is composed of multiple blades designed to uphold a single-crystal structure, as illustrated in Figure 5.2. Within each blade, neutrons undergo separation into two distinct paths through Laue diffraction, subsequently recombining once more. These blades, extracted from a unified ingot, possess crystal planes that naturally align, ensuring precise control over the motion of neutron waves within the coherence length.
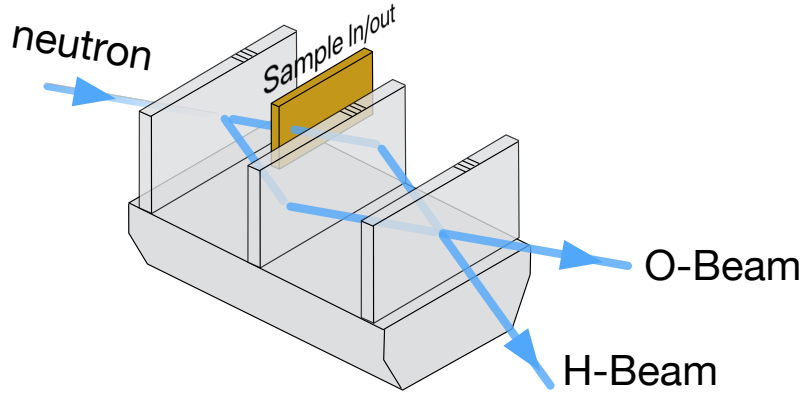

Figure 5.2: The sketch of conventional neutron interferometer using silicon single crystal.

A silicon crystal interferometer follows the Mach–Zehnder model and incorporates four components responsible for wave reflection. According to symmetry considerations, the amplitude and phase of the resultant forward (O-beam) wave function behind the interferometer comprises equal contributions derived from both beams, traversing paths I and II. The wave traveling along the path I experiences transmission (t) at the first crystal, followed by two consecutive reflections (r) at the second and third crystals, ultimately arriving at the detector as the O-beam. Conversely, the wave on path II undergoes reflection-reflection-transmission (rrt) and can be identified as an H-beam. Symmetry analysis reveals that these two waves exhibit identical phase and amplitude. However, differences in phase (denoted as ϕ_1 and ϕ_2) emerge when neutrons encounter distinct interactions along the two beam paths. Therefore, the intensity of the O-beam is given by

$$I_{\mathrm{O}} = |\psi_{\mathrm{I}} + \psi_{\mathrm{II}}|^2 = \left| \mathrm{ttr}\ \psi_0 e^{i\phi_1} + \mathrm{rrt}\ \psi_0 e^{i\phi_2} \right|^2, \tag{5.14}$$

where the psi_0 is the wave function of incident neutrons. Setting $\Delta\phi = \phi_2 - \phi_1$ to be the phase difference, one sees that the intensity pattern for the O-beam interferogram displays complete modulation in this ideal case:

$$I_O(\Delta\phi) = A\left[1 + \cos\Delta\phi\right] \tag{5.15}$$

By similar reasoning, one finds that the intensity in the H-beam is

$$I_H(\Delta\phi) = \left|\text{trt } \psi_0 e^{i\phi_1} + \text{rrr } \psi_0 e^{i\phi_2}\right|^2 = B - A\cos\Delta\phi \tag{5.16}$$

The minus sign in front of the cosine term arises because there is an odd number of reflections (r), for each component contributing to I_H. From particle conservation, it also follows that

$$I_O + I_H = \text{constant.} \tag{5.17}$$

The total intensity of the O-beam and the H-beam remains constant, as is expected due to silicon's near-zero absorption of thermal neutrons. Consequently, the neutron intensity alternates between the O-beam and the H-beam detectors as the phase difference $\Delta\phi$ is adjusted. However, due to the various imperfections present in the interferometer, intensity oscillations are expected to be somewhat damped compared to the ideal expected behavior.

Silicon interferometers have been widely used in physics experiments since their first demonstration in 1974. In the past, they've been employed to measure neutron nuclear scattering length, confirm quantum mechanics, investigate gravitational interactions, and explore unknown phenomena such as chameleon fields. Recently, there has been a surge in proposing neutron interferometry for various new physics investigations due to its highly sensitive measurement capabilities. This includes studies on breaking Lorentz symmetry and endeavors to detect primordial gravitational waves. While these studies are crucial for enhancing our understanding of current physical phenomena, it is imperative to conduct these experiments with utmost precision. There's a growing expectation for further enhancements in the sensitivity of neutron interferometers from various avenues.

The measurement sensitivity of a neutron interferometer is proportional to the neutron wavelength and interaction length from Eq. (5.13). However, silicon interferometers are composed of silicon crystals made from ingots, so the available neutron wavelength is limited by the lattice constant and the interaction length is limited by the size of the ingot. In addition, interferometers are sensitive to noise and require large vibration isolators and temperature control mechanisms. To solve this problem, several interferometers are in the development stage. Split interferometers, which split existing silicon interferometers in two, allow for increased interaction length[138]. Spin-echo interferometers and Talbot-Lau interferometers have been implemented to enhance measurement accuracy by boosting statistical data. Despite their practical application, their ability to measure a wide range of physical phenomena is restricted due to the absence of achieving a two-path separation. Therefore, the need for a neutron interferometer that can achieve high-sensitivity measurement with a two-path separation is crucial and anticipated across various fields.

The neutron interferometer using neutron mirrors was demonstrated by Funahashi in 1996[139]. Neutron mirrors can utilize neutrons of longer wavelengths that cannot be reflected by silicon crystals, thus improving the sensitivity of the measurement. In this mirror interferometer, two layers of neutron mirrors and a gap layer were deposited on a silicon wafer. Subsequently, an interferometer with an air gap was demonstrated by Kitaguchi by using an etalon substrate[143]. By enlarging the air gap of the etalon substrate, an interferometer in which the two paths are completely separated was realized by Seki[141]. A conceptual diagram of the mirror interferometer developed so far is shown in Figure 5.3. These developed interferometers have successfully observed the interference of long-wavelength neutrons. On the other hand, the distance between the two separated paths is as short as 300 μm, so the auxiliary phase shifter used in the silicon interferometer cannot be used. Therefore, the interference fringes are observed according to the same principle as in spin-echo interferometry using

polarized neutrons. In addition, it was difficult to measure interference fringes stably due to statistical problems, so measurement of the interaction by sample insertion was not realized. A combination of the interferometer using the multilayer mirror and a pulsed neutron source has been proposed to solve the statistics problem and achieve stable measurements. In 2021, interferometers with multilayer mirrors were successfully operated at the pulsed neutron source[142]. The results show that short-time measurements were achieved and that disturbances can be removed from the phase shifts obtained. However, this has not yet departed from the measurement of interference fringes based on the spin-echo principle.
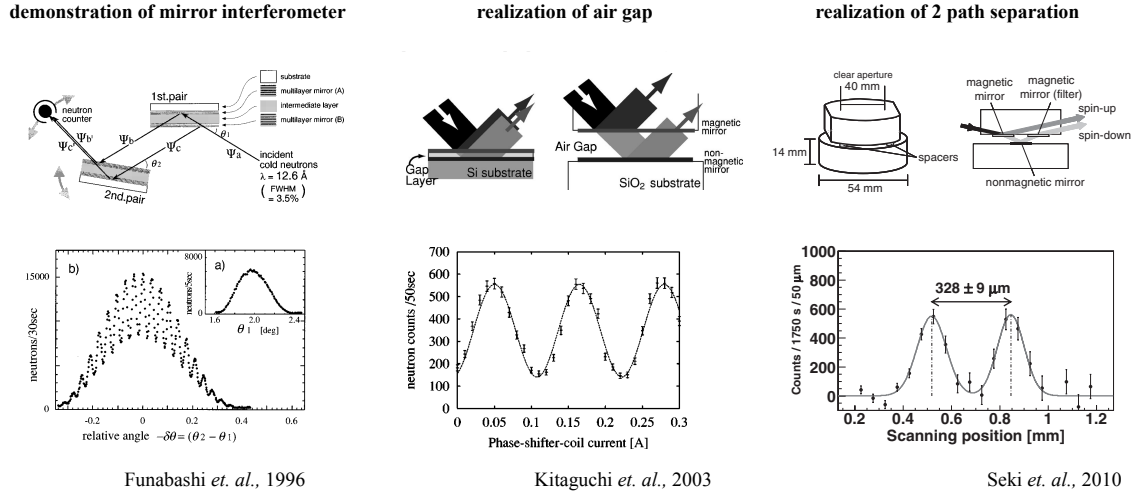
Figure 5.3: History of neutron interferometer using multilayer mirrors.

5.3 Theoretical Phase Shifts

The phase shift that can be measured using a neutron interferometer depends on the neutron wavelength, and thus, the interferograms that can be observed are wavelength-dependent. In this section, the wavelength dependence of the phase shift obtained is explained. Consider the case where the neutron mirror is a component deposited on a glass substrate In this figure, the D represents the air gap of glass substrate, θ is the incident angle of neutrons, θ' and θ'' is the incident angle for each mirror considered with refraction, and n is the refraction index of glass. For reference, a typical value for these variables is $D = 200$ μm and $\theta = 1$ degree. Incident neutrons are separated into two paths due to the effect of refraction by the glass substrate and reflection by the mirror. The phase shift is determined by the optical path length, which is defined by the geometric configuration since it is given by the line integral of the momentum of the neutrons separated into two paths from the Eq. (5.8).

It is assumed that the two glass substrates are parallel, and the sides and bottom of the glass substrate are vertical. The optical lengths L of path I (B→E) and path II (B→C→D→F→G) can be expressed as follows:

$$L_{\mathrm{I}} = \frac{nl_1}{\cos\theta'}, \tag{5.18}$$

$$L_{\mathrm{II}} = \frac{2D}{\sin\theta''} + \frac{n(l_1 - l_2)}{\cos\theta'} + (l_1 \tan\theta' - (l_1 - l_2)\tan\theta')\sin\theta. \tag{5.19}$$
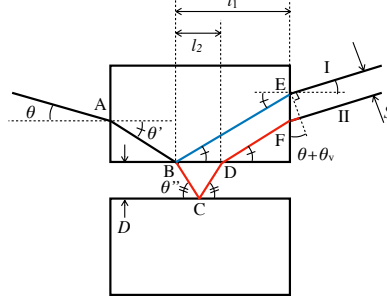
Figure 5.4: Characteristics of the 1st beam splitting components. The neutron beam incidents from left to right.

The refraction index n can be written as

$$
\begin{aligned}
n &= \sqrt{1 - \frac{U}{E_n}} \\
&\simeq 1 - \frac{\lambda^2 N b_{\mathrm{c}}}{2\pi} \\
&= 1 - \frac{mU\lambda^2}{h^2},
\end{aligned}
\tag{5.20}
$$

where U is the Fermi pesudopotential, E_{n} is the neutron energy, N is the atomic density, b_{c} is the neutron-nuclear scattering length, m is the neutron mass, and h is the Plank constant. Note that the absorption was neglected. The relationship between the refraction angle can be expressed using Snell's law with refraction index n as follows:

$$
\begin{aligned}
\sin\theta &= n\sin\theta', \\
n\cos\theta' &= \cos\theta''.
\end{aligned}
\tag{5.21}
\tag{5.22}
$$

From the geometric conditions, the following equations hold:

$$
\begin{aligned}
1 - \sin^2\theta'' &= n^2\left(1 - \sin^2\theta'\right) = n^2 - \sin^2\theta, &(5.23)\\
\sin^2\theta'' &= \left(1 - n^2\right) + \sin^2\theta, &(5.24)\\
\frac{\tan\theta'}{\tan\theta''} &= \frac{\sin\theta}{\sin\theta''}. &(5.25)
\end{aligned}
$$

Using Eqs. (5.21)–(5.25), the Eq. (5.19) is written as

$$
L_{\mathrm{II}} = \frac{2D}{\sin\theta''} + \frac{nl_1}{\cos\theta'} - \frac{2n^2 D}{\sin\theta''} + 2D\frac{\tan\theta'}{\tan\theta''}\sin\theta.
\tag{5.26}
$$

Consequently, the optical path difference at the 1st glass substlate can be described as

$$
\begin{aligned}
\Delta L_{\mathrm{1st}} &= L_{\mathrm{II}} - L_{\mathrm{I}} \\
&= 2D\sqrt{\left(1 - n^2\right) + \sin^2\theta} \\
&= 2D\sqrt{1 - n^2 + \sin^2\theta}.
\end{aligned}
\tag{5.27}
$$

By defining the normalized refraction index δn as

$$\delta n = 1 - n \simeq \frac{mU\lambda^2}{h^2}, \tag{5.28}$$

the Eq. (5.27) can be written using $n^2 \simeq 1 - 2\delta n$, and applying an approximation of $\delta n / \sin^2 \theta \ll 1$; then

$$\begin{aligned}\Delta L_{1st} &\simeq 2D\sqrt{\sin^2\theta + 2\delta n} \\ &\simeq 2D\sin\theta\left(1 + \frac{\delta n}{\sin^2\theta}\right).\end{aligned} \tag{5.29}$$

Since the path difference for the 2nd splitting component is the same as for the 1st splitting component, the overall path difference in the interferometer is written as

$$\begin{aligned}\Delta L &= \Delta L_{2nd} - \Delta L_{1st} \\ &\simeq 2D\left[\sin\theta_2\left(1 + \frac{\delta n}{\sin^2\theta_2}\right) - \sin\theta_1\left(1 + \frac{\delta n}{\sin^2\theta_1}\right)\right],\end{aligned} \tag{5.30}$$

where the θ_1 is the incident angle for the 1st component, θ_2 is the incident angle for the 2nd component. The air gaps of the two components were assumed to be the same. By denoting $\theta_2 = \theta_1 + \delta\theta$, $\theta_1 = \theta$, and assuming $\sin\theta \simeq \theta$, Eq. (5.30) can be written as

$$\Delta L \simeq 2D\delta\theta\left(1 - \frac{\delta n}{\theta^2}\right). \tag{5.31}$$

The phase shifts due to the path difference are

$$\Delta\phi = \frac{2\pi}{\lambda}\Delta L. \tag{5.32}$$

From these, the phase shifts obtained in this experiment can be written as

$$\Delta\phi \simeq 2\pi\frac{2D\delta\theta}{\lambda}\left(1 - \frac{\delta n}{\theta^2}\right), \tag{5.33}$$

which can be written using Eq. (5.28) as:

$$\Delta\phi \simeq \frac{4\pi D\delta\theta}{\lambda} - \frac{4\pi D\delta\theta mU}{h^2\theta^2}\lambda. \tag{5.34}$$

Finally, the phase shift resulting from the difference in the optical path can be expressed using two terms. One term is inversely proportional to the wavelength, while the other term is directly proportional to the wavelength. Since the phase shift obtained by inserting a potential V in one path is described by Eq (5.13), the observed phase shift is written as

$$\Delta\phi = \frac{4\pi D\delta\theta}{\lambda} - \frac{4\pi D\delta\theta mU}{h^2\theta^2}\lambda + \frac{2\pi m_n L\Delta V}{\hbar^2}\lambda. \tag{5.35}$$

Since each term in the phase shift depends on wavelength, the interference fringes are wavelength-dependent. The phase shift due to the sample has the same dimension as the second term of the phase shift due to the geometric distance.

5.4   Calculation of Phase Shifts

In the previous section, we showed that the phase shift can be described by two terms, one proportional and one inversely proportional to wavelength. The phase shift due to the inserted sample is determined by measuring the phase shift with and without the sample, with the geometrically determined phase shift fixed. This eliminates the accuracy of the geometric phase shift approximation from the phase shift due to the inserted sample. On the other hand, in the development of an interferometer, it is important to compare the measured and theoretical values of the phase shift in order to evaluate the accuracy of its design. Here, the function is evaluated by comparing the expression for the phase shift using the approximation with the expression before the approximation, and by varying each parameter.

The geometric phase shift is expressed by the following equation:

$$\Delta\phi \quad = \quad \frac{2\pi}{\lambda}\left[2D\sqrt{1-n^2+\sin^2\theta_2} - 2D\sqrt{1-n^2+\sin^2\theta_1}\right] \tag{5.36}$$

$$\simeq \quad \frac{4\pi D\delta\theta}{\lambda} - \frac{4\pi D\delta\theta mU}{h^2\theta^2}\lambda \tag{5.37}$$

where

$$\delta\theta = \theta_2 - \theta_1. \tag{5.38}$$

The wavelength dependence of phase shift before and after the approximation, obtained using the conditions used in the experiment, is shown in Figure 5.5, where the experimental parameter is $D = 189$ μm, $\theta = 1.05$ deg, and $U_F = 90.5$ neV for SiO_2. Since the wavelength range used in the experiment is 0.8–1.1 nm, the phase shift in the post-approximation Eq.(5.37) is smaller than that in the pre-approximation Eq. (5.36) by about 5%.
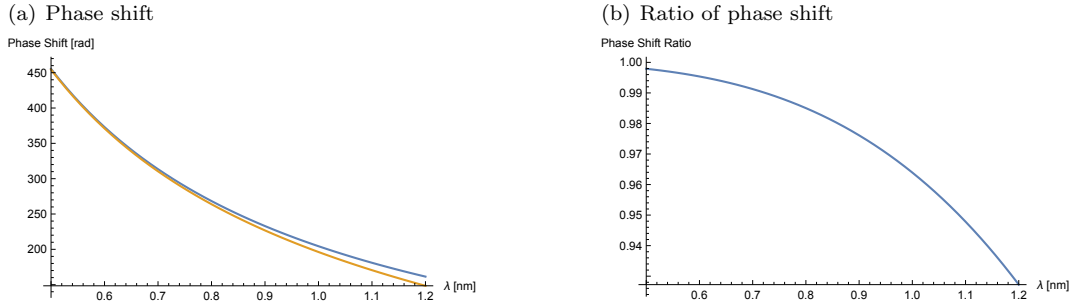

Figure 5.5: (a) Wavelength dependence of phase shift before (blue) and after (orange) the approximation. (b) Wavelength dependence of the ratio of phase shift before and after approximation.

Next, consider the case where the glass substrate injection plane is not perpendicular to the mirror plane. When the mirror and ejection surfaces of the glass substrate are not perpendicular, that is, when $\theta_V \neq 0$ in Figure 5.4, the path difference in the first glass substrate can be written as follows

$$\Delta L' = 2D\frac{\tan\theta'}{\tan\theta''}\cos\theta\sin\theta_v = S\sin\theta_v \tag{5.39}$$

where the S represents the 2 path difference, shown in Figure 5.4, which is written as

$$\Delta\phi' = \frac{2\pi}{\lambda}\left[2D\sqrt{1-n^2+\sin^2\theta_2} - 2D\sqrt{1-n^2+\sin^2\theta_1} + S\sin\theta_{v2} - S\sin\theta_{v1}\right]. \tag{5.40}$$

Here, the θ_{v1} and θ_{v2} represent the angular difference of injection surface. For simplify, the angular difference of injection surface is replaced by $\delta\theta_v = \theta_{v2} - \theta_{v1}$. The phase shift depending on the $\delta\theta_v$ and $\delta\theta$ is shown is Figure 5.6. The angler difference $\delta\theta_V$ has the same effect on the observed phase shift as $\delta\theta$. Therefore, it is important to note that the $\delta\theta$ dependence of the phase shift is influenced by the offset in the angular difference of the injection plane.
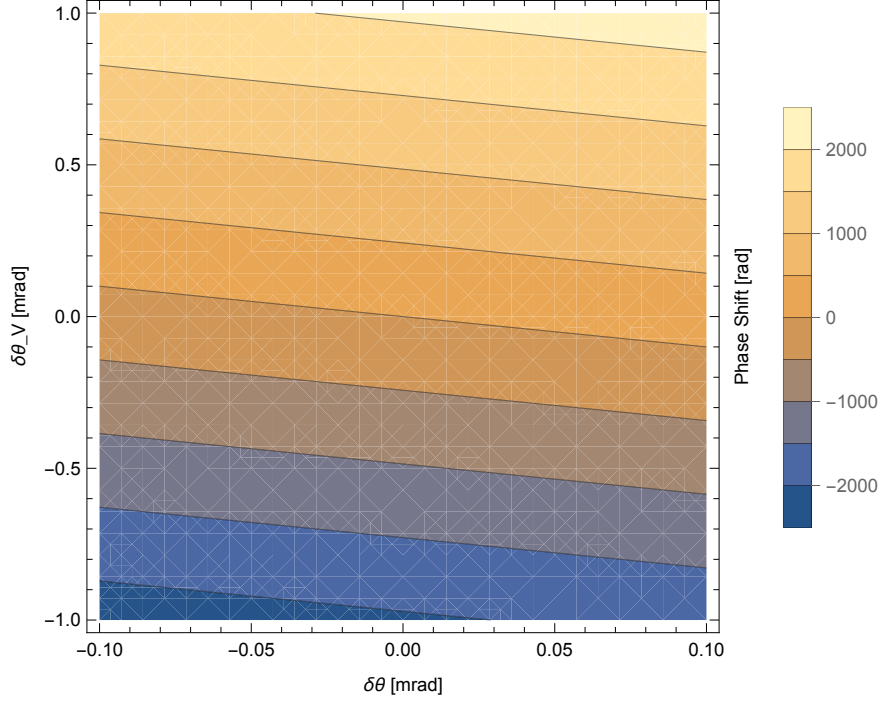
Figure 5.6: The calculated phase shift depending the $\delta\theta$ and $\delta\theta_V$ at $\lambda = 1$ nm

Next, consider the case where the gap spacing of the two opposite mirror is different. When the air gap spacing of the 1st opposite mirror is $D_1 = D$ and that of the 2nd opposite mirror is D_2, we put the difference between them as $\Delta D = D_2 - D_1$. The resulting phase shift can be written as follows from (5.36):

$$\Delta\phi'' = \frac{2\pi}{\lambda}\left[2D_2\sqrt{1 - n^2 + \sin^2\theta_2} - 2D_1\sqrt{1 - n^2 + \sin^2\theta_1}\right] \tag{5.41}$$

$$= \frac{2\pi}{\lambda}\left[2D\sqrt{1 - n^2 + \sin^2\theta_2} - 2D\sqrt{1 - n^2 + \sin^2\theta_1}\right]$$

$$+ \frac{2\pi}{\lambda}\left[2\Delta D\sqrt{1 - n^2 + \sin^2\theta_2}\right] \tag{5.42}$$

The phase shift obtained from this is shown in Figure 5.7. It can be seen that when the gap spacing between the two opposite mirrors changes by a few micrometers, it is observed as a phase shift offset. The point $\delta\theta = 0$ in the experiment must account for this air gap difference. It is important to recognize that this value remains constant during the experiment and does not impact the measurement of the phase shift. However, it does introduce an offset to the $\delta\theta$ dependence of the phase shift.
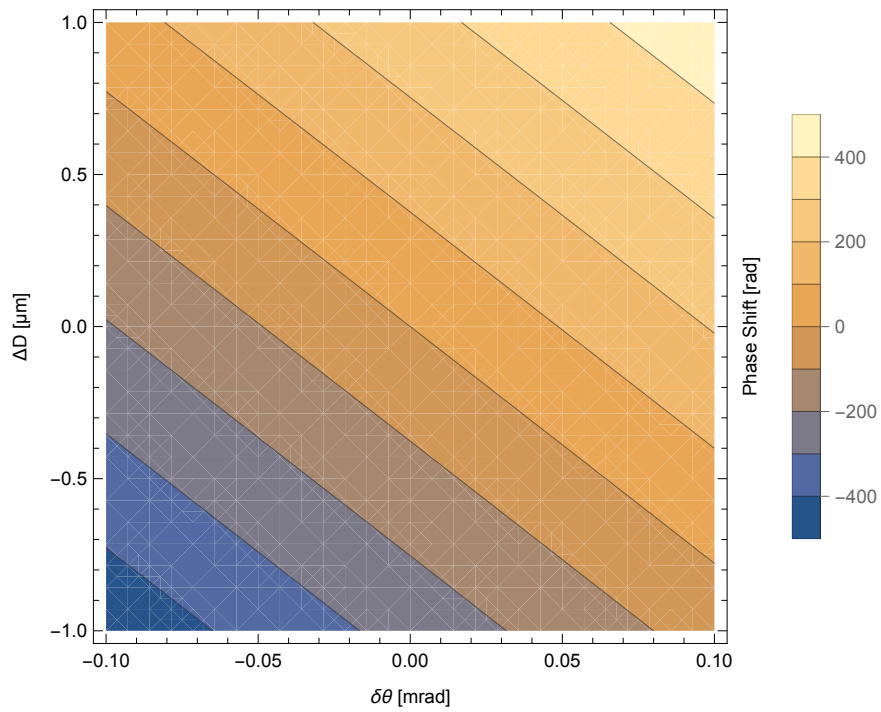
Figure 5.7: The calculated phase shift depending the $\delta\theta$ and ΔD at $\lambda = 1$ nm

5.5 Accuracy Requirement for Mirrors

The interferometric properties of neutrons are influenced by their coherent length, as detailed in Section 1.2.2. In this section, the installation accuracy of the four mirrors composing the interferometer is derived from the coherent length. At the beamline where the experiment is conducted, several factors determine the coherence length in different directions. Along the beam axis, the longitudinal coherence length L_L^c is dictated by the wavelength resolution. The transverse coherence length for the horizontal direction L_H^c is determined by the guide bench installed in the beamline. The transverse coherence length for the vertical direction L_V^c is determined by the slit collimation. In this experiment configuration, since the largest wave vector is $k = 8.05$ nm^{-1}, the distribution of momentum transfer for the longitudinal direction is $\sigma_L = 0.0435$ nm^{-1}, for the horizontal direction is $\sigma_H = 0.000725$ nm^{-1} and for the vertical direction is $\sigma_V = 0.042$ nm^{-1}. Using these values and Eq. (1.20), we obtain $L_L^c = 32.5$ nm, $L_H^c = 2.0$ μm, and $L_V^c = 33.8$ nm. This value indicates that the neutron beam must be controlled with an accuracy of approximately 30 nm.

From this coherence length, the required accuracy of the mirror installation is estimated. The mirror arrangement can be considered broken down into the following axial directions, respectively

- Gap spacing between paired mirrors (ΔD)

- Rotation of opposing mirrors ($\Delta\theta_H$ and $\Delta\theta_V$)

- Rotation between pair mirrors ($\delta\theta_H$ and $\delta\theta_V$)

These items can be written as shown in Figure 5.8. The installation accuracy of each mirror is determined by the angle of incidence of neutrons to the mirror θ, the distance between the twin-pair mirrors D, and the distance from the mirror to the detector L, in addition to the coherent length. Here we use a typical setup of $\theta = 1$ deg, $D = 200$ μm, and $L = 1$ m, and calculate the installation accuracy for each axis.
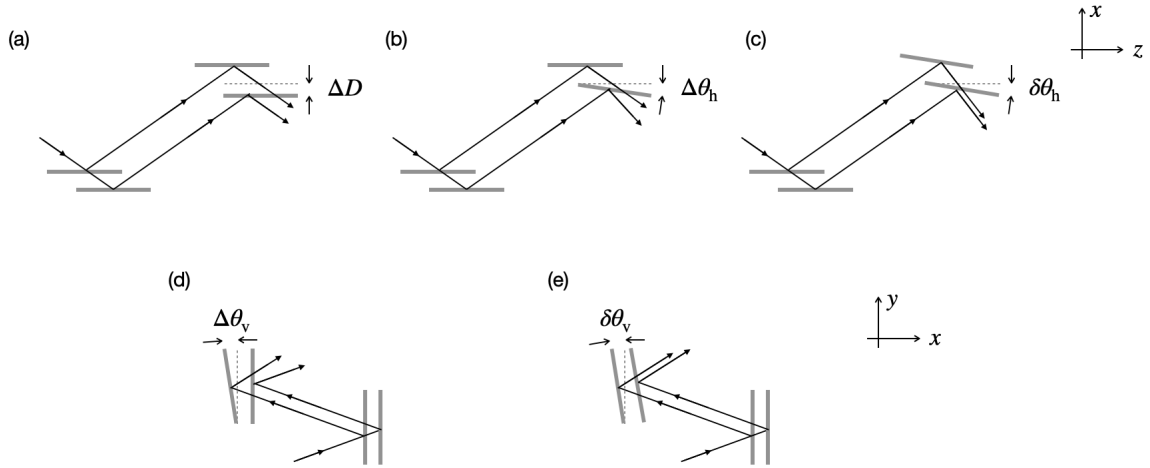

Figure 5.8: Axial direction for mirror alignment. The z axis is the longitudinal direction, and neutrons fly in this direction. Note that the coordinate axes point in different directions for the top three (a–c) and the bottom two (d, e).

When the spacing difference between the two paired mirrors is ΔD (Figure 5.8a), the lateral optical path difference and the requirement for the difference is

$$2\Delta D \sin\theta \quad \lessgtr \quad L_{\mathrm{v}}^{c} \tag{5.43}$$

$$\Delta D \quad \lessgtr \quad 0.97 \ \mu\mathrm{m} \tag{5.44}$$

The vertical direction can be calculated in the same method:

$$2\Delta D \cos\theta \quad \lessgtr \quad L_{\mathrm{h}}^{c} \tag{5.45}$$

$$\Delta D \quad \lessgtr \quad 1.0 \ \mu\mathrm{m} \tag{5.46}$$

Therefore, the spacing between two pair mirrors must be matched with an accuracy of less than 1 μm.

Next, we focus on the angle difference between opposing mirrors. When one mirror makes an angle of $\Delta\theta$ with respect to the opposing mirrors, the two superimposed beams separate at an angle of $2\Delta\theta$ (Figure 5.8b). In this case, the superimposed beam at the detector position has the optical length shift, and this required accuracy is

$$2L\Delta\theta_{\mathrm{h}} \quad \lessgtr \quad L_{\mathrm{h}}^{c} \tag{5.47}$$

$$\Delta\theta_{\mathrm{h}} \quad \lessgtr \quad 1.0 \ \mu\mathrm{rad} \tag{5.48}$$

In the vertical direction, the difference in length depends on the incident angle θ (Figure 5.8d). This shift and the required accuracy can be written as follows.

$$2L\theta\Delta\theta_{\mathrm{v}} \quad \lessgtr \quad L_{\mathrm{v}}^{c} \tag{5.49}$$

$$\Delta\theta_{\mathrm{v}} \quad \lessgtr \quad 0.97 \ \mu\mathrm{rad} \tag{5.50}$$

Therefore, the angular difference between the opposing mirrors must match with an accuracy of less than 1 μrad. Assuming a mirror area of 10 mm, this parallelism requires an accuracy of about $\lambda_{\mathrm{HeNe}}/60$ for the mirror. Where the $\lambda_{\mathrm{HeNe}} = 630$ nm is the wavelength of HeNe laser, widely used to evaluate optical substrates.

Next, we focus on the angle difference between the paired mirrors (Figure 5.8c). The optical path difference due to the angular difference between the paired mirrors was obtained in Eq. (5.31). Considering only the first-order terms here for simplicity, the relative accuracy can be written as

$$2D\delta\theta_{\mathrm{h}} \quad \lessgtr \quad L_{\mathrm{L}}^{c} \tag{5.51}$$

$$\delta\theta_{\mathrm{h}} \quad \lessgtr \quad 80 \ \mu\mathrm{rad} \tag{5.52}$$

To observe interference fringes with high contrast, the two paired mirrors must be placed within a relative angle of 0.0046 degrees. There is the transverse shift between the superposed two beams of $2D(\cos\theta_{2} - \cos\theta_{1})$ for horizontal direction at the same time. This shift is 0.56 nm in $\delta\theta = 80$ μrad and is sufficiently smaller than the value of L_{H}^{c} to be ignored.

The tilt angle $\delta\theta_{\mathrm{V}}$ between the paired mirrors caused by twisting the optics results in a vertical shift between the two superimposed beams of $2D\sin\delta\theta_{\mathrm{V}}$ (Figure 5.8e). The condition that this shift be less than the coherence length is expressed as

$$2D\sin\delta\theta_{\mathrm{v}} \quad \lessgtr \quad L_{\mathrm{V}}^{c} \tag{5.53}$$

$$\delta\theta_{\mathrm{v}} \quad \lessgtr \quad 85 \ \mu\mathrm{rad} \tag{5.54}$$

This also requires the same accuracy as the horizontal direction. Given this context, the precise adjustment of the angular difference between two paired mirror components becomes a critical aspect in the construction of interferometers using mirrors. This adjustment is essential to ensure the proper functioning and accuracy of the interferometric measurements.

5.6 Beam Splitting Etalons

I constructed the interferometer using two Beam Splitting Etalons (BSEs) with a neutron mirror deposited on it. The schematic view of BSE is shown in Figure 5.9 The BSE consists of two glass substrates and spacers with an air gap of $D = 189$ µm, which were bonded by optical contact to keep the parallelism of two glass substrates[141]. The designed flatness of the substrate was 4.2 nm ($\lambda_{\mathrm{HeNe}}/150$) and the parallelism of the two mirrors was maintained at approximately 30 nm ($\lambda_{\mathrm{HeNe}}/20$), where the λ_{HeNe} is the wavelength of HeNe laser. The neutron mirrors were sputtered inside a glass substrate, one a total reflection mirror and the other a half mirror. The neutron mirror, crafted from a multilayer structure of Ni and Ti, was capable of reflecting momentum transfers in the range of $0.232 < Q < 0.292$ nm^{-1}[144].
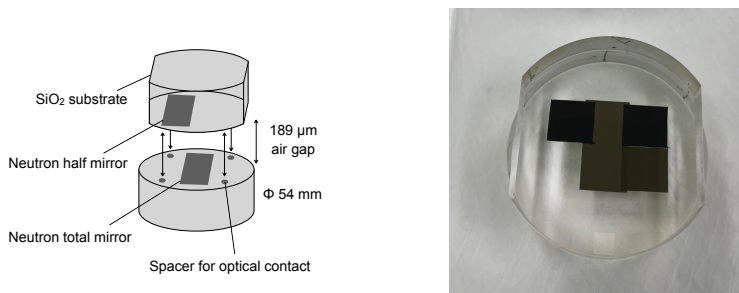
Figure 5.9: The configuration of beam splitting etalon (left) and this picture (right).

Each BSE is supported at two points from below on an aluminum fixture and is anchored in the horizontal (x) direction by a metal spring exerting a force of around 0.5 N. This setup is intended to prevent any potential falling of the BSE and to minimize deflection effects.

5.7 Experimental Configuration

The experiment was conducted at BL05 (NOP) within the Materials and Life Science Experimental Facility (MLF) at J-PARC[64, 65]. The beam power sustained during the experiments was 620 kW. The produced neutrons are provided to three branches through the neutron mirror bender located 7.2 m away from the moderator[86, 87]. This experiment used the Low Divergence Branch in this beam line. The available wavelength in this branch is longer than 0.2 nm, which TOF spectrum is shown in Figure 5.10. The neutron was provided toward the experimental setup via a four-blade slit and a vacuum guide tube. The slit width of vertical was set to $W_{\mathrm{ver}} = 44$ mm and the horizontal was $W_{\mathrm{hor}} = 6$ mm.

The experimental setup of the interferometer was placed following the beam port, which was 16.0 m away from the moderator. The overview of the experimental setup is shown in Figure 5.11. The Cd pre-slit of 400 µm width was placed 909 mm, the neutron assembly was 1259 mm away from the beam port. The Cd pre-slit, interferometer assembly, and sample insertion assembly were placed on an active vibration isolator. Among them, the interferometer assembly and sample insertion assembly were placed on an active vibration isolator and maintained at a consistent temperature of 23°C within a simple thermostatic chamber to minimize external disturbances. Over a duration of 9.2 h, the standard deviation of the temperature remained at 0.035 K. A detail discussion of temperature-dependent interference fringes is mentioned in section 5.12.
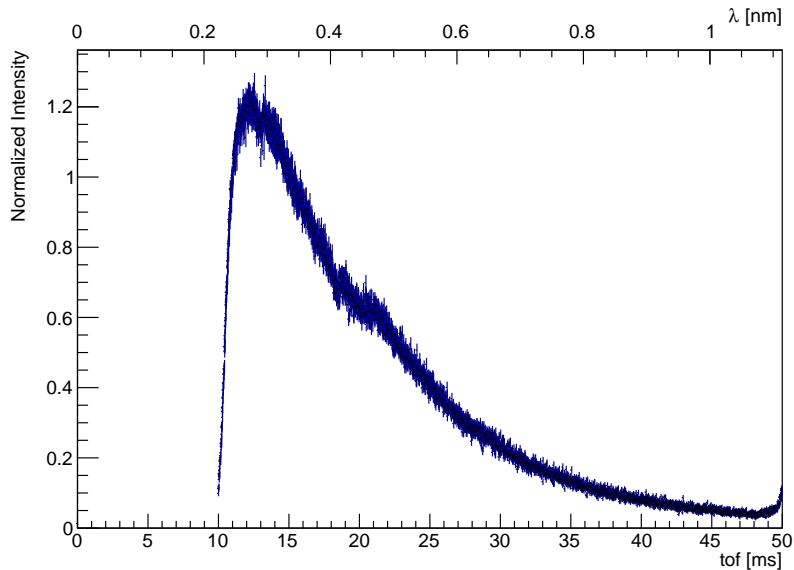
Figure 5.10: The TOF spectrum of the direct beam at low divergence branch in BL05.

The two BSEs were placed two 140 mm apart, as shown in Figure 3.7. These BSEs allowed the neutrons to be separated into two paths and superposed. The BSEs were positioned at an incident angle θ_1 of 1.05 deg with respect to the neutrons, with the centers of the two BSEs separated by a distance of 140 mm. These BSEs were held on a single aluminum plate to suppress disturbances. This adjustment facilitated the alteration of the incident angle of neutrons directed towards the 1st BSE. The fixture accommodating the two BSEs was positioned on an automated stage capable of movement in the rotational direction along the y and z axis. Among them, the axis that rotates around the y-axis is called the etalon yaw. The insertion sample was placed at the center of two BSEs using the sample insertion assembly. The assembly can move the sample to the x, y, yaw, pitch, and roll directions using automatic and manual stages.

The interference pattern of the neutron waves was detected as O and H beams by a neutron detector equipped with time and two-dimensional position detection capabilities[71]. The detector was placed 17.74 m away from the moderator, and 485 mm away from the center of the interferometer assembly.

5.8 Parallelism Alignments

The relative angles of the two BSEs were aligned by a laser-based autocollimator. The autocollimator irradiates a monochromatic collimated laser onto the object to be measured, and the parallelism can be measured from the position of the focal point of the reflected light. The parallelism of the two BSE surfaces, the measurement surfaces, is measured as shown in Figure 5.13 to determine the relative angles of the etalons. Since the front and back surfaces of the BSE are designed to be parallel, measuring the parallelism of the two BSE surfaces corresponds to measuring the parallelism of the mirror surfaces. The angular resolution of the parallelism of the parallelism to be measured, $\delta\theta$, can be written as

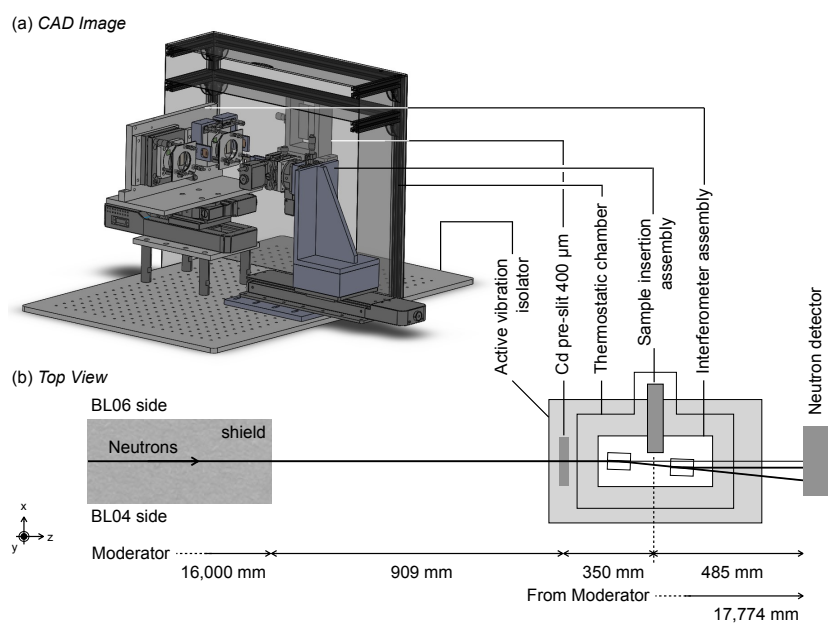$$\delta\theta = \frac{\Delta x}{2L}, \tag{5.55}$$

Figure 5.11: Overview of the experimental configuration of multilayer mirror interferometer.
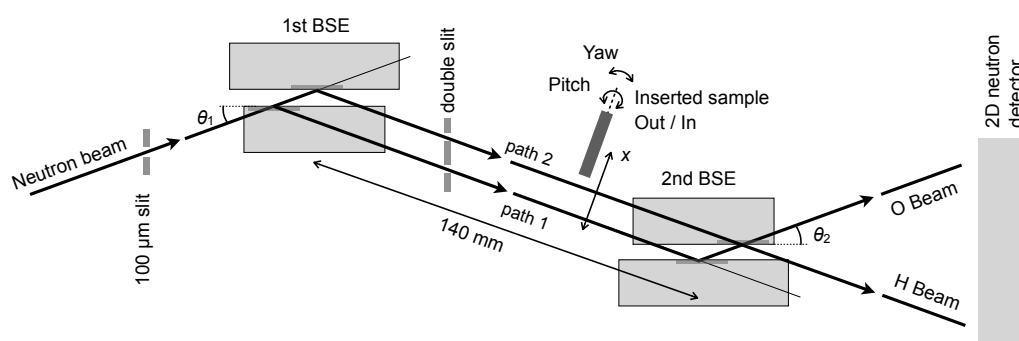

Figure 5.12: Schematic view of BSE. The configuration of the novel neutron interferometer was constructed by two BSEs.

where the dx is the difference position of the two laser spots, and L is the focal length of the telescope. The equipment used in this measurement was $L = 1000$ mm, and the pixel size of the CMOS camera installed on the autocollimator was 5.3×5.3 µm^2, so the angular resolution in parallel degrees was approximately 2.65 µrad. Since the laser spot size is 10–15 µm, the resolution is a little worse. The following histogram (Figure 5.14) shows the CMOS camera image taken during the alignment. As a note, the 2D histogram on the left side has been rebinned due to resolution, so the peak heights are different from the intensity distribution on the right side. Since the laser spot size calculated for the center of gravity was 484.7 ± 4.6 pixel, the angular resolution is estimated to be 12 µrad.
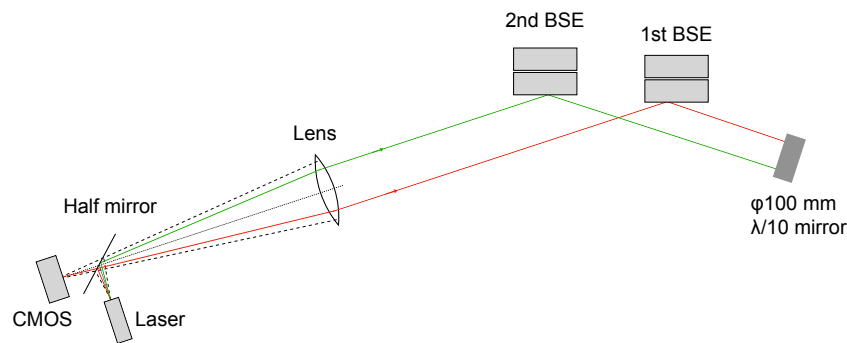

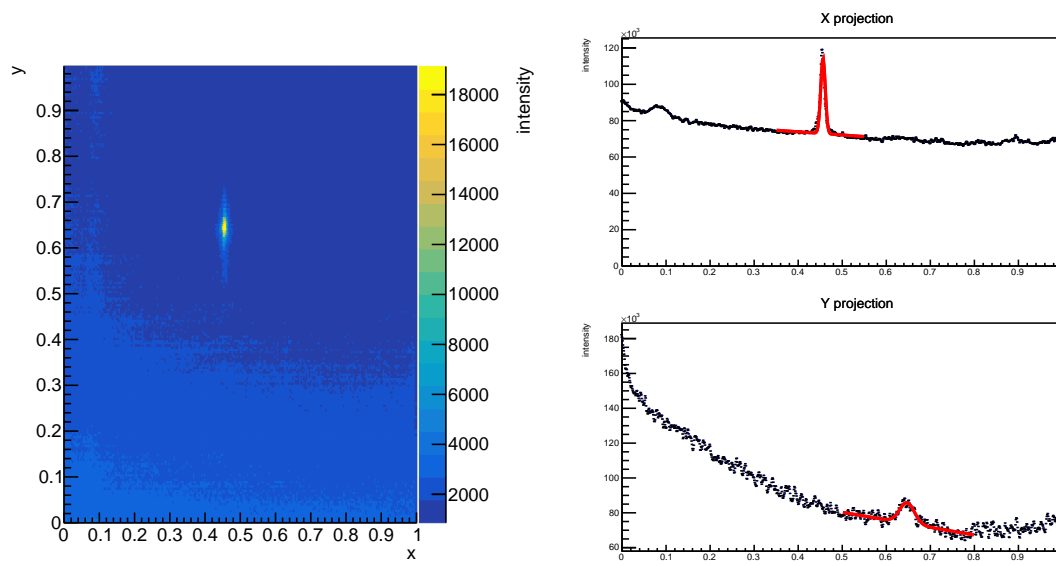Figure 5.13: Sketch of autocollimator.

Figure 5.14: The measured distribution of autocollimator. The spatial distribution is normalized.

The autocollimator was also used to measure the angle determination accuracy of the yaw stage with a fixed 2nd BSE. By deriving the difference in the measured position of the reflected laser when the yaw stage is moved by a small angle, the displacement angle can be determined with respect to

the amount of scale movement. The x-position of the laser spot observed at each $\delta\theta$ is shown in Figure 5.15, the y-position in Figure 5.16, and the displacement amount of each point is shown in Figure 5.17. The measured y-position was drifting at a particular point, which is a time variation due to the interval between measurements. This variation is canceled out by calculating the difference between the two points. The displacement angle to the yaw-axis stage scale is 0.123 ± 0.002 mrad/div from Eq. (5.55), and the relative uncertainty is 1.7%. This is consistent with the design value of 0.1222 mrad/div.
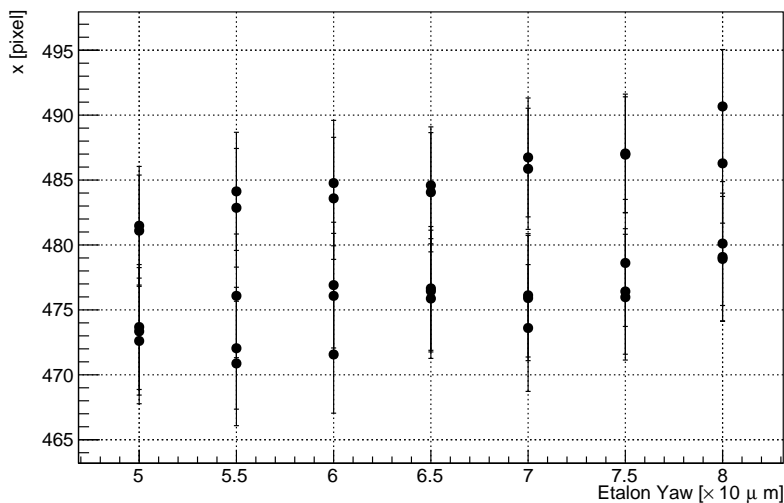

Figure 5.15: The etalon yaw division dependence of measured position x.

5.9   Two Path Separation by the BSE

In an effort to quantify the beam profile, a Cd mask measuring 1 mm in thickness was methodically traversed across the two beam paths situated between the BSEs. The Cd mask intercepted neutron waves by scanning in the x-direction using a sample insertion assembly. The measurement setup is shown in Figure 5.18. The scanned Cd mask intercepts neutron beams separated into two paths one by one. The neutron intensities pertaining to the O and H beams, along with their differentials, are shown in Figure 5.19. The distinct staircase pattern observable in the neutron intensities signifies that the neutrons were fully bifurcated into two separate pathways by the 1st BSE. A double Gaussian fitting applied to the derivative of the neutron intensity demonstrates that the separation between the two paths was measured at 326 µm, a value that is in agreement with the design specifications.

5.10   Interference Fringe

The relative angle, denoted as $\delta\theta = \theta_2 - \theta_1$, could be modified with a resolution of 6 µrad utilizing a micrometer affixed to the 2nd BSE. Following this precise alignment, periodic intensity distributions were discernible in the TOF region spanning from 35 ms to 50 ms (refer to Figure 5.22a). These oscillation patterns vanished when a single path was obstructed with a Cd mask, thus inferring that
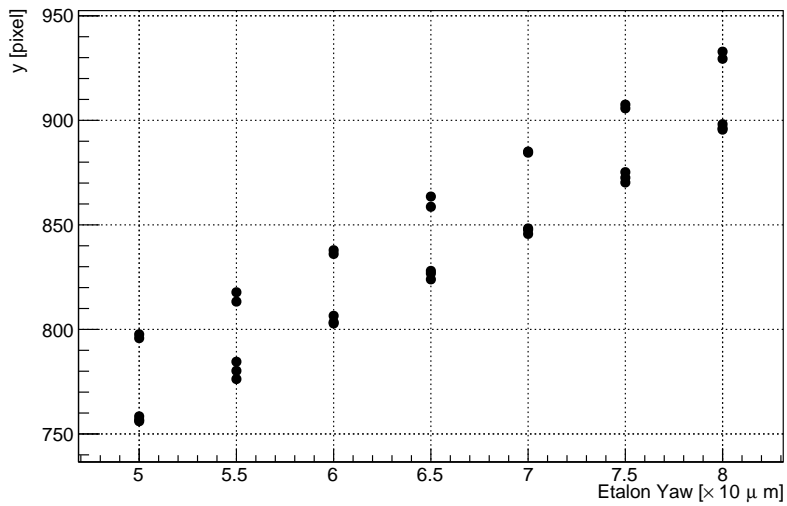
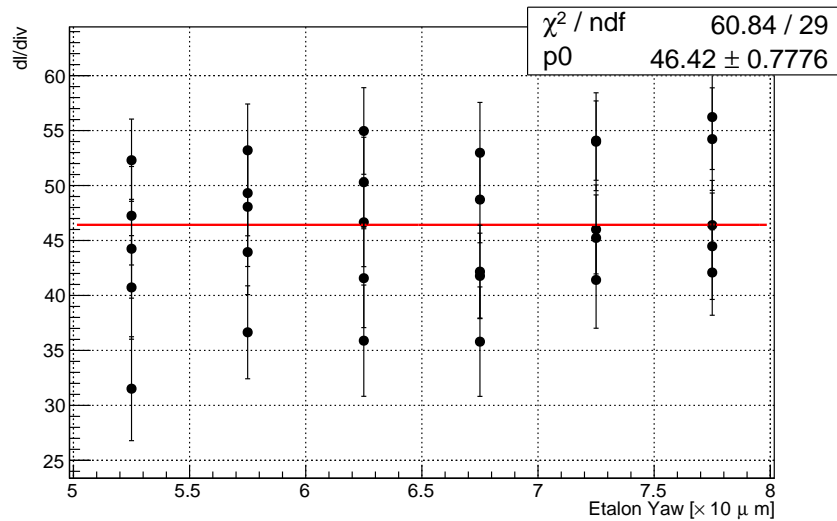Figure 5.16: The etalon yaw division dependence of measured position y.

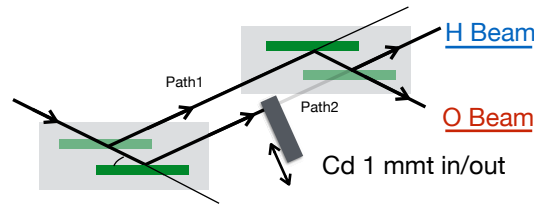Figure 5.17: Change in laser observation position relative to change in etalon yaw.
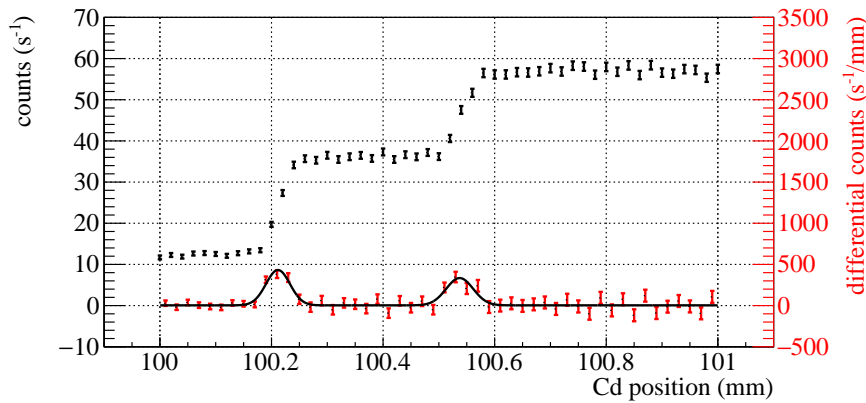
Figure 5.18: Cd mask scan measurement setup.

Figure 5.19: Overall neutron intensity of O and H beams in relation to the position of the Cd mask (black) and the corresponding differential intensity (red) that has been fit using a double Gaussian model.

these oscillations were consequences of the interference of neutron waves emerging from two separate paths.

Interference fringes were calculated from the following equation:

$$I(\lambda) = \frac{I_{\mathrm{O}}/I_{\mathrm{O_{Cd}}} - I_{\mathrm{H}}/I_{\mathrm{H_{Cd}}}}{I_{\mathrm{O}}/I_{\mathrm{O_{Cd}}} + I_{\mathrm{H}}/I_{\mathrm{H_{Cd}}}}, \tag{5.56}$$

where I_{O} and I_{H} represent the measured TOF spectra of O and H beams, respectively, while $I_{\mathrm{O_{Cd}}}$ and $I_{\mathrm{H_{Cd}}}$ symbolize the normalization spectra with a single path blocked by the Cd mask. The background is subtracted from each spectra. Each spectrum measured using a Cd mask is shown in Figure 5.20. The spectra of $I_{\mathrm{O_{Cd}}}$ and $I_{\mathrm{H_{Cd}}}$ were obtained by adding the O and H beams when path 1 was blocked and when path 2 was blocked. The observed spectra with the normalization spectra and background spectra are shown in Figure 5.21. Any prompt event stemming from proton collision with the mercury target within the $40 < \mathrm{TOF} < 40.1$ ms region was deliberately excluded from the analysis.

Phase shifts were evaluated by fitting the normalized interference fringes with a model function. The interference fringe, normalized by Eq. (5.56), is shown in Figure 5.22b. This interference fringe can be fitted by the following equation:

$$I(\lambda) = A\cos\left(\frac{P_{\mathrm{L}}}{\lambda} + P_{\mathrm{R}}\lambda - P_{\mathrm{S}}\lambda\right) + B, \tag{5.57}$$

where λ denotes the neutron wavelength. The λ was obtained by the TOF and the distance from
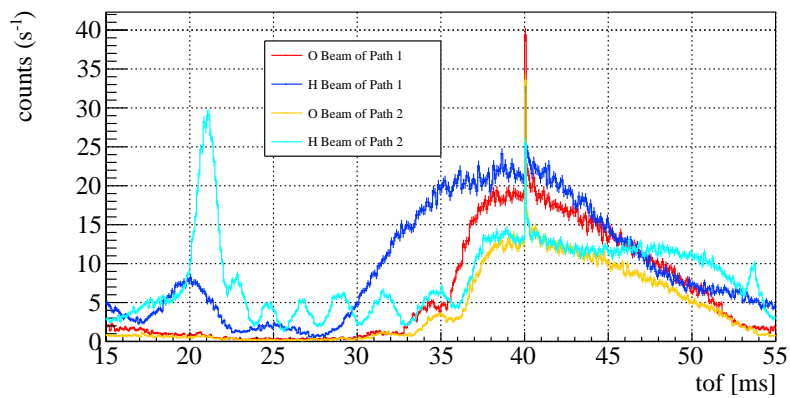
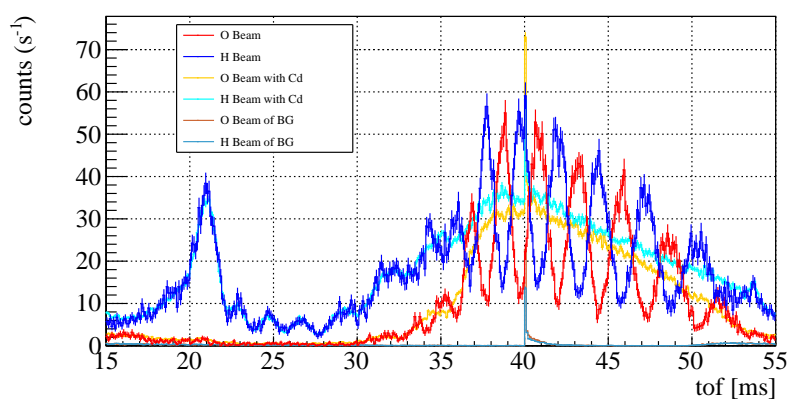Figure 5.20: The TOF spectra measured using Cd mask.

Figure 5.21: The measured TOF spectra, with the normalization and background spectra.

the moderator to the detector (17.74 m). The variables in this equation are related to the physical quantities in Eq. (5.34). The cosine function's initial term symbolizes the geometric optical length difference between the two paths, defined as $P_{\mathrm{L}} = 4\pi D\delta\theta$, with D representing the BSE's air gap. The second term represents the path difference times refractive index in SiO_2 of the BSE, denoted as $P_{\mathrm{R}} = -4\pi D\delta\theta mU/(h^2\theta_1^2)$, where U is the Fermi pseudopotential of SiO_2, m is the neutron mass, and h is Planck's constant. The third term represents the interaction with the inserted sample and can be articulated as $P_{\mathrm{S}} = Nb_{\mathrm{c}}t$, where N is the atomic number density, b_{c} is the neutron-nuclear scattering lengths, and t is the thickness. The sensitivity of the measured interactions is proportionally linked to the phase shifts written as the third term. The visibility, denoted by A, was typically around 60%. The other background, such as absorption effects, was ignored because they appear in B terms, which differ from the phase shift terms. The fitting algorithm used Migrad provided by CERN root. The fitting region was defined as the TOF range from 37 ms to 49 ms, where the interference fringes were distinctly visible.
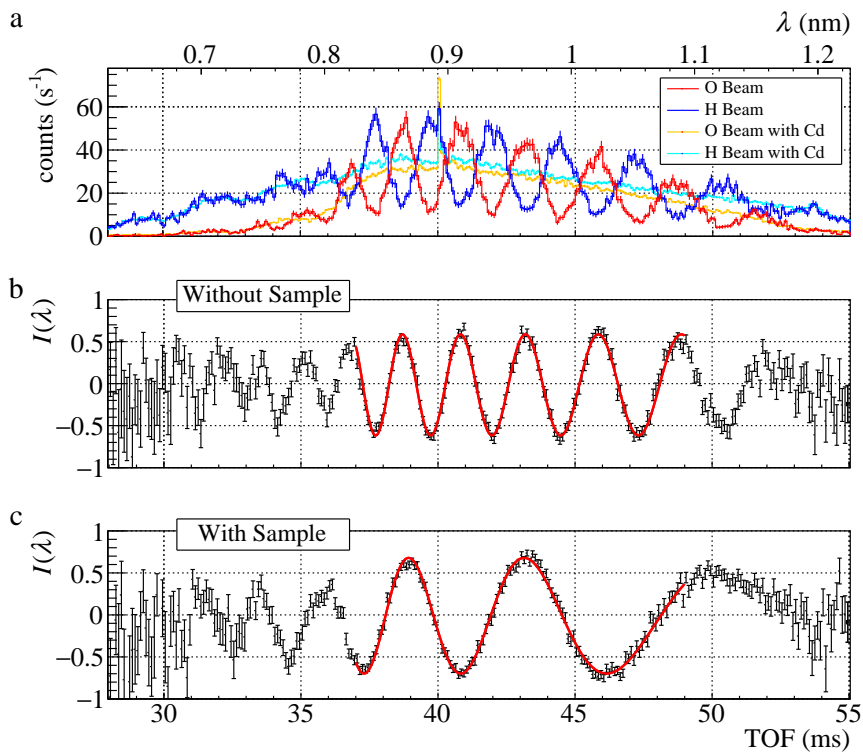

Figure 5.22: Time of flight (TOF) dependency of the measured interference fringes. (a) TOF spectra of neutron intensity in the O and H beams. The spectra corresponding to a single-path shielding with Cd are also represented in the same figure, derived from the sum of path 1 and path 2 shielding. (b) Interference fringes obtained from the above spectrum. (c) Variation in the interference fringes prompted by the insertion of an Si sample. The measurement time attributed to these fringes was 10 min. For each spectrum, background readings were subtracted.

5.11 Phase Shift caused by Geometric Path Length

The phase of the fringes can be manipulated by adjusting $\delta\theta$ with the micrometer attached in the 2nd BSE. The measured phase shift is proportional to the $\delta\theta$ by Eq. (5.57). The interference patterns obtained by varying $\delta\theta$ are shown in Figure 5.25. Each pattern displayed a different period corresponding to the micrometer scale values. The variation in these periods was evaluated by fitting with Eq (5.57). In the process of fitting periodic functions, the chi-squared value gives good results even for functions that differ from the optimal solution by 2π; that phenomenon is known as the local minimum problem. This can pose a challenge in obtaining optimal solutions during the fitting process. To circumvent this issue, the chi-squared values of the fitting functions with a fixed phase term were calculated for the data points. These calculated chi-squared values are presented in Figure 5.23. The phase difference shows a strong correlation between P_L and P_R, with each "groove" repeating at π intervals. The optimal solution for fitting was obtained by fitting the initial value of the phase term as a free parameter in the vicinity of each groove. Here, the fitting parameters for the phase shift were restricted to a range of $\pm\pi/2$ from the initial values. The chi-square values obtained by fitting in each groove are shown in the Figure 5.24. The optimal solution was the value with the smallest chi-square value. The chi-squared value at each groove changes according to a quadratic function as it moves away from the optimal solution. The point where this chi-square reaches $\chi^2_{\min} + 1$ corresponds to the standard deviation.
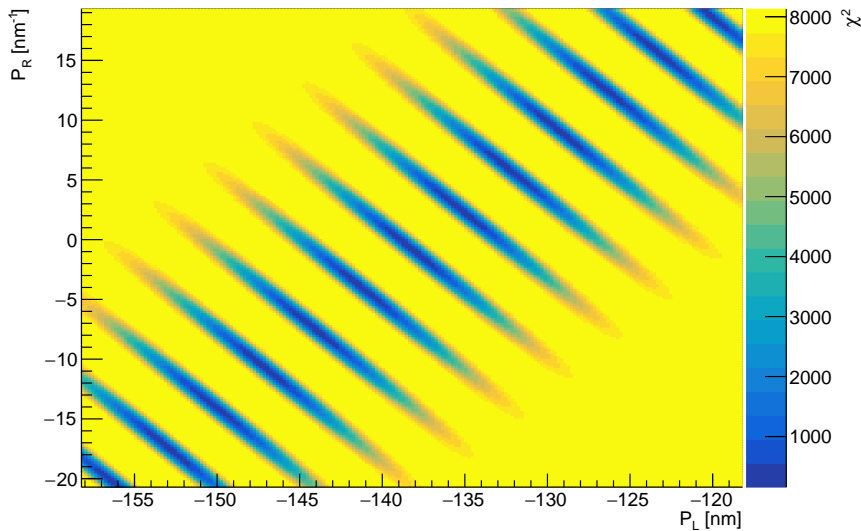

Figure 5.23: The χ^2 of the fitting for the interference fringe at $\delta\theta = 6.9$ div.

The change in P_L with respect to $\delta\theta$ was measured to be 2.13 ± 0.01 nm/µrad (refer to Figure 5.26a), which is roughly 10% less than the theoretical value of 2.38 nm/µrad. The change in P_R was calculated to be -0.096 ± 0.020 nm/µrad (refer to Figure 5.26b), approximately a quarter of the theoretical value of -0.39 nm/µrad. These deviations are speculated to arise from geometric inaccuracies in the BSEs or potential misalignment of the micrometer. Importantly, these effects can be counteracted by computing the phase shifts both with and without the sample present.
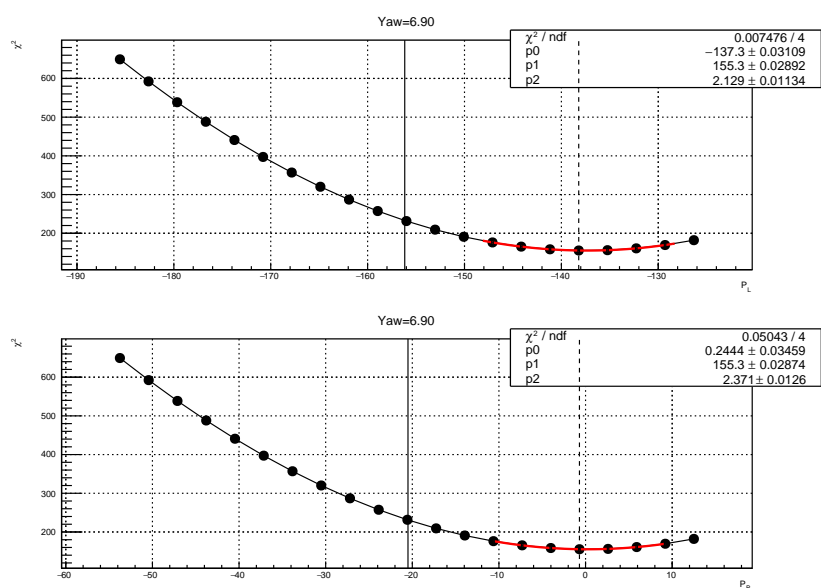
Figure 5.24: The minimum χ^2 of each groove at $\delta\theta = 6.9$ div.
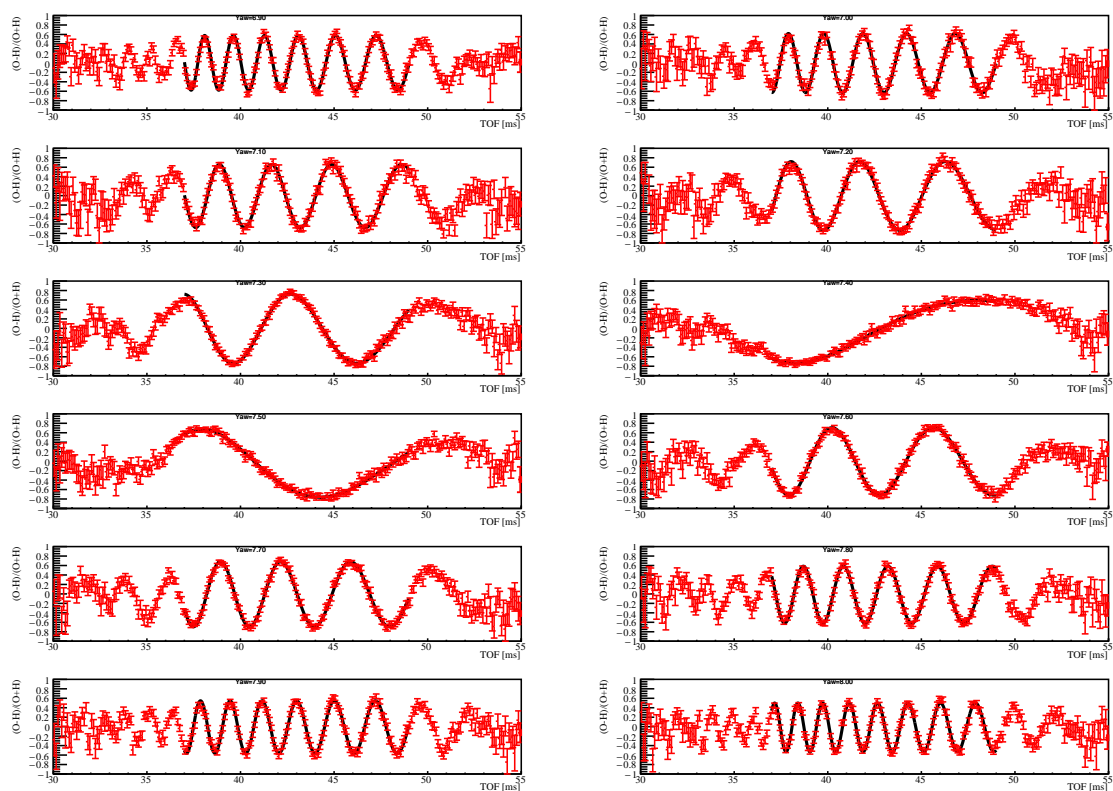

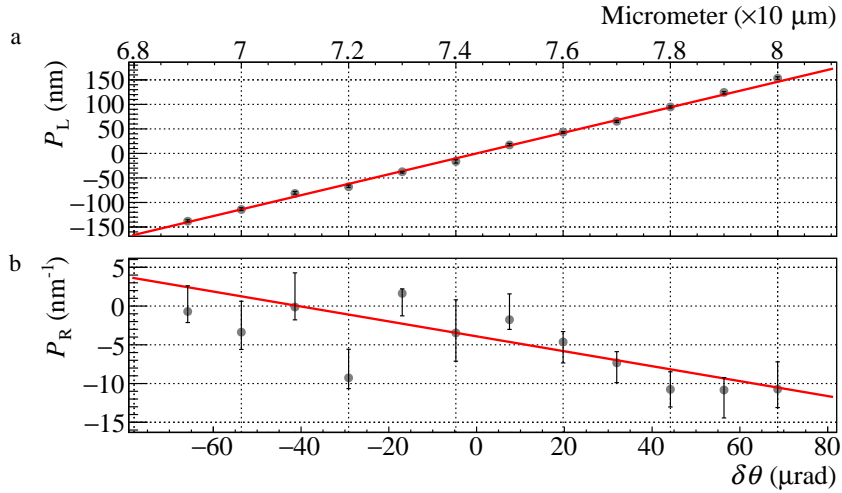Figure 5.25: The interference fringe on each $\delta\theta$.

Figure 5.26: Relationship of $\delta\theta$ with (a) P_{L} and (b) P_{R}, characterized by a linear function. The conversion factor between the micrometer value and $\delta\theta$ is established as 12.22 µrad/µm. The baseline value for $\delta\theta$ was determined through the fitting process applied to P_{L}.

5.12 Fluctuation of Phase Shift

Interference fringes measured by an interferometer are constantly subject to variations due to disturbances such as temperature and time, so the phase shift varies with time. To evaluate this, the interference fringes were measured continuously with temperature. The temperature in the interferometer was read by K-type thermocouples mounted upstream and downstream in the aluminum plate of the interferometer assembly. The measured interferograms were divided into 10-minute intervals to obtain sufficient visibility, and the period was obtained from a fit by the Eq. (5.57). The temperature was taken as the average value within each measurement time from the data logged every 10 seconds. The relationship between the measured phase shift and time is shown in the Figure 5.27, along with the temperature. The standard deviation of the observed values was used for the variation in phase shift and temperature, respectively. The phase variations over time were $\Delta P_L/\Delta t = 3.9 \times 10^{-4}$ nm/min and $\Delta P_R/\Delta t = 1.5 \times 10^{-4}$ nm^{-1}/min. The sample term variation was 3×10^{-3} rad par 20 minutes, which time is one dataset of measurement of the potential difference by sample insertion. This variation is four orders of magnitude lower than the phase shift caused by the Si sample, which was roughly 60 rad. These findings demonstrate the interferometer's effectiveness within a simple thermostatic chamber, thereby signifying its robust stability during extended periods of measurement.

Next, the temperature setting of the thermostatic cell was artificially changed and the interferometer was subjected to a temperature change. The phase shift and temperature observed at this time are shown in Figure 5.28 The phase variations over temperature were $\Delta P_L/\Delta T = 2.7$ nm/K and $\Delta P_R/\Delta T = 0.23$ nm^{-1}/K. The sample term variation was 6.8×10^{-4} rad par 3×10^{-3} K, in which temperature variation is the stability of the thermostatic chamber. This suggests that the temperature-dependent variation in phase shift is an order of magnitude smaller than the variation with time.
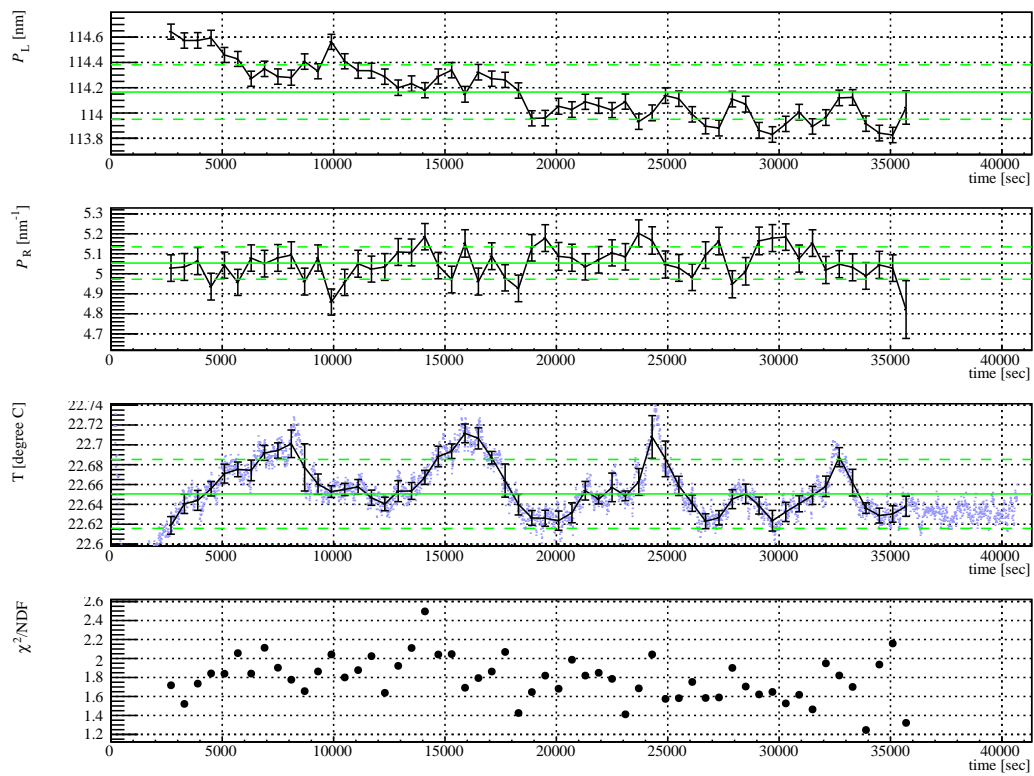
Figure 5.27: Time dependence of the temperature and phase shift parameters and the χ^2 of each fitting while long run.
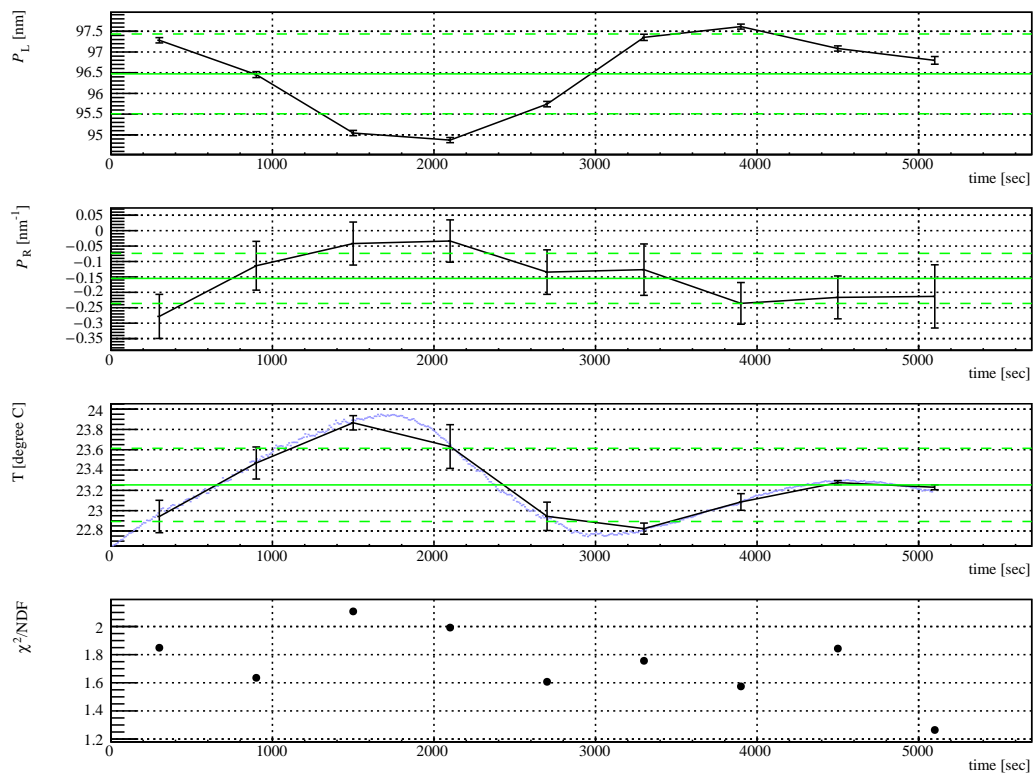
Figure 5.28: Time dependence of the temperature and phase shift parameters and the χ^2 of each fitting when the temperature is intentionally varied.

5.13   Measurement of Neutron-Nuclear Scattering Length

The potential of a sample is obtained from the phase shift between the sample insertion and removal. Interference fringe measurements were repeated at 10-minute intervals with and without the sample. The obtained fringe was split at 5-minute intervals, creating one data set of sample out-in-in-out to eliminate the effects of disturbances. To ensure accurate results, we carefully adjusted the samples to minimize phase shifts in the interference fringes using three-axis stages (Figure 5.12). Particularly, the alignment of the measurement sample in the x-direction was conducted with great care due to the short distance of approximately 100 µm between the two paths. Figure 5.29 shows the changes in the interference fringes when the sample was scanned in the x-direction. When the sample obstructed the neutron wave in one path, the phase changed distinctly. When the sample overlapped both paths or was outside them, the phase difference remained the same. This phase shift was used to determine the sample's position in the x-direction. The measurement sample needs to have a uniform thickness in the area where the beam passes, requiring sharp edges. To satisfy this precision, the sample was cut using a wire cutter, creating a sample that satisfies the necessary accuracy.
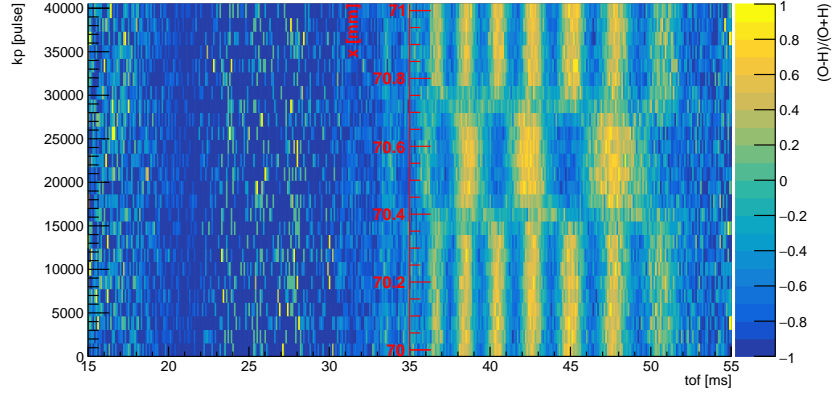

Figure 5.29: The observed phase shift in x-direction alignments.

I performed a global fitting for one dataset consisting of four interference fringes with the following equation:

$$I_0(\lambda) = A_0 \cos\left(\frac{P_\mathrm{L}}{\lambda} + P_\mathrm{R}\lambda\right) + B_0 \tag{5.58}$$

$$I_1(\lambda) = A_1 \cos\left(\frac{P_\mathrm{L}}{\lambda} + P_\mathrm{R}\lambda + P_\mathrm{s}\lambda\right) + B_1 \tag{5.59}$$

$$I_2(\lambda) = A_2 \cos\left(\frac{P_\mathrm{L}}{\lambda} + P_\mathrm{R}\lambda + P_\mathrm{s}\lambda\right) + B_2 \tag{5.60}$$

$$I_3(\lambda) = A_3 \cos\left(\frac{P_\mathrm{L}}{\lambda} + P_\mathrm{R}\lambda\right) + B_3, \tag{5.61}$$

where the P_L represents the optical path difference between two paths, P_R is the optical path times refraction index of SiO_2, and P_S donated by the inserted sample. In the four fittings, P_L and P_R were common parameters because the phase shifts due to geometrical optics do not change. The A and B were independent parameters. The parameter with the smallest sum of χ^2/ndf for the four fittings

was considered the best fitting. The measured one dataset is shown in Figure 5.30 along with the fitting functions.
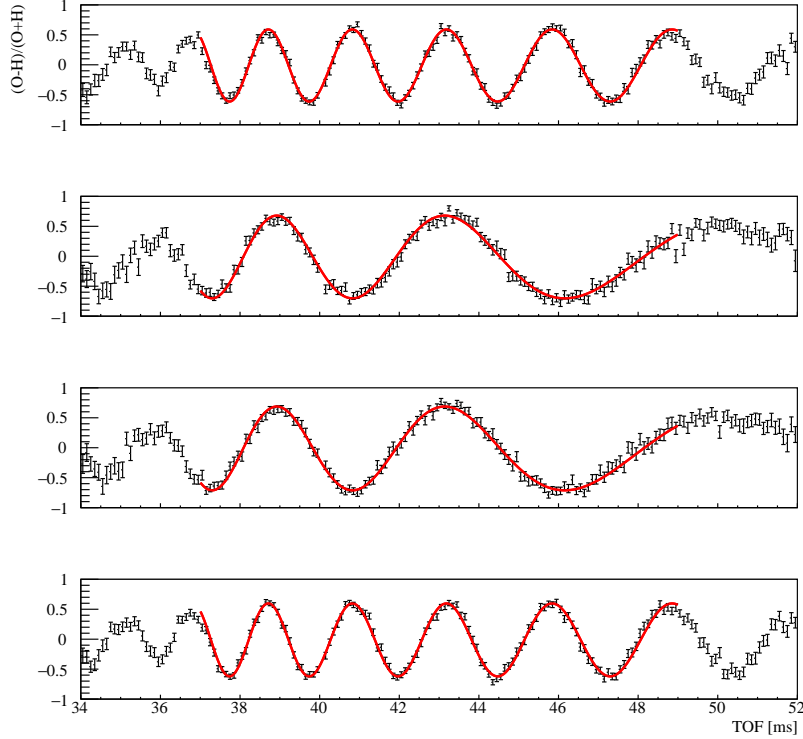

Figure 5.30: Typical interference fringe of one dataset. The inserted sample was 0.3 mm thick Si. These fringes are the "sample out-in-in-out" from the top to the bottom.

The effect of the disturbance is observed as a slight change in P_L and P_R, which appears in the χ^2/ndf in the fit result. To account for this effect, χ^2/ndf was multiplied by the uncertainty for each parameter obtained in the fitting when χ^2/ndf is greater than 1.

The interference fringe resulting from the introduction of a 0.3 mm thick Si sample into one of the paths is shown in Figure 5.22c. The phase underwent a significant change from the state without the sample. The capability to detect a phase shift induced by the sample was measured to be 0.02 rad per 20 min. This sensitivity exceeded that measured by NIST (0.31 rad per min)[145] by a factor of three and was comparable to that measured by ILL (0.08 rad per min)[129]. Notably, this experiment was conducted in the temperature stability of 30 mK. In contrast to Si interferometers, which require a temperature accuracy of 5 mK[146], the temperature accuracy in this experiment is relaxed by one order of magnitude, and the accuracy of phase determination is improved.

In our study, we measured Si and Al as representative nuclei, Ti and V as nuclei with negative b_c values, and V-Ni alloy as nuclei with near-zero b_c. V-Ni alloy is widely used as sample containers in neutron scattering experiments to prevent Bragg scatterings[147]. The V-Ni alloy is Fabricated by TAIYO KOKO Co., Ltd., and the Si sample used in this experiment was cut from an N-type wafer. To eliminate disturbances, we repeated the measurement of P_S with and without the sample for 5 min each. This process was carried out for several hours for each sample. The phase shift for each data set, derived from the interference fringes when each sample was inserted, is shown in Figure 5.31 for Al 0.1 mm thick, Figure 5.32 for Ti 0.1 mm thick, Figure 5.33 for Ti 0.2 mm thick, Figure 5.34 for

V 0.316 mm thick, Figure 5.35 for V 0.314 mm thick, and Figure 5.36 for V-Ni alloy. The black data point and error bar are the measured phase shift and its uncertainty. The red error bar is the reduced uncertainties obtained from the chi-square calculation progress, which is described above. The label on the horizontal axis indicates the number of the measured data set.

The $\delta\theta$ dependence of phase shift was measured for Al 1 mm thick and Si sample. These phase shifts are shown in Figure 5.37 for Al 1 mm thick, and Figure 5.38 for Si. The phase shifts obtained from the 1mm thick Al samples showed varying values depending on the $\delta\theta$. This phenomenon was not observed with the other samples, such as Si shown in Figure 5.38. It is anticipated to be more pronounced in samples that cause larger phase shifts, but this issue has not been fundamentally resolved yet. It is believed that a better understanding of this issue can be achieved by developing an interferometer capable of using a wide range of wavelengths and by improving the accuracy of phase shift fitting.

The obtained values of b_c, along with their systematic and statistical uncertainties, are summarized in Table 5.1. The values for Si, Al, and Ti were consistent with the literature values, with an accuracy of 2.2%. However, the results tended to be smaller compared to the literature values, which we attribute to systematic differences between the wavelengths obtained from the TOF method and the true values[148]. Importantly, the statistical uncertainty was two orders of magnitude smaller than the systematic uncertainty. To improve the accuracy of b_c determination, efforts should focus on reducing the systematic uncertainties arising from sample conditions. The uncertainties of each scattering length are explained in the next section.

Figure 5.31: The all dataset of measured phase shift P_S of Al 0.1 mm thick.

Figure 5.32: The all dataset of measured phase shift P_{S} of Ti 0.1 mm thick.

Figure 5.33: The all dataset of measured phase shift P_{S} of Ti 0.2 mm thick.

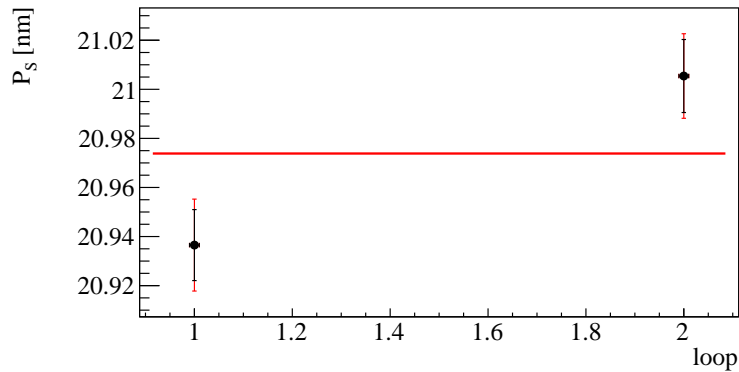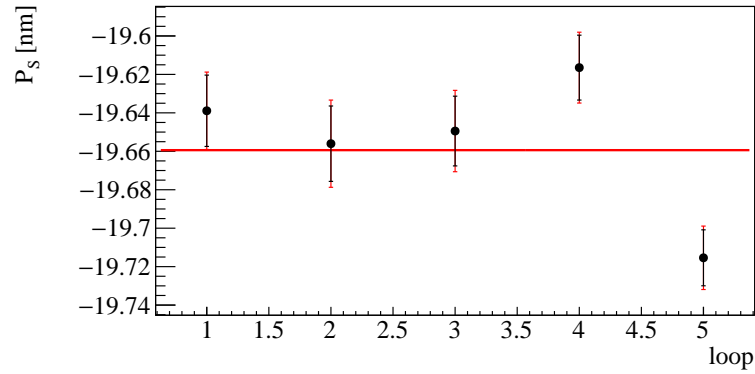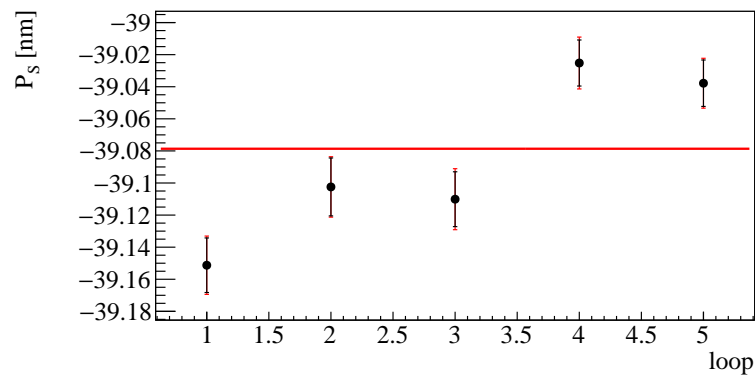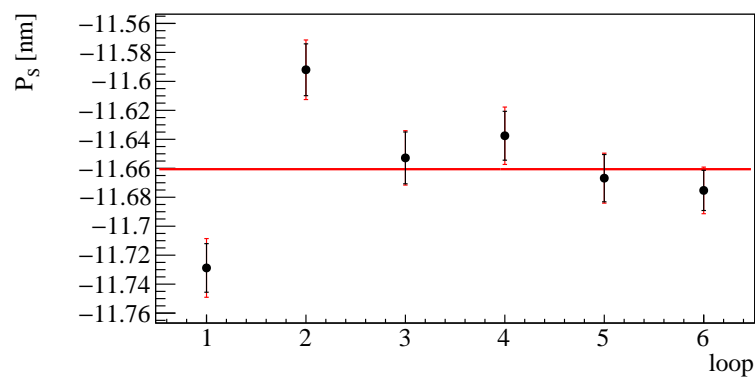Figure 5.34: The all dataset of measured phase shift P_{S} of V 0.316 mm thick.
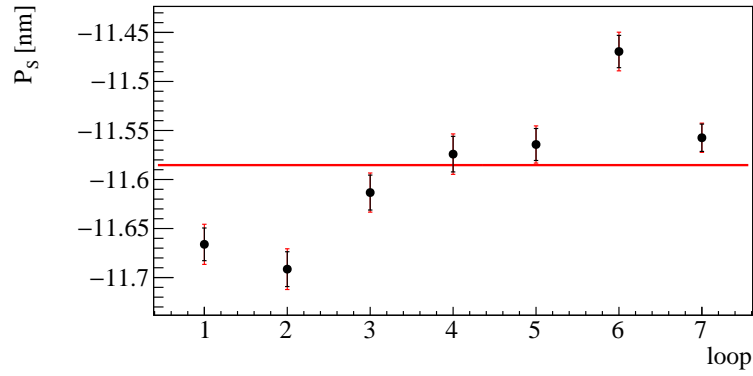
Figure 5.35: The all dataset of measured phase shift P_S of V 0.314 mm thick.
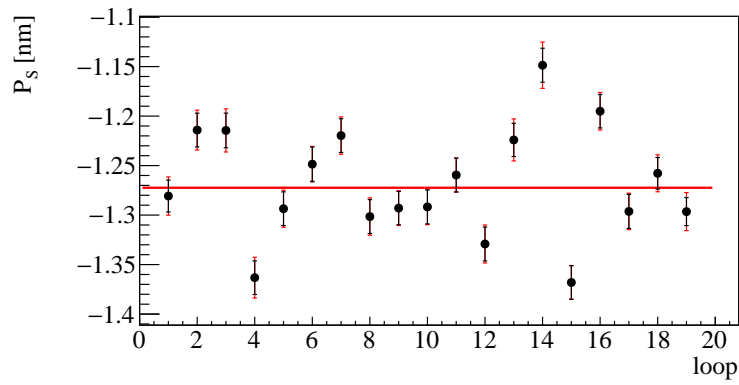

Figure 5.36: The all dataset of measured phase shift P_S of V-Ni alloy.
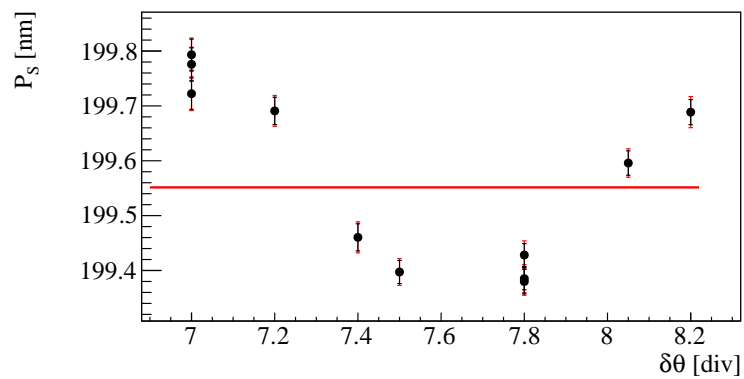
Figure 5.37: The Etalon Yaw dependence of measured phase shift P_S of Al 1 mm thick.
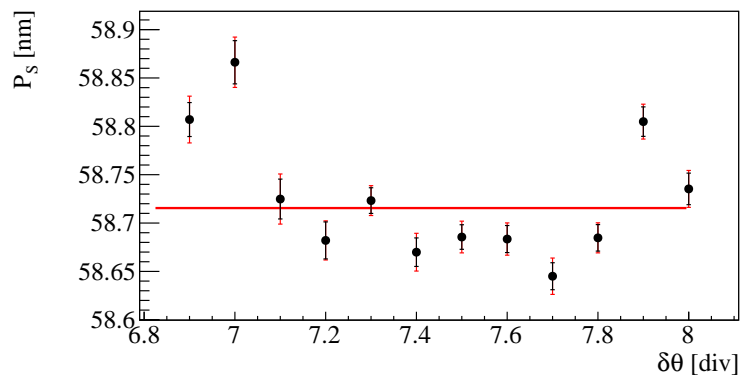
Figure 5.38: The Etalon Yaw dependence of measured phase shift P_S of Si.

Table 5.1: Each sample yielded measured b_c.

sample	t (mm)	Purity (wt%)	Stat. Unc.	Sys. Unc.	b_c (fm)	b_c/b_c^{ref}
Si	0.287 ± 0.001	$99.999+$	9.2×10^{-5}	6.7×10^{-3}	4.060 ± 0.027	0.978 ± 0.007
Ti	0.100 ± 0.002	$99.5+$	4.4×10^{-4}	1.8×10^{-2}	-3.477 ± 0.062	1.011 ± 0.018
	0.204 ± 0.004	$99.5+$	2.0×10^{-4}	1.9×10^{-2}	-3.386 ± 0.064	0.985 ± 0.019
Al	0.103 ± 0.001	$99+$	6.0×10^{-4}	1.5×10^{-2}	3.408 ± 0.050	0.988 ± 0.015
	0.287 ± 0.002	$99+$	5.3×10^{-5}	7.8×10^{-3}	3.423 ± 0.027	0.992 ± 0.008
	0.961 ± 0.001	$99+$	4.1×10^{-5}	5.7×10^{-3}	3.466 ± 0.020	1.005 ± 0.006
V	0.316 ± 0.001	$99.7+$	3.9×10^{-4}	6.8×10^{-3}	-0.522 ± 0.004	1.364 ± 0.010
	0.314 ± 0.002	$99.7+$	6.1×10^{-4}	7.2×10^{-3}	-0.520 ± 0.004	1.361 ± 0.011
V Averaged	—		—		-0.521 ± 0.003	1.363 ± 0.008
V-Ni alloy	0.315 ± 0.006	$V : Ni = 94.582 : 5.32$	3.1×10^{-3}	1.8×10^{-2}	-0.062 ± 0.001	-0.528 ± 0.010

5.14 Uncertainties

I considered the following systematic uncertainties for neutron-nuclear scattering length. The thickness of each sample was measured using a micrometer manufactured by Mitutoyo Corporation. Measurements were taken multiple times, and the mean and standard deviation of these measurements were used as the sample thickness and its uncertainties, respectively. These uncertainties include instrumental uncertainties.

The displacement of sample rotation with respect to the beam axis changes the effective thickness D_{eff} of the measured sample:

$$D_{\text{eff}} = D/\cos\theta \simeq \frac{D}{1 - \theta^2/2},\qquad(5.62)$$

where the D is the sample thickness measured by the micrometer and θ is the sample rotation angle with respect to the beam axis. This displacement was corrected by measuring the rotation-dependent phase shift of the sample, which was performed for yaw-and pitch-axis. The phase shifts depending on the yaw- and pitch-axis are shown in Figure 5.39 and 5.40, respectively. Each phase shift was fitted with a quadratic function. The sample rotations were aligned at the minima of the quadratic function.

The sample, such as V, was visually aligned perpendicular to the beam axis because we cannot observe the phase shift depending on the sample rotation. The uncertainty of the sample rotation for V and V-Ni alloy sample were adopted as the standard deviation of the minima obtained during the rotation alignment of Ti, Al, and Si. The derived standard deviation of yaw and pitch axes were $\sigma_{\text{pitch}} = 0.43$ deg and $\sigma_{\text{yaw}} = 1.56$ deg, respectively. Note that the uncertainty of effective sample thickness due to the rotation was much smaller than the absolute thickness.
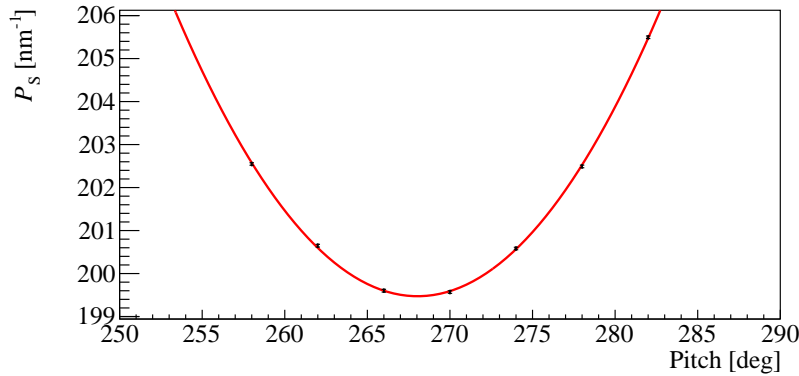
Figure 5.39: Measured P_{S} depending on the sample rotation of pitch.

The neutron wavelength was determined by the TOF method with the distance from the moderator to detector L. The L was 17.74 m, and the size of the moderator was about 10 cm. Assuming that the value of L has uncertainty only by the magnitude of the moderator, we adopted the uncertainty of 0.54%.

The atomic density N was obtained from the mass density ρ, atomic weight, and the Abogadro constant, in which the ρ is the most dominant uncertainty source. The atomic weight is determined with great precision[149]. The material density of the samples used in this experiment was measured by a specific gravity meter. The specific gravity meter can determine the material density from the ratio of the mass in the air to the mass in pure water. The instrumental uncertainty of this specific gravity meter was 0.08%, which value was adopted as the uncertainty of N.
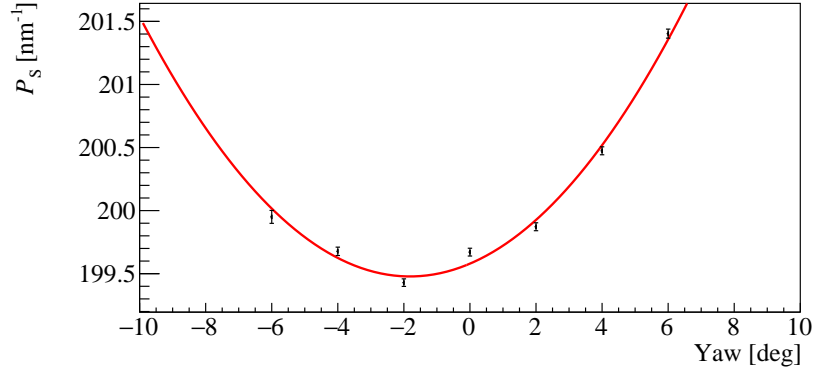
Figure 5.40: Measured P_S depending on the sample rotation of yaw.

Inserting a sample in one path of the interferometer shortens the path through the atmosphere by the thickness of the sample. The phase shift due to the sample was obtained by subtracting the effect due to the atmosphere from the measured phase shift. The atmosphere phase shift was calculated by following equation[122]:

$$\phi_{air} = (0.420 \pm 0.01 \ [\mathrm{m}^{-12}])D\lambda, \tag{5.63}$$

where the D is the sample thickness. The factor of phase shift was calculated using the 1010.5 hPa as atmosphere pressure, 23°C as temperature, and 15.25% as humidity. Each value is the average over the experimental period.

The relative uncertainties of the neutron-nuclear scattering lengths measured by each sample are shown in table 5.2. The summarized values indicate relative uncertainty with the obtained b_c.

Table 5.2: uncertainty table

sample	t (mm)	statistics	systematics	sample thickness	sample rotaion	wavelength	atomic densisty	air scat.
Si	0.287	9.2×10^{-5}	6.7×10^{-3}	3.8×10^{-3}	5.3×10^{-4}	5.4×10^{-3}	8.2×10^{-4}	4.9×10^{-5}
Ti	0.100	4.4×10^{-4}	1.8×10^{-2}	1.7×10^{-2}	1.0×10^{-5}	5.4×10^{-3}	8.2×10^{-4}	5.1×10^{-5}
Al	0.204	2.0×10^{-4}	1.9×10^{-2}	1.8×10^{-2}	4.0×10^{-4}	5.4×10^{-3}	8.2×10^{-4}	5.2×10^{-5}
	0.103	6.0×10^{-4}	1.5×10^{-2}	1.4×10^{-2}	4.9×10^{-5}	5.4×10^{-3}	8.2×10^{-4}	4.9×10^{-5}
	0.287	5.3×10^{-5}	7.8×10^{-3}	5.6×10^{-3}	4.5×10^{-5}	5.4×10^{-3}	8.2×10^{-4}	4.9×10^{-5}
	0.961	4.1×10^{-5}	5.7×10^{-3}	1.5×10^{-3}	7.5×10^{-6}	5.4×10^{-3}	8.2×10^{-4}	4.8×10^{-5}
V	0.316	3.9×10^{-4}	6.8×10^{-3}	4.1×10^{-3}	3.9×10^{-4}	5.3×10^{-3}	8.1×10^{-4}	2.7×10^{-4}
	0.314	6.1×10^{-4}	7.2×10^{-3}	4.7×10^{-3}	3.9×10^{-4}	5.3×10^{-3}	8.1×10^{-4}	2.7×10^{-4}
V-Ni	0.315	3.1×10^{-3}	1.8×10^{-2}	1.7×10^{-2}	3.6×10^{-4}	4.9×10^{-3}	7.8×10^{-4}	2.2×10^{-3}

5.15 Detailed Analysis of Vanadium

In contrast to the previously mentioned samples, the results for V and V-Ni alloy samples exhibited significant discrepancies with their respective literature values. I conducted elemental analyses on the V and V-Ni alloy samples used in the measurements to investigate the underlying cause of this observed discrepancy. However, no significant impurities were identified. To eliminate the uncertainty arising from the neutron wavelength of the pulse source, we determined the b_c of V from both V and V-Ni alloy samples relative to Si. The effects of measured impurities were also eliminated. The derived b_c values for V were -0.555 ± 0.003 fm from the V sample and -0.559 ± 0.005 fm from the V-Ni alloy sample, respectively. Note that we adopted the b_c of Si as 4.1491 ± 0.0010 fm, and b_c of Ni as 10.3 ± 0.1 fm[52]. The scattering lengths of vanadium determined in this experiment are shown in Figure 5.41, along with results from previous experiments. Both values of V were found to be in agreement, but were 45% different from the NIST recommended value of -0.3824 ± 0.0012 fm[150]. Supporting this result, a previous report indicated that the Bragg peak persisted unless the V-Ni alloy contained a higher amount of Ni than expected from the NIST database[147]. The following sections describe the impurity exclusion and relative measurement procedures.
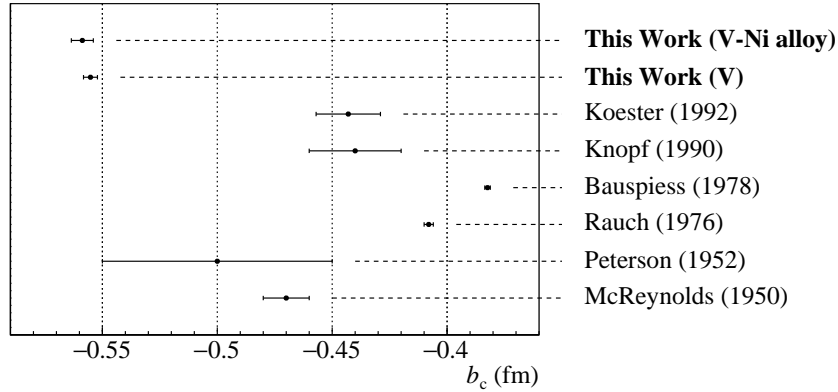
Figure 5.41: History of measured nuclear scattering length of vanadium.

Impurity Measurements

When impurities are included in the inserted sample, the phase shift obtained by the inserted sample is expressed as the sum of the phase differences due to each element. The observed phase shift is written by the equation:

$$\Delta\phi = \sum_i N_i b_i t \lambda, \tag{5.64}$$

where the i is the index of the contained atom, b is neutron-nuclear scattering length, t is the sample thickness, and the λ is neutron wavelength. The atomic density of the atom N_i is written by

$$N_i = \frac{\rho}{M_i} R_i N_A \tag{5.65}$$

where the R_i is the weighted ratio of the atom, ρ is the density of the sample, M is the atomic weight, and the N_A is Adogadro constant. The phase shift ϕ_i by the interested atom i is obtained by the

measured phase shift ϕ_{meas} minus contamination phase shift ϕ_{C}:

$$\Delta\phi_{\mathrm{i}} = \Delta\phi_{\mathrm{meas}} - \Delta\phi_c \tag{5.66}$$

$$N_{\mathrm{i}}b_{\mathrm{i}}t\lambda = \Delta\phi_{\mathrm{meas}} - \sum_j N_j b_j t\lambda \tag{5.67}$$

$$\frac{\rho}{M_{\mathrm{i}}}R_{\mathrm{i}}N_A b_{\mathrm{i}}t\lambda = \Delta\phi_{\mathrm{meas}} - \sum_j \frac{\rho}{M_j}R_j N_A b_j t\lambda \tag{5.68}$$

$$b_{\mathrm{i}} = \frac{M_{\mathrm{i}}}{R_{\mathrm{i}}}\left(\frac{\Delta\phi_{\mathrm{meas}}}{\rho N_A t\lambda} - \sum_j \frac{R_j}{M_j}b_j\right) \tag{5.69}$$

I performed an elemental analysis of the V and V-Ni alloy samples to investigate the cause of the discrepancy in the literature values. The analysis was performed by an X-ray fluorescence spectrometer (XRF) from Na to U, gas chromatography with thermal conductivity detection for H and N, and gas chromatography with non-dispersive infrared absorption methods for O. The XRF measurement was performed by RIKEN Materials Characterization Support Team, and the gas chromatography measurement was performed by TORAY Research Center, Inc. The samples used for XRF analysis were the same as those used in the experiment. The samples used for gas chromatography analysis were cut from the same base material as the sample used in the experiment. The measured contamination is shown in Table 5.3. The V_a had a thickness of 0.316 mm and the V_b had a 0.314 mm, these samples were cut from the same base material. The elements for which the mixing ratios measured by XRF were below the detection or quantitation limits were excluded. Uncertainties in the mass mixing ratios of XRF measurements were adopted only the statistical uncertainty. The uncertainties of the mass mixing ratios of H, N, and O could not be calculated due to the small amount of statistics, so the lower limit of quantitation was adopted.

While a high concentration of hydrogen impurities could have explained the negative deviation observed, the measured concentration was relatively low at only 3 ppm. Therefore, it becomes evident that the observed discrepancy cannot be solely attributed to hydrogen impurity. Vanadium metal is susceptible to oxygen contamination during the refining process[151]. Hence, it is presumed that this contamination occurred during that stage. Assuming the correctness of the b_c values obtained in this study, the estimated oxygen mixing ratio in the sample used in the NIST database is approximately 0.9%. Supporting this hypothesis, a previous report indicated that the Bragg peak persisted unless the V-Ni alloy contained a higher amount of Ni than expected from the NIST database[147].

Relative Measurements

In order to counteract systematic uncertainties, mainly originating from the accuracy of the wavelength determination of BL05, the nuclear scattering length is determined using the phase shift obtained with the Si sample as a reference standard. Since the Si sample had the fewest impurities and the literature values were determined with a high degree of accuracy, it was determined that this was the most optimal standard to use. The phase shift obtained in this case can be written as

$$\Delta\phi = nb_N t\lambda + Pt\lambda = \left(\frac{\rho}{M}N_A b_N - P\right)t\lambda, \tag{5.70}$$

where P is the phase shift coefficient due to the atmosphere. The ratio between the literature and experimental values of the phase shift of silicon is written as

$$\frac{\Delta\phi_{\mathrm{Si}}^{\mathrm{exp}}}{\Delta\phi_{\mathrm{Si}}^{\mathrm{ref}}} = \frac{\phi_{\mathrm{Si}}^{\mathrm{exp}}}{\left(\frac{\rho_{\mathrm{Si}}}{M_{\mathrm{Si}}}N_A b_{\mathrm{Si}}^{\mathrm{ref}} - P\right)t_{\mathrm{Si}}\lambda} \tag{5.71}$$

Table 5.3: Contamination of each sample. The unit of these values are wt%

atom	M	b_c (fm)	V-Ni alloy (wt%)	V_a (wt%)	V_b (wt%)
H	1.01	-3.739 ± 0.0011	0.0002 ± 0.0002	0.0003 ± 0.0002	0.0003 ± 0.0002
N	14.01	9.36 ± 0.02	0.02 ± 0.006	0.02 ± 0.006	0.02 ± 0.006
O	16.00	5.803 ± 0.004	0.023 ± 0.006	0.019 ± 0.006	0.019 ± 0.006
Al	26.98	3.449 ± 0.005	0.106 ± 0.0016	0.15 ± 0.0018	0.166 ± 0.002
Si	28.09	4.1491 ± 0.001	0.039 ± 0.00064	0.0666 ± 0.00078	0.0658 ± 0.0008
P	30.97	5.13 ± 0.01	0.013 ± 0.00021	0.0173 ± 0.00021	0.0145 ± 0.0006
S	32.06	2.847 ± 0.001	0.02 ± 0.00021	0.0229 ± 0.00021	0.0194 ± 0.0002
V	50.94	-0.3824 ± 0.0012	94.7	99.7	99.7
Fe	55.84	9.45 ± 0.02	0.029 ± 0.0012	0.0119 ± 0.00081	0.033 ± 0.0002
Ni	58.69	10.3 ± 0.1	5.055 ± 0.0096	0.0036 ± 0.0005	—
Cu	63.55	7.718 ± 0.004	—	0.00745 ± 0.00035	0.0057 ± 0.0002
Zn	65.38	5.68 ± 0.005	0.0088 ± 0.00035	0.00444 ± 0.00024	0.0039 ± 0.0005
Ge	72.63	8.185 ± 0.02	0.014 ± 0.0014	0.014 ± 0.0011	0.0135 ± 0.0003
As	74.92	6.58 ± 0.01	—	—	0.0019 ± 0.0004
Sn	118.71	6.225 ± 0.002	0.0081 ± 0.0006	0.006 ± 0.0006	—

When the scattering length of the interesting nucleus in the sample is b_i, the relative nuclear scattering length obtained is

$$b_i = \frac{M_i}{R_i} \left(\frac{\Delta\phi_{\mathrm{meas}}}{L\rho N_A t \lambda} \frac{\Delta\phi_{\mathrm{Si}}^{\mathrm{exp}}}{\Delta\phi_{\mathrm{Si}}^{\mathrm{ref}}} + \frac{P}{\rho N_A} - \sum_j \frac{R_j}{M_j} b_j \right) \tag{5.72}$$

$$= \frac{M_i}{R_i} \left(\frac{\Delta\phi_{\mathrm{meas}}}{\rho N_A t} \frac{t_{\mathrm{Si}}}{\Delta\phi_{\mathrm{Si}}^{\mathrm{exp}}} \left(\frac{\rho_{\mathrm{Si}}}{M_{\mathrm{Si}}} N_A b_{\mathrm{Si}} - P \right) - \sum_j \frac{R_j}{M_j} b_j + \frac{P}{\rho N_A} \right) \tag{5.73}$$

This equation does not include a wavelength term in the scattering length.

5.16 Future Developments

The statistical uncertainty associated with the measured phase shift was up to two orders of magnitude smaller than the systematic uncertainty, highlighting the considerable potential for highly sensitive measurements. To mitigate the uncertainty in wavelength determination, two approaches can be employed: conducting relative measurements to Si or performing precise wavelength measurements. Furthermore, improving the sensitivity of b_c can be achieved by utilizing thicker samples with reduced impurities. The systematic uncertainty arising from non-uniform sample thickness can be addressed by Ultra-high precision machining technology[76, 77].

The statistics can be increased by a factor of 20 by replacing the current multilayers with super-mirrors and reflecting neutrons within the optimal wavelength range of 0.2–0.8 nm at J-PARC BL05. This is advantageous when measuring small interactions and relative measurements. Extending the BSE's air gap would allow the measurement of various interactions such as gas samples using a gas cell[132, 14, 47].

5.17   Conclusion

I have developed a neutron interferometer utilizing multilayer mirrors. The successful operation of our interferometer with pulsed neutrons at J-PARC resulted in a visibility of 60%. Notably, our interferometer exhibited a remarkable precision of phase determination, achieving an accuracy of 0.02 rad within a 20-min interval. Moreover, our interferometer employed a neutron wavelength of around 0.9 nm, which offers enhanced sensitivity for specific applications compared to Si interferometers using 0.44 nm. The time-dependent phase shift measured in our interferometer was four orders of magnitude smaller than the phase shift induced by a 0.3 mm thick Si sample. This indicates that our interferometer is robust against fluctuations. By incorporating samples into one of the paths, we measured the b_c for Si, Al, Ti, V, and V-Ni alloy. These measurements demonstrated agreement with literature values within an accuracy of 2.2%, except for vanadium. This suggests that our neutron interferometer accurately captures the phase shift introduced by the inserted sample. About the b_c for V, further investigation is required to ascertain whether impurities present in the V sample contributed to the observed discrepancy. The utilization of a high-sensitivity neutron interferometer would open up possibilities for a range of new physics search experiments[132, 14, 135, 24, 44, 22, 133, 134].

The results of this research are supported by the fact that the multilayer neutron mirrors were installed within the required accuracy determined by the coherent length. The application of etalons, which are commonly used in laser optics, and autocollimators for neutron experiments has enabled precise positioning of the elements. This technique demonstrates the advance of neutron optics by improving the installation accuracy of components.

Part IV

Conclusion and Future Outlook

Chapter 6

Future Outlook

In this research, I have achieved advancements in neutron optics by employing cutting-edge engineering technologies. Through the development of large, flat neutron mirrors meeting the required precision, I successfully captured the optical reflection of epithermal neutrons. This result serves as evidence that epithermal neutrons can be handled optically, thus expanding the scope of neutron optics. By applying ultra-precision machining techniques to single-crystal samples used for neutron diffraction, I demonstrated that systematic errors arising from the components can be eliminated. This shows that ultra-precision machining technology can be used to remove systematic errors due to the shape of components. Neutron interferometers using multilayer mirrors met the installation precision requirements set by the coherence length by combining autocollimators with etalon in the development of neutron optics components. This illustrates that the use of advanced engineering technologies can eliminate uncertainties related to the installation accuracy of general optical components. The advancement of neutron optics demonstrated by these experiments can be utilized in the development of fundamental physics. In the following chapters, I will explain how the findings of this research can be applied to fundamental physics experiments.

6.1 Neutron-Antineutron Oscillations

To explain the origin of a matter-dominated universe, the existence of baryon number non-conservation processes is required. The breaking of baryon numbers, similar to flavor oscillations in neutrinos, suggests that neutrons can transform into antineutrons. Left-right symmetric grand unified theories, which predict the existence of heavy right-handed neutrinos, suggest that neutron-antineutron oscillations occur in the range of 10^9–10^{10} second. The observation of neutron-antineutron oscillations is based on the hypothesis that neutrons transform into antineutrons over a certain period. The detection is relatively straightforward because antineutrons react with neutrons to produce an average of five pi mesons. Measurements have been conducted on neutrons bound inside atomic nuclei and free-flying neutrons, with neither observation yielding antineutrons, only providing lower limits. The probability of neutron-antineutron oscillations occurring can be expressed by the following formula:

$$P_{n \to \bar{n}} = \frac{\alpha^2}{\alpha^2 + V^2} \times \sin^2\left(\frac{\sqrt{\alpha^2 + V^2}}{\hbar} \times t\right) \tag{6.1}$$

with

$$V = \frac{1}{2}\left(E_{\mathrm{n}} - E_{\bar{\mathrm{n}}}\right) \tag{6.2}$$

where the α is the mixing parameter, E_n is the neutron energy, and $E_{\bar{n}}$ is antineutron energy. As can be seen from this equation, long-duration flights are desirable because the reversal probability is time-dependent. In other words, long-distance flights of low-energy neutrons can improve the sensitivity of the search. The lower limit of the oscillation period has been investigated in experiments with long-distance flights of free neutrons of 76 m at the ILL reactor, and a lower limit of $\tau_{n\bar{n}} > 8.6 \times 10^7$ sec has been explored[40].

To enhance the search sensitivity, the NNBAR experiment is planned at the currently under-construction European Spallation Source (ESS)[152]. This experiment aims to observe the neutron-antineutron oscillation of low-speed neutrons, traveling at 1000 m/s over a distance of 200 m. The experiment plans to increase the statistical quantity by incorporating a focusing system between the neutron source and the detector[153]. The increase in statistics will be achieved by installing an ellipsoidal focusing system coated with a supermirror with an m-value of about 6, extending over approximately 20 m, positioned around 5 m away from the source[154]. The proposed setup for the NNBAR experiment is illustrated in Figure 6.1. Since such large mirrors cannot be fabricated in a single piece, they need to be divided into several segments for installation. Considering the need to focus the beam from a 24 cm moderator to a point 200 m away, the mirrors must be installed with at least 1.2 mrad precision. Given that the critical reflection angle for a mirror with $m = 6$ is around 7 mrad, an installation precision of less than 1 mrad is essential. While the installation of segmented ellipsoidal mirrors is still in the development phase, and there are no examples of using such large mirrors, this research successfully installed large mirrors with an accuracy of 0.3 mrad. Therefore, the challenges regarding the installation accuracy of mirrors in the NNBAR experiment can be overcome based on the findings of this research.
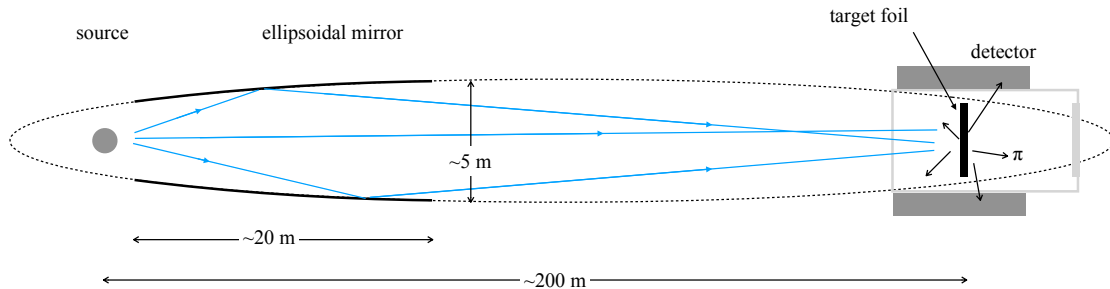

Figure 6.1: Configuration of NNBAR experiments.

6.2 Short Range Gravity

In modern physics, the existence of a fifth force is suggested by both particle physics and cosmology. As explained in Section 1.1.1, searching for the fifth force using neutrons is an extremely effective approach within the range of 10^{-11}–10^{-8} m. However, even with these experiments, there is still a shortfall of several orders of magnitude from the region predicted by new physics, necessitating further improvement in search sensitivity. Previous neutron experiments have primarily focused on neutron scattering for exploring the fifth force. Experiments utilizing neutron dynamical diffraction offer a method to break through the limitations of previous approaches. The most dominant systematic uncertainty in these experiments, the thickness of the single-crystal sample, has been eliminated using

ultra-precision machining techniques. As discussed in Chapter 4, future experiments, which include increasing the number of measurement points for crystal diffraction Q-dependence and conducting experiments using germanium, can enhance the sensitivity of the search for the fifth force. This approach represents a significant step forward in the ongoing quest to uncover and understand new physical forces.

6.3 Neutron-Nuclear Scattering Length

Neutron interactions are predominantly influenced by phenomena related to the potential of nucleons. The neutron-nucleon scattering length represents the interaction between neutrons and nucleons and varies with isotopes. This value is widely used as a fundamental parameter in neutron experiments and has been databased, owing to its importance. However, the current situation is that many of these values were measured around the 1970s and have not been updated for half a century. As the measurement accuracy of neutron experiments improves year by year, enhancing the precision of the parameters used in these experiments is essential. Furthermore, as mentioned in Section 1.1.5, a more profound understanding of nucleon structure requires more precise values. Therefore, improving the accuracy of these experimental values is anticipated from multiple perspectives, including both fundamental physics research and practical applications.

The nuclear scattering length can be measured using the neutron interferometer. The phase shift caused by the inserted sample is written as

$$\Delta\phi = nb_{\mathrm{c}}t\lambda, \tag{6.3}$$

where the b_{c} is the nuclear scattering length, n is atomic density, t is the sample thickness. The neutron interferometer developed in this study enables precise measurement of the nuclear scattering length by sample insertion. Furthermore, the use of a gas cell makes it possible to measure the nuclear scattering length of gaseous samples. This can provide realistic measurements for models of nucleon-nucleon interactions. The scattering length can be written using the spin singlet term and the triplet term as follows

$$b_{\mathrm{c}} = \frac{I+1}{2I+1}b_1' + \frac{I}{2I+1}b_0' \tag{6.4}$$

where I represents the direction of spin. In previous studies, measurements of the nuclear scattering length of ^{3}He have placed restrictions on some nucleon-nucleon interaction theories. The results are shown in Figure 6.2, which was taken from Ref.[47]. Experiments have been performed at several facilities and methods, each supporting a different theoretical system. Therefore, the neutron interferometer developed in this study can be used to measure the nuclear scattering lengths of light elements to add new experimental values.

6.4 Primordial Gravitational Wave

As demonstrated in Chapter 1.1, primordial gravitational waves represent the only current method capable of observing the state of the universe immediately following inflation. Before the clear-up of the universe, the momentum of particles was so immense that observations using electromagnetic waves were not possible. Consequently, it remains challenging to observe how fundamental particles and interactions were constituted during the period from the Big Bang to the clear-up of the universe. However, since gravitational waves are determined solely by the energy scale of inflation, they can impose strong constraints on models that induce inflation. Although gravitational waves have been detected in experimental setups around the world, the expected period of primordial gravitational waves is around 1 Hz, which implies the necessity of an interferometer arm length of approximately
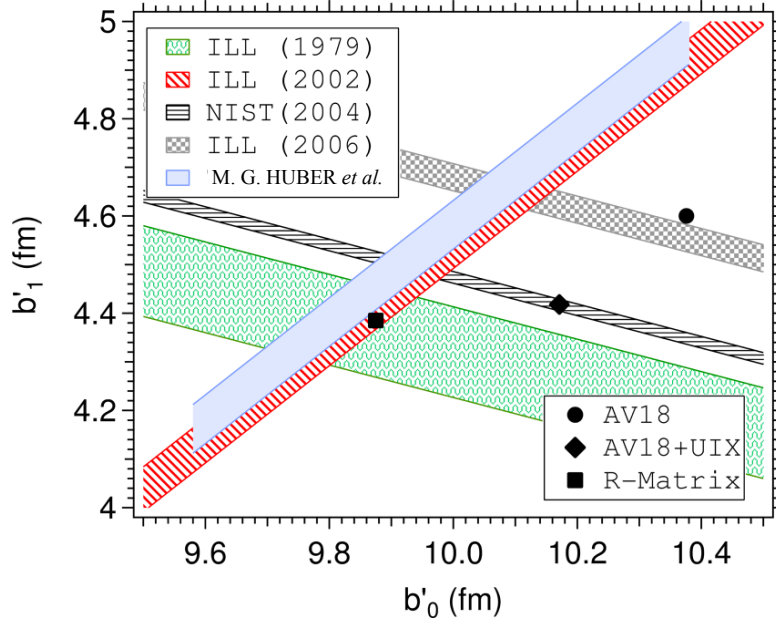
Figure 6.2: The comparison of nuclear potential models and measured scattering length.

3×10^8 m for current experimental setups. To detect primordial gravitational waves with realistically sized devices, it is necessary to develop a gravitational wave interferometer that can achieve long interaction times using matter waves, along with the elimination of background noise caused by mirrors. To address these challenges, the development of a gravitational wave interferometer using multi-wavelength neutrons has been proposed. This interferometer combines a Mach-Zehnder-type neutron interferometer with multi-wavelength neutrons. By combining neutrons at 100 m/s and 75 m/s with an interaction length of 75 m, it becomes possible to search for 1 Hz primordial gravitational waves[22]. The setup described above is impossible with a neutron interferometer using a fixed interaction distance and wavelength with a single silicon crystal. In contrast, the neutron interferometer developed in this research, employing multilayer mirrors, can accommodate the proposed setup. The proposed experimental system is illustrated in Figure 6.3. Accepting such an experimental system allows us to approach phenomena from the early stages of the universe's birth.

6.5 Lorentz Invariance

Lorentz symmetry is a fundamental principle in physics, forming the basis for various theoretical constructions. However, as explained in Chapter 1.1.4, theories aimed at the quantization of gravity for the construction of a Grand Unified Theory suggest the breaking of Lorentz symmetry at high energies. The breaking of Lorentz symmetry imparts an anisotropic effect on the momentum direction of particles like neutrons. Since this anisotropic effect is considered invariant with respect to the coordinates of the solar system, it suggests that the momentum undergoes diurnal variations. Even at low energies, neutrons, which carry large momenta, become powerful test particles for this phenomenon. The anisotropic effects dependent on the direction of neutron momentum can be measured using a neutron interferometer with non-parallel paths. In this scenario, the influence of Lorentz symmetry
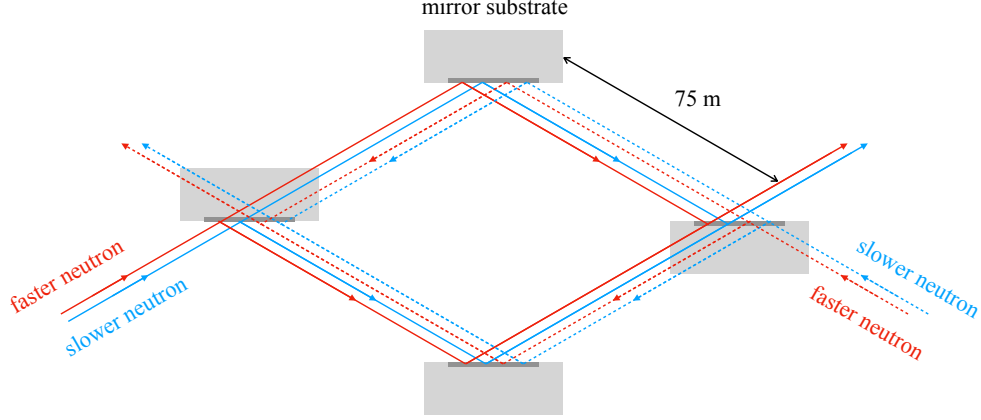
Figure 6.3: Proposed configuration of neutron interferometer to explore the primordial gravitational waves.

breaking can be represented by the following formula:

$$\Delta\phi \equiv \phi_1 - \phi_2 = G(\mathbf{R})\left(\frac{pmcL\Delta x}{\hbar^2}\right) \tag{6.5}$$

where p is neutron momentum, m is neutron mass, L is interaction distance, and Δx is lattice spacing, which is a discrete space breaking. G is an overall geometric factor depending on the arrangement of the interferometer and its orientation with respect to the underlying spatial lattice. When a non-parallel neutron interferometer is used, this value can be written as follows

$$G(\mathbf{R}) = (2/3)g\left(\mathbf{R}\hat{\mathbf{p}_1}\right) + (1/3)g\left(\mathbf{R}\hat{\mathbf{p}_2}\right) - (2/3)g\left(\mathbf{R}\hat{\mathbf{p}_3}\right) - (1/3)g\left(\mathbf{R}\hat{\mathbf{p}_4}\right) \tag{6.6}$$

In the proposed experimental setup, $\hat{\mathbf{p}}$ represents the four distinct momentum directions of neutrons as they travel through the interferometer, and $\mathbf{R}$ denotes the rotation of the interferometer with respect to the coordinate system of the solar system. The experimental setup is illustrated in Figure 6.4. Assuming a typical interaction distance of 10 cm for the interferometer and $g \sim 0.1$, the phase shift caused by the breaking of Lorentz symmetry that can be explored is $3 \times 10^{24}\Delta x$. Given that the interferometer developed in this research has a phase determination accuracy of 10^{-4} rad, it allows for the verification of symmetry breaking with an accuracy of 3×10^{-29} m. When converted to the same dimensions, the region explored at LHC CERN corresponds to 1×10^{-18} m. Thus, an improvement in sensitivity of 11 orders of magnitude is expected. For a more detailed description, see Ref.[44]. The development of the non-parallel neutron interferometer is achieved by independently positioning four mirrors, which is not feasible with silicon single-crystal interferometers where four diffractive components are fixed to a single ingot. Therefore, the multilayer neutron interferometer can realize the verification of fundamental physical symmetries with high precision. This advancement opens new avenues for exploring fundamental aspects of physics that have not been accessible with traditional methods.
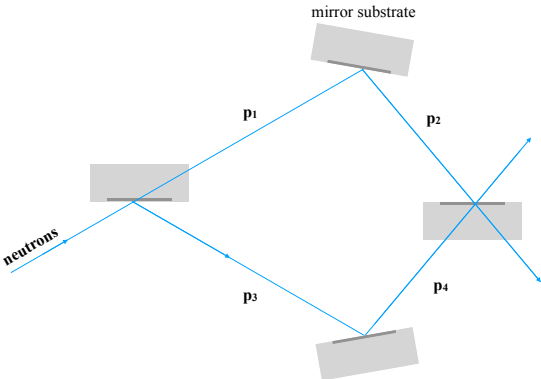
Figure 6.4: Proposed configuration of matter interferometer to verify the Lorentz invariance.

Chapter 7

Overall Conclusion

In fundamental physics, there is a concerted effort to gain a deeper understanding of the behavior and interactions of elementary particles, with the goal of broadly and generally comprehending physical phenomena. Currently, the Standard Model of particle physics, which unifies electromagnetism and the weak force among the four fundamental interactions, is capable of explaining most physical phenomena with the greatest accuracy. However, theories including the remaining strong force and gravity are still under development, and understanding these interactions remains a challenge in fundamental physics. The progress in theoretical physics has always been supported by empirical verification through experiments. Among various experiments, those using neutron optics have yielded many significant results, as this method allows for the optical handling of neutrons, which have mass and no electric charge. Besides achieving key findings in measuring nuclear interactions, verifying quantum mechanics, and enhancing the understanding of gravity, neutron optics have recently been proposed for experiments exploring the fifth force, CP symmetry violation, and baryon number non-conservation, maintaining its high utility value.

Neutrons, unable to be focused using electromagnetic forces, require the utilization of large-area beams to ensure adequate statistical data. Therefore, in neutron optics, either the use of large optical components with maintained accuracy or high-intensity neutron sources is essential. The introduction of pulsed neutron sources has substantially decreased statistical uncertainties, significantly advancing neutron optics. However, the requirement for precision ranging from micrometers to nanometers in neutron optical components presents a challenge in scaling up. To further develop neutron optics, tackling three key challenges is imperative: the development of large optical components with maintained accuracy, enhancement of component shape accuracy, and improvement in component installation accuracy. My approach to resolving these issues involved employing advanced machining technologies in the development of neutron optical components. These challenges were addressed and demonstrated through a series of three experiments.

The large optical components with maintained accuracy were validated using epithermal neutron reflectometry. For the reflection of epithermal neutrons, mirrors with dimensions around 300 mm, maintaining a tilt error of approximately 0.1 mrad and a surface roughness of about 0.1 nm, are required. To achieve this, I developed neutron mirrors that satisfied the necessary accuracy by combining a multilayer neutron mirror on a glass substrate with an aluminum substrate. By subjecting these mirrors to epithermal neutrons with energies up to 0.7 eV at oblique incidences, the optical reflection of near-epithermal neutrons was observed. The findings reveal that large optical components, exhibiting shape precision approximately an order of magnitude greater than conventional mirrors, are practically viable. This implies that neutron optics, previously limited to the thermal region, can now be expanded to the epithermal region through the development of large components that maintain high precision.

The improvement in component shape accuracy was demonstrated in an experiment searching for the fifth force using dynamical diffraction. In dynamical diffraction, the averaged potential of the crystal inferred from the observed interference patterns can be used to search for the existence of a fifth force. By using ultra-precision machining to manufacture the sample with a slope error of less than 1 µm, I eliminated the most dominant uncertainty in this experiment. The use of machined silicon single-crystal samples in the experiment successfully increased the limit range for the existence of the fifth force by up to two orders of magnitude. Adding measurements with germanium single-crystal samples to these results indicated an improvement in the search sensitivity by at least 1.3 times and the elimination of unknown systematic uncertainties arising from atomic structure factors and other elemental sources. Thus, it was shown that using neutron optics with improved component shape accuracy allows for a highly precise approach to the investigation of the fifth force.

The improvement of component installation accuracy was demonstrated through the development of a multilayer mirror neutron interferometer. Neutron interferometers can precisely measure the interactions acquired by neutrons. This system can improve measurement sensitivity by using neutron mirrors, which is a completely different mechanism than conventional ones. Each mirror needs to be installed within the precision determined by the coherence length. I achieved the required precision in component installation by applying optical substrates and positioning systems used in laser optics to neutron optics. By employing these developments to construct a neutron interferometer, I observed interference patterns dependent on neutron wavelengths. The developed interferometer, while achieving a measurement sensitivity comparable to traditional interferometers, significantly relaxed the requirements for disturbance suppression devices. Furthermore, the values of neutron nuclear scattering lengths obtained by inserting samples in one path matched the literature values, confirming the correct functioning of the developed interferometer. The advancement in component installation accuracy enabled the realization of neutron mirror arrangements that were previously unachievable, thus establishing a new measurement system in neutron optics.

These demonstration experiments have shown that the application of advanced machining technologies can significantly advance the field of neutron optics. Enhanced neutron optics can be utilized in the exploration of fundamental physics. The development of large mirrors with maintained shape accuracy can be applied in constructing large ellipsoidal focusing mirrors for experiments such as neutron-antineutron oscillation search. Improvements in the shape accuracy of neutron optical components, such as single-crystal samples, enable us to approach the existence of the fifth force using dynamical diffraction. The neutron interferometer, realized through improved component installation accuracy, allows for high-precision re-verification of fundamental physical experiments previously conducted using silicon single crystals. Moreover, this advancement enables the construction of flexible experimental systems that were impossible with conventional interferometers. This opens up potential applications in experiments such as atomic gravitational wave searches and tests of Lorentz invariance. From these, neutron optics using advanced machining technologies extended the range of fundamental physics experiments that can be explored.

Acknowledgments

Bibliography

[1] J. Chadwick, The existence of a neutron, Proc. R. Soc. Lond. A Math. Phys. Sci. 136 (830) (1932) 692–708. `doi:10.1098/rspa.1932.0112`.

[2] P. Hořava, C. M. Melby-Thompson, General covariance in quantum gravity at a Lifshitz point, Phys. Rev. D 82 (6) (2010) 064027. `doi:10.1103/PhysRevD.82.064027`.

[3] N. Arkani-Hamed, S. Dimopoulos, G. Dvali, The hierarchy problem and new dimensions at a millimeter, Phys. Lett. B 429 (3-4) (1998) 263–272. `doi:10.1016/s0370-2693(98)00466-3`.

[4] R. Jackiw, S.-Y. Pi, Chern-Simons modification of general relativity, Phys. Rev. D 68 (10) (2003) 104012. `doi:10.1103/PhysRevD.68.104012`.

[5] K. Konno, T. Matsuyama, S. Tanda, Rotating Black Hole in Extended Chern-Simons Modified Gravity, Progr. Theoret. Phys. 122 (2) (2009) 561–568. `doi:10.1143/PTP.122.561`.

[6] R. Penrose, On the Gravitization of Quantum Mechanics 1: Quantum State Reduction, Found. Phys. 44 (5) (2014) 557–575. `doi:10.1007/s10701-013-9770-0`.

[7] S. Perlmutter *et al.*, Measurements of Ω and Λ from 42 High-Redshift Supernovae, ApJ 517 (2) (1999) 565. `doi:10.1086/307221`.

[8] Planck Collaboration *et al.*, *Planck*2013 results. XVI. Cosmological parameters, Astron. Astrophys. 571 (2014) A16. `doi:10.1051/0004-6361/201321591`.

[9] J. Murata, S. Tanaka, A review of short-range gravity experiments in the LHC era (Feb. 2015). `doi:10.1088/0264-9381/32/3/033001`.

[10] D. J. Kapner *et al.*, Tests of the gravitational inverse-square law below the dark-energy length scale, Phys. Rev. Lett. 98 (2) (2007) 021101. `doi:10.1103/PhysRevLett.98.021101`.

[11] ATLAS Collaboration *et al.*, Search for Dark Matter Candidates and Large Extra Dimensions in Events with a Photon and Missing Transverse Momentum in pp Collision Data at s= TeV with the ATLAS Detector, Phys. Rev. Lett. 110 (1) (2013) 011802. `doi:10.1103/PhysRevLett.110.011802`.

[12] Y. Kamiya *et al.*, Constraints on new gravitylike forces in the nanometer range, Phys. Rev. Lett. 114 (16) (2015) 161101. `doi:10.1103/PhysRevLett.114.161101`.

[13] C. C. Haddock *et al.*, Search for deviations from the inverse square law of gravity at nm range using a pulsed neutron beam, Phys. Rev. D 97 (6) (2018) 062002. `doi:10.1103/PhysRevD.97.062002`.

[14] K. Li *et al.*, Neutron limit on the strongly-coupled chameleon field, Phys Rev D 93 (6) (2016) 062001. `doi:10.1103/physrevd.93.062001`.

[15] H. Fischer *et al.*, Search for dark energy with neutron interferometry (Oct. 2023). `arXiv: 2310.18109`.

[16] M. Jaffe *et al.*, Testing sub-gravitational forces on atoms from a miniature in-vacuum source mass, Nat. Phys. 13 (10) (2017) 938–942. `doi:10.1038/nphys4189`.

[17] P. Yin *et al.*, Experiments with levitated force sensor challenge theories of dark energy, Nat. Phys. 18 (10) (2022) 1181–1185. `doi:10.1038/s41567-022-01706-9`.

[18] G. Ichikawa *et al.*, Observation of the spatial distribution of gravitationally bound quantum states of ultracold neutrons and its derivation using the Wigner function, Phys. Rev. Lett. 112 (7) (2014) 071101. `doi:10.1103/PhysRevLett.112.071101`.

[19] R. Colella, A. W. Overhauser, S. A. Werner, Observation of Gravitationally Induced Quantum Interference, Phys. Rev. Lett. 34 (23) (1975) 1472–1474. `doi:10.1103/PhysRevLett.34.1472`.

[20] H. Abele, H. Leeb, Gravitation and quantum interference experiments with neutrons, New J. Phys. 14 (5) (2012) 055010. `doi:10.1088/1367-2630/14/5/055010`.

[21] A. Królak, M. Patil, The First Detection of Gravitational Waves, Universe 3 (3) (2017) 59. `doi:10.3390/universe3030059`.

[22] S. Iwaguchi *et al.*, Displacement-noise-free neutron interferometer for gravitational wave detection using a single Mach-Zehnder configuration, Phys. Lett. A 441 (2022) 128150. `doi:10.1016/j.physleta.2022.128150`.

[23] D. Kikuchi *et al.*, Possible altitudinal, latitudinal, and directional dependence of the relativistic Sagnac effect in Chern-Simons modified gravity, Phys. Rev. D 90 (6) (2014) 064036. `doi:10.1103/PhysRevD.90.064036`.

[24] H. Okawara, K. Yamada, H. Asada, Possible daily and seasonal variations in quantum interference induced by Chern-Simons gravity, Phys. Rev. Lett. 109 (23) (2012) 231101. `doi:10.1103/PhysRevLett.109.231101`.

[25] H. Rauch *et al.*, Precise determination of the 4π-periodicity factor of a spinor wave function, Z. Phys. B: Condens. Matter 29 (3) (1978) 281–284. `doi:10.1007/BF01321193`.

[26] A. Danner *et al.*, Spin-rotation coupling observed in neutron interferometry, npj Quantum Information 6 (1) (2020) 1–6. `doi:10.1038/s41534-020-0254-8`.

[27] T. Denkmayr *et al.*, Weak values from strong interactions in neutron interferometry, Physica B Condens. Matter 551 (August 2017) (2018) 339–346. `doi:10.1016/j.physb.2018.04.014`.

[28] J. H. Christenson *et al.*, Evidence for the pi Decay of the 20 Meson, Phys. Rev. Lett. 13 (4) (1964) 138–140. `doi:10.1103/PhysRevLett.13.138`.

[29] W.-M. Y. e. Al, Review of particle physics, J. Phys. G Nucl. Part. Phys. 33 (1) (2006) 1–1232. `doi:10.1088/0954-3899/33/1/001`.

[30] Belle Collaboration *et al.*, Observation of mixing-induced CP violation in the neutral B meson system, Phys. Rev. D 66 (3) (2002) 032007. `doi:10.1103/PhysRevD.66.032007`.

[31] T. Okudaira *et al.*, Angular distribution of γ rays from neutron-induced compound states of La140, Phys. Rev. C Nucl. Phys. 97 (3) (2018) 034622. `doi:10.1103/physrevc.97.034622`.

[32] V. V. Flambaum, Enhanced nuclear Schiff moment and time-reversal violation in ^{229}Th-containing molecules, Phys. Rev. C Nucl. Phys. 99 (3) (2019) 035501. `doi:10.1103/PhysRevC.99.035501`.

[33] W. M. Snow, C. Haddock, B. Heacock, Searches for Exotic Interactions Using Neutrons, Symmetry 14 (1) (2021) 10. `doi:10.3390/sym14010010`.

[34] M. Pospelov, A. Ritz, Electric dipole moments as probes of new physics, Ann. Phys. 318 (1) (2005) 119–169. `doi:10.1016/j.aop.2005.04.002`.

[35] C. Abel *et al.*, Measurement of the Permanent Electric Dipole Moment of the Neutron, Phys. Rev. Lett. 124 (8) (2020) 081803. `doi:10.1103/PhysRevLett.124.081803`.

[36] S. Itoh *et al.*, Demonstration of simultaneous measurement of the spin rotation of dynamically-diffracted neutrons from multiple crystal planes using pulsed neutrons, Nucl. Instrum. Methods Phys. Res. A 1057 (2023) 168734. `doi:10.1016/j.nima.2023.168734`.

[37] T. M. Ito, (forthe nEdm Collaboration), Plans for a Neutron EDM Experiment at SNS, J. Phys. Conf. Ser. 69 (1) (2007) 012037. `doi:10.1088/1742-6596/69/1/012037`.

[38] K. Babu *et al.*, Neutron-Antineutron Oscillations: A Snowmass 2013 White Paper (Oct. 2013). `arXiv:1310.8593`.

[39] R. N. Mohapatra, Neutron-antineutron oscillation in grand unified theories: An update, Nucl. Instrum. Methods Phys. Res. A 284 (1) (1989) 1–8. `doi:10.1016/0168-9002(89)90237-4`.

[40] M. Baldo-Ceolin *et al.*, A new experimental limit on neutron-antineutron oscillations, Zeitschrift für Physik C Particles and Fields 63 (3) (1994) 409–416. `doi:10.1007/BF01580321`.

[41] C. Theroine, A neutron-antineutron oscillation experiment at the European Spallation Source, Nuclear and Particle Physics Proceedings 273-275 (2016) 156–161. `doi:10.1016/j.nuclphysbps.2015.09.019`.

[42] B. Knorr, Lorentz symmetry is relevant, Phys. Lett. B 792 (2019) 142–148. `doi:10.1016/j.physletb.2019.01.070`.

[43] D. Mattingly, Modern Tests of Lorentz Invariance, Living Rev. Relativ. 8 (1) (2005) 5. `doi:10.12942/lrr-2005-5`.

[44] T. A. Brun, L. Mlodinow, Detecting discrete spacetime via matter interferometry, Phys. Rev. D 99 (1) (2019) 015012. `doi:10.1103/PhysRevD.99.015012`.

[45] H. M. Hofmann, G. M. Hale, Three-Nucleon Force in the 4He Scattering System (Nov. 2002). `arXiv:nucl-th/0211008`.

[46] M. G. Huber *et al.*, Precision measurement of the n-3He incoherent scattering length using neutron interferometry, Phys. Rev. Lett. 102 (20) (2009) 200401. `doi:10.1103/PhysRevLett.102.200401`.

[47] M. G. Huber *et al.*, Neutron interferometric measurement of the scattering length difference between the triplet and singlet states of n-^{3}He (6) (2014) 064004. `arXiv:1409.8567`, `doi:10.1103/PhysRevC.90.064004`.

[48] R. Haun *et al.*, Precision Measurement of the Neutron Scattering Length of ^{4}He Using Neutron Interferometry, Phys. Rev. Lett. 124 (1) (2020) 012501. `doi:10.1103/PhysRevLett.124.012501`.

[49] P. R. Huffman *et al.*, Precision neutron interferometric measurement of the -³He coherent neutron scattering length, Phys. Rev. C Nucl. Phys. 70 (1) (2004) 014004. `doi:10.1103/PhysRevC.70.014004`.

[50] H. Rauch, W. Treimer, U. Bonse, Test of a single crystal neutron interferometer, Phys. Lett. A 47 (5) (1974) 369–371. `doi:10.1016/0375-9601(74)90132-7`.

[51] A. Zeilinger *et al.*, Single- and double-slit diffraction of neutrons, Rev. Mod. Phys. 60 (4) (1988) 1067–1073. `doi:10.1103/RevModPhys.60.1067`.

[52] V. F. Sears, Neutron scattering lengths and cross sections, Neutron News 3 (3) (1992) 26–37. `doi:10.1080/10448639208218770`.

[53] K. Shibata *et al.*, JENDL-4.0: A New Library for Nuclear Science and Engineering, J. Nucl. Sci. Technol. 48 (1) (2011) 1–30. `doi:10.1080/18811248.2011.9711675`.

[54] 海. 徹 *et al.*, 多層膜における中性子の光学的性質, 日本結晶学会誌 20 (3) (1978) 167–178. `doi:10.5940/jcrsj.20.167`.

[55] F. Mezei, Novel polarized neutron devices: supermirror and spin component amplifier, Commun. Phys.; (United Kingdom) 1:3 (Apr. 1976).

[56] S. Broekhuijsen, 11B4C containing Ni/Ti neutron multilayer mirrors, Vol. 1905 of Linköping Studies in Science and Technology. Licentiate Thesis, Linköping University Electronic Press, Linköping, 2021. `doi:10.3384/diss.diva-174637`.

[57] T. Newton, D. Flynn, R. Williams, The national bureau of standards reactor at the NIST center for neutron research, in: Encyclopedia of Nuclear Energy, Elsevier, 2021, pp. 74–81. `doi:10.1016/b978-0-12-819725-7.00030-1`.

[58] https://www.issp.u-tokyo.ac.jp/labs/neutron/jrr3/, `https://www.issp.u-tokyo.ac.jp/labs/neutron/jrr3/`.

[59] Y. Yamagata *et al.*, Development of a neutron generating target for compact neutron sources using low energy proton beams, J. Radioanal. Nucl. Chem. 305 (3) (2015) 787–794. `doi:10.1007/s10967-015-4059-8`.

[60] K. Hirota *et al.*, Design and Construction of an Imaging beamline at the Nagoya University Neutron Source, EPJ Web of Conferences 231 (2020) 05002. `doi:10.1051/epjconf/202023105002`.

[61] P. W. Lisowski, K. F. Schoenberg, The Los Alamos Neutron Science Center, Nucl. Instrum. Methods Phys. Res. A 562 (2) (2006) 910–914. `doi:10.1016/j.nima.2006.02.178`.

[62] J. Wei *et al.*, China Spallation Neutron Source - An overview of application prospects, Chin. Phys. C 33 (11) (2009) 1033–1042. `doi:10.1088/1674-1137/33/11/021`.

[63] K. H. Andersen, C. J. Carlile, A proposal for a next generation European neutron source, J. Phys. Conf. Ser. 746 (1) (2016) 012030. `doi:10.1088/1742-6596/746/1/012030`.

[64] S. Nagamiya, Introduction to J-PARC, Prog Theor Exp Phys 2012 (1) (2012) 02B001. `doi:10.1093/ptep/pts025`.

[65] K. Nakajima *et al.*, Materials and Life Science Experimental Facility (MLF) at the Japan Proton Accelerator Research Complex II: Neutron Scattering Instruments, Quantum Beam Science 1 (3) (2017) 9. `doi:10.3390/qubs1030009`.

[66] N. Niimura *et al.*, An imaging plate neutron detector, Nucl. Instrum. Methods Phys. Res. A 349 (2) (1994) 521–525. `doi:10.1016/0168-9002(94)91220-3`.

[67] J. D. Parker *et al.*, Neutron imaging detector based on the μPIC micro-pixel chamber, Nucl. Instrum. Methods Phys. Res. A 697 (2013) 23–31. `doi:10.1016/j.nima.2012.08.036`.

[68] J. D. Parker *et al.*, Spatial resolution of a μPIC-based neutron imaging detector, Nucl. Instrum. Methods Phys. Res. A 726 (2013) 155–161. `doi:10.1016/j.nima.2013.06.001`.

[69] S. Uno *et al.*, Two-dimensional Neutron Detector with GEM and its Applications, Phys. Procedia 26 (2012) 142–152. `doi:10.1016/j.phpro.2012.03.019`.

[70] S. Uno *et al.*, Development of a Two-Dimensional Gaseous Detector for Energy-Selective Neutron Radiography, Phys. Procedia 37 (2012) 600–605. `doi:10.1016/j.phpro.2012.01.035`.

[71] K. Hirota *et al.*, Development of a neutron detector based on a position-sensitive photomultiplier, Phys. Chem. Chem. Phys. 7 (8) (2005) 1836–1838. `doi:10.1039/b417838f`.

[72] S. Egawa *et al.*, Single-shot achromatic imaging for broadband soft x-ray pulses, Opt. Lett. 45 (2) (2020) 515. `doi:10.1364/ol.381538`.

[73] T. Saiki *et al.*, Sequentially timed all-optical mapping photography boosted by a branched 4f system with a slicing mirror, Opt. Express 28 (21) (2020) 31914–31922. `doi:10.1364/OE.400679`.

[74] N. Ebizuka *et al.*, Development of a multichannel Fourier transform spectrometer, Appl. Opt. 34 (34) (1995) 7899–7906. `doi:10.1364/AO.34.007899`.

[75] D. B. Newell *et al.*, The CODATA 2017 values ofh,e,k, andNAfor the revision of the SI, Metrologia 55 (1) (2018) L13–L16. `doi:10.1088/1681-7575/aa950a`.

[76] T. Hosobata *et al.*, Development of precision elliptic neutron-focusing supermirror, Opt. Express 25 (17) (2017) 20012–20024. `doi:10.1364/OE.25.020012`.

[77] T. Hosobata *et al.*, Elliptic neutron-focusing supermirror for illuminating small samples in neutron reflectometry, Opt. Express 27 (19) (2019) 26807–26820. `doi:10.1364/OE.27.026807`.

[78] S. Takeda *et al.*, A Focusing Test of a Multiple Segmented Ellipsoidal Neutron-Focusing Mirror for a Compact-Focusing SANS Instrument, in: Proceedings of the International Conference on Neutron Optics (NOP2017), Vol. 22 of JPS Conference Proceedings, Journal of the Physical Society of Japan, 2018, pp. 1–8. `doi:10.7566/JPSCP.22.011013`.

[79] 田. 英明 *et al.*, ホログラムスケールを用いたエンコーダの高精度化, 精密工学会誌 89 (4) (2023) 336–342. `doi:10.2493/jjspe.89.336`.

[80] T. Glaschke, L. L. Deck, P. J. de Groot, Characterizing the resolving power of laser Fizeau interferometers, in: Fifth European Seminar on Precision Optics Manufacturing, Vol. 10829, SPIE, 2018, pp. 26–31. `doi:10.1117/12.2317630`.

[81] T. E. Mason *et al.*, The Spallation Neutron Source in Oak Ridge: A powerful tool for materials research, Physica B Condens. Matter 385-386 (2006) (2006) 955–960. `doi:10.1016/j.physb.2006.05.281`.

[82] M. Utsuro, V. K. Ignatovich, Handbook of Neutron Optics, Wiley, 2010. `doi:10.1002/9783527628780`.

[83] H. M. Shimizu *et al.*, Measurement of cold neutron-beam focusing effect of a permanent sextupole magnet, Nucl. Instrum. Methods Phys. Res. A 430 (2) (1999) 423–434. `doi: 10.1016/S0168-9002(99)00238-7`.

[84] E. Fermi, Motion of neutrons in hydrogenous substances, Ric. Sci. 7 (2) (1936) 13–52.

[85] H. Abele *et al.*, Characterization of a ballistic supermirror neutron guide, Nucl. Instrum. Methods Phys. Res. A 562 (1) (2006) 407–417. `doi:10.1016/j.nima.2006.03.020`.

[86] K. Mishima *et al.*, Design of neutron beamline for fundamental physics at J-PARC BL05, Nucl. Instrum. Methods Phys. Res. A 600 (1) (2009) 342–345. `doi:10.1016/j.nima.2008.11.087`.

[87] K. Mishima, J-PARC neutron beam line (BL05/NOP) for fundamental physics, Hamon 25 (2) (2015) 156–160. `doi:10.5611/hamon.25.2\_156`.

[88] T. Ebisawa *et al.*, Neutron Reflectivities of Ni-Mn and Ni-Ti Multilayers for Monochromators and Supermirrors, J. Nucl. Sci. Technol. 16 (9) (1979) 647–659. `doi:10.3327/jnst.16.647`.

[89] T. Ebisawa *et al.*, The neutron reflectometer (C3-1-2) at the JRR-3M reactor at JAERI, Physica B Condens. Matter 213-214 (C) (1995) 901–903. `doi:10.1016/0921-4526(95)00318-4`.

[90] Y. Kawabata *et al.*, Improvement of the cold neutron beam line (CN-3) in KUR for neutron optical device development, Physica B Condens. Matter 311 (1) (2002) 106–111. `doi:10.1016/ S0921-4526(01)01119-X`.

[91] M. Hino *et al.*, A study on reflectivity limit of neutron supermirror, Nucl. Instrum. Methods Phys. Res. A 600 (1) (2009) 207–209. `doi:10.1016/j.nima.2008.11.125`.

[92] F. Eriksson *et al.*, Ion-assisted magnetron sputter deposition of B4C-doped Ni/Ti multilayer mirrors, in: C. Morawe, A. M. Khounsary, S. Goto (Eds.), Advances in X-Ray/EUV Optics and Components XIII, Vol. 10760, SPIE, 2018, pp. 40–43. `doi:10.1117/12.2317742`.

[93] C. Höglund *et al.*, B 4C thin films for neutron detection, J. Appl. Phys. 111 (10) (2012). `doi: 10.1063/1.4718573`.

[94] T. Veres *et al.*, Roughness replication in neutron supermirrors, J. Appl. Crystallogr. 50 (1) (2017) 184–191. `doi:10.1107/S1600576716019385`.

[95] F. Maekawa *et al.*, NOBORU: J-PARC BL10 for facility diagnostics and its possible extension to innovative instruments, Nucl. Instrum. Methods Phys. Res. A 600 (1) (2009) 335–337. `doi: 10.1016/j.nima.2008.11.086`.

[96] Y. Kiyanagi *et al.*, Design study of the imaging beam line at J-PARC MLF, ERNIS, Nucl. Instrum. Methods Phys. Res. A 651 (1) (2011) 16–20. `doi:10.1016/j.nima.2011.02.075`.

[97] E. G. Kessler *et al.*, The Lattice Spacing Variability of Intrinsic Float-Zone Silicon, J. Res. Natl. Inst. Stand. Technol. 122 (24) (2017) 1–25. `doi:10.6028/jres.122.024`.

[98] C. G. Shull, Observation of Pendell\"osung Fringe Structure in Neutron Diffraction, Phys. Rev. Lett. 21 (23) (1968) 1585–1589. `doi:10.1103/PhysRevLett.21.1585`.

[99] H. Rauch, Neutron Physics, 1978.

[100] N. Kato, IUCr, A theoretical study of pendellösung fringes. I. General considerations, Acta Crystallogr. 14 (5) (1961) 526–532. `doi:10.1107/S0365110X61001625`.

[101] N. Kato, A theoretical study of pendellösung fringes. II. Detailed discussion based upon a spherical wave theory, Acta Crystallogr. 14 (6) (1961) 627–636. `doi:10.1107/S0365110X61001947`.

[102] N. Kato, Pendellösung Fringes in Distorted Crystals II. Application to Two-Beam Cases, J. Phys. Soc. Jpn. 19 (1) (1964) 67–77. `doi:10.1143/JPSJ.19.67`.

[103] N. Kato, Pendellösung Fringes in Distorted Crystals III. Application to homogeneously bent crystals, J. Phys. Soc. Jpn. 19 (6) (1964) 971–985. `doi:10.1143/JPSJ.19.971`.

[104] S. W. Lovesey, Theory of neutron scattering from condensed matter. Vol. 1. Nuclear scattering, United Kingdom, 1984.

[105] A. Erba *et al.*, Accurate dynamical structure factors from ab initio lattice dynamics: the case of crystalline silicon, J. Comput. Chem. 34 (5) (2013) 346–354. `doi:10.1002/jcc.23138`.

[106] M. Deutsch, M. Hart, S. Cummings, High-accuracy structure-factor measurements in germanium, Phys. Rev. B Condens. Matter 42 (2) (1990) 1248–1253. `doi:10.1103/physrevb.42.1248`.

[107] J. S. Reid, J. D. Pirie, Dynamic deformation and the Debye–Waller factors for silicon-like crystals, Acta Crystallogr. A 36 (6) (1980) 957–965. `doi:10.1107/S0567739480001982`.

[108] N. Isgur, Interpreting the Neutron's Electric Form Factor: Rest Frame Charge Distribution or Foldy Term?, Phys. Rev. Lett. 83 (2) (1999) 272–275. `doi:10.1103/PhysRevLett.83.272`.

[109] Particle Data Group *et al.*, Review of Particle Physics, Phys. Rev. D Part. Fields 98 (3) (2018) 030001. `doi:10.1103/PhysRevD.98.030001`.

[110] V. F. Sears, Electromagnetic neutron-atom interactions, Phys. Rep. 141 (5) (1986) 281–317. `doi:10.1016/0370-1573(86)90129-8`.

[111] M. A. Spackman, The electron distribution in silicon. A comparison between experiment and theory, Acta Crystallogr. A 42 (4) (1986) 271–281. `doi:10.1107/S0108767386099312`.

[112] S. Cummings, M. Hart, Redetermination of Absolute Structure Factors for Silicon at Room and Liquid Nitrogen Temperatures, Aust. J. Phys. 41 (3) (1988) 423–432. `doi:10.1071/ph880423`.

[113] J. H. Hubbell *et al.*, Erratum: Atomic Form Factors, Incoherent Scattering Functions, and Photon Scattering Cross Sections, J. Phys. Chem. Ref. Data 6 (2) (1977) 615–616. `doi:10.1063/1.555554`.

[114] G. L. Greene, V. Gudkov, Neutron interferometric method to provide improved constraints on non-Newtonian gravity at the nanometer scale, Phys. Rev. C Nucl. Phys. 75 (1) (2007) 015501. `doi:10.1103/PhysRevC.75.015501`.

[115] T. Fujiie, 中性子の動力学的回折を用いた未知相互作用の探索, Master's thesis, Nagoya University (Mar. 2020).

[116] B. Heacock *et al.*, Pendellösung interferometry probes the neutron charge radius, lattice dynamics, and fifth forces, Science 373 (6560) (2021) 1239–1243. `doi:10.1126/science.abc2794`.

[117] B. Heacock, Doctoral Thesis of benjamin Heacock, Ph.D. thesis, North Carolina State University (2019).

[118] Y. A. Abramov, F. P. Okamura, A Topological Analysis of Charge Densities in Diamond, Silicon and Germanium Crystals, Acta Crystallogr. A 53 (2) (1997) 187–198. `doi:10.1107/S0108767396013335`.

[119] L. Koester, K. Knopf, W. Waschkowski, Neutron interactions with germanium isotopes and amorphous and crystalline GeO2, Z. Phys. A At. Nucl. 327 (2) (1987) 129–136. `doi:10.1007/BF01292400`.

[120] M. S. Dewey *et al.*, Structure factors in germanium at 0.342 and 1.382 MeV, Phys. Rev. B Condens. Matter 50 (5) (1994) 2800–2808. `doi:10.1103/physrevb.50.2800`.

[121] T. Takama, S. Sato, Determination of the atomic scattering factors of germanium by means of the Pendellösung-beat measurement using white radiations, Jpn. J. Appl. Phys. 20 (7) (1981) 1183–1189. `doi:10.1143/JJAP.20.1183`.

[122] H. Rauch, S. A. Werner, Neutron Interferometry: Lessons in Experimental Quantum Mechanics, Wave-Particle Duality, and Entanglement, Oxford University Press, 2015. `doi:10.1093/acprof:oso/9780198712510.001.0001`.

[123] S. Sponar *et al.*, Tests of fundamental quantum mechanics and dark interactions with low-energy neutrons, Nature Reviews Physics 3 (5) (2021) 309–327. `doi:10.1038/s42254-021-00298-2`.

[124] S. Hammerschmied *et al.*, Measurements of the coherent neutron-tritium scattering length and its relation to the four nucleon problem, Z Physik A 302 (4) (1981) 323–328. `doi:10.1007/bf01414263`.

[125] H. Rauch, D. Tuppinger, New methods for interferometric neutron scattering lengths measurements, Zeitschrift für Physik A Atoms and Nuclei 322 (3) (1985) 427–432. `doi:10.1007/BF01412077`.

[126] A. Ioffe *et al.*, Precision neutron-interferometric measurement of the coherent neutron-scattering length in silicon, Phys. Rev. A 58 (2) (1998) 1475–1479. `doi:10.1103/PhysRevA.58.1475`.

[127] S. A. Werner, J.-L. Staudenmann, R. Colella, Effect of Earth's Rotation on the Quantum Mechanical Phase of the Neutron, Phys. Rev. Lett. 42 (17) (1979) 1103–1106. `doi:10.1103/PhysRevLett.42.1103`.

[128] A. Cimmino *et al.*, Observation of the topological Aharonov-Casher phase shift by neutron interferometry, Phys. Rev. Lett. 63 (4) (1989) 380–383. `doi:10.1103/PhysRevLett.63.380`.

[129] Y. Hasegawa *et al.*, Violation of a Bell-like inequality in single-neutron interferometry, Nature 425 (6953) (2003) 45–48. `doi:10.1038/nature01881`.

[130] D. A. Pushin *et al.*, Experimental realization of decoherence-free subspace in neutron interferometry, Phys. Rev. Lett. 107 (15) (2011) 150401. `doi:10.1103/PhysRevLett.107.150401`.

[131] C. W. Clark *et al.*, Controlling neutron orbital angular momentum, Nature 525 (7570) (2015) 504–506. `doi:10.1038/nature15265`.

[132] H. Lemmel *et al.*, Neutron Interferometry constrains dark energy chameleon fields (2015) 310–314`arXiv:1502.06023, doi:10.1016/j.physletb.2015.02.063`.

[133] C. J. Riedel, Direct detection of classically undetectable dark matter through quantum decoherence, Phys. Rev. D 88 (11) (2013) 116005. `doi:10.1103/PhysRevD.88.116005`.

[134] C. J. Riedel, I. Yavin, Decoherence as a way to measure extremely soft collisions with dark matter, Phys. Rev. D 96 (2) (2017) 023007. `doi:10.1103/PhysRevD.96.023007`.

[135] J. M. Rocha, F. Dahia, Neutron interferometry and tests of short-range modifications of gravity (12) (2021) 124014. `arXiv:2103.04218`, `doi:10.1103/PhysRevD.103.124014`.

[136] D. A. Pushin, M. Arif, D. G. Cory, Decoherence-free neutron interferometry, Phys. Rev. A 79 (5) (2009) 053635. `doi:10.1103/PhysRevA.79.053635`.

[137] D. Sarenac *et al.*, Three Phase-Grating Moiré Neutron Interferometer for Large Interferometer Area Applications, Phys. Rev. Lett. 120 (11) (2018) 113201. `doi:10.1103/PhysRevLett.120.113201`.

[138] H. Lemmel *et al.*, Neutron interference from a split-crystal interferometer, J. Appl. Crystallogr. 55 (Pt 4) (2022) 870–875. `doi:10.1107/S1600576722006082`.

[139] H. Funahashi *et al.*, Interferometer for cold neutrons using multilayer mirrors, Phys. Rev. A 54 (1) (1996) 649–651. `doi:10.1103/physreva.54.649`.

[140] M. Kitaguchi, Cold-neutron interferometry using beam splitting etalons, Ph.D. thesis, Kyoto University (2004). `doi:10.14989/doctor.k11047`.

[141] Y. Seki *et al.*, Multilayer Neutron Interferometer with Complete Path Separation, J. Phys. Soc. Jpn. 79 (12) (2010) 124201. `doi:10.1143/JPSJ.79.124201`.

[142] N. Yamamoto *et al.*, Development of Pulsed Neutron Interferometer, in: Proceedings of the 3rd J-PARC Symposium (J-PARC2019), Vol. 011119, Journal of the Physical Society of Japan, 2021, pp. 2–5. `doi:10.7566/jpscp.33.011119`.

[143] M. Kitaguchi *et al.*, Cold-neutron interferometer of the Jamin type, Phys. Rev. A 67 (3) (2003) 033609. `doi:10.1103/PhysRevA.67.033609`.

[144] Y. Seki, Multilayer Neutron Interferometer with Complete Path Separation, Ph.D. thesis, Kyoto University (2011).

[145] P. Saggu *et al.*, Decoupling of a neutron interferometer from temperature gradients, Rev. Sci. Instrum. 87 (12) (2016) 123507. `doi:10.1063/1.4971851`.

[146] D. A. Pushin *et al.*, Neutron Interferometry at the National Institute of Standards and Technology, Adv. High Energy Phys. 2015 (2015) 1–8. `doi:10.1155/2015/687480`.

[147] S. Sakurai, Industrial Users Society for Neutron Application Season Report vol.37, Tech. rep., Taiyo Koko (2017).

[148] https://j-parc.jp/researcher/MatLife/ja/instrumentation/index.html, `https://j-parc.jp/researcher/MatLife/ja/instrumentation/index.html`, accessed: 2023-11-26.

[149] T. Prohaska *et al.*, Standard atomic weights of the elements 2021 (IUPAC Technical Report), J. Macromol. Sci. Part A Pure Appl. Chem. 94 (5) (2022) 573–600. `doi:10.1515/pac-2019-0603`.

[150] W. Bauspiess, U. Bonse, H. Rauch, The prototype neutron interferometer at the Grenoble high flux reactor, Nuclear Instruments and Methods 157 (3) (1978) 495–506. `doi:10.1016/0029-554X(78)90009-5`.

[151] H. Yoshinaga, Recovery of molybdenum and vanadium from spent catalyst, J. MMIJ 123 (12) (2007) 768–771. `doi:10.2473/journalofmmij.123.768`.

[152] A. Addazi *et al.*, New high-sensitivity searches for neutrons converting into antineutrons and/or sterile neutrons at the HIBEAM/NNBAR experiment at the European Spallation Source, J. Phys. G Nucl. Part. Phys. 48 (7) (2021) 070501. `doi:10.1088/1361-6471/abf429`.

[153] R. Wagner *et al.*, Design of an optimized nested-mirror neutron reflector for a NNBAR experiment, Nucl. Instrum. Methods Phys. Res. A 1051 (2023) 168235. `doi:10.1016/j.nima.2023.168235`.

[154] Expression of Interest for A New Search for Neutron-Anti-Neutron Oscillations at ESS.